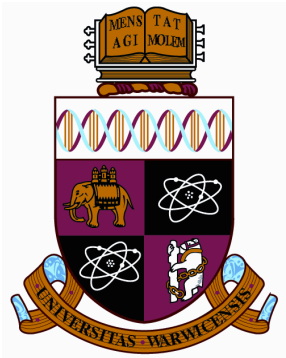

Electroanalytical Applications of Carbon Electrodes using Novel Hydrodynamic Flow Devices

by

Michael Edward Snowden

Thesis

Submitted to the University of Warwick for the degree of

Doctor of Philosophy

Department of Chemistry

June 2010

THE UNIVERSITY OF WARWICK

Table of Contents

Table of Figures

Acknowledgements

I would like to thank everyone who has helped and supported me throughout the course of my PhD, your time and efforts are all greatly appreciated.

Firstly, I thank my supervisors Patrick Unwin and Julie Macpherson for their guidance over the past three years. Their encouragement and enthusiasm across a diverse range of electrochemical areas has presented me with challenges spanning the spectrum of fundamental studies to the design and development of novel analytical devices. Additionally I am grateful for the members of the Electrochemistry Group and my collaborators in Engineering for the training and help received on a variety of equipment that has made this work possible. In particular I am grateful to Lee and Marcus in Mechanical Workshops for their advice and skills in the construction of various parts of vital apparatus, and to Kirk for helping me with parts for electronic set-ups and with repairs.

I would not have made it this far without my friends inside and outside of the University. Massive thanks go to the "Triple-One Crew", and for everyone who took the time to persuade me to eat or have the occasional pint and game of cards! Thanks goes to the University Fencing club and Coventry Ju-Jitsu for preventing the unhealthy build up of stress, and the "riff-raff" from the Mill/Q7 for many good nights out. I am grateful to Sandra for the many little things she has done that have helped ease the burden. I also thank the furry friends that have been more than eager to help me get some much needed fresh air.

Most importantly I am truly grateful for the continual love and support given to me by my parents, my brothers Christopher and David, the rest of my family, and my girlfriend Heather.

Declaration

The work contained within this thesis is my own except where outlined below. I confirm that this thesis has not been submitted for any degree at another university.

Chapter 3

Theoretical data was obtained from the finite element models written by Dr. Martin Edwards.

Chapter 4 and 5

The construction of the channel flow cells by microstereo lithography was performed by Dr. Philip King. Channel heights were determined by white light interferometery performed by Miss Carrie-Anne McGeouch, and the poly crystalline boron doped diamond sample was laser cut by Miss Laura Hutton. Photography within these chapters was performed by Mr. Massimo Peruffo. The work presented within chapter 4 has been published:

M.E. Snowden, P.H. King, J.A.Covington, Julie V.Macpherson and Patrick R.Unwin, *Analytical Chemistry* **2010**, *82*, 3124

Chapter 6

The radial flow cell was fabricated by Mr Maxim Joseph and the nozzle height was determined by Miss Carrie-Anne McGeouch. All photographs for this chapter were taken by Mr. Massimo Peruffo.

Abstract

Since the first reported use of carbon nanotubes (CNTs) as an electrode material in 1996 the use of CNTs within electrochemistry has grown rapidly. Single walled carbon nanotubes offer bio-compatibility combined with nano-scale dimensions and low background currents in the pristine state. Over the past decade the quantity of SWNTs synthesised globally has greatly increased making the material available for a variety of studies and potentially a feasible material for commercial electrodes.

Despite this rise in popularity there is still an on going debate about the sites of electron transfer (ET) at a carbon nanotube. Some reports claim that the sidewall of the carbon nanotube exhibits sluggish ET rates with the majority of the ET occurring at defect sites and the end of the CNT. In contrast there is also evidence that suggests that ET at the sidewall is facile and not sluggish. The origin of ET is investigated using both theoretical and experimental data to probe the developing diffusion profiles to active ET sites. This is achieved on the timescale of a typical voltammetric experiment by significantly reducing the rate of diffusion to the electroactive sites using a Nafion™ film. The reduced rate of diffusion allows the developing diffusion profiles to the individual sites to be decoupled.

The use of convection and diffusion is a proven electrochemical technique to increase the sensitivity of analytical measurements and to probe reaction rates and mechanisms. The well-defined mass transport within a channel flow cell or an impinging jet electrode, combined with the continual replacement of solution, makes this geometry amenable to online studies, *e.g.* bedside or industrial monitoring, or a combination with chromatography. One draw back of conventional channel flow and impinging jet electrode set-ups is the need for specialist equipment or calibration steps each time the system is assembled. The use of microstereo lithography (MSL) to construct custom designed cells for use with a variety of planar electrodes is investigated. The hydrodynamics within the proposed designs are theoretically tested and verified experimentally. The devices constructed are easily assembled using a wide range of electrode materials and the computer aided manufacture provides flexibility in critical dimensions. Importantly, the devices only require a one-off determination of the height prior to assembly, removing the need for an electrochemical calibration step as the cells do not distort during assembly.

Of particular interest for analytical studies is the greatly reduced background currents provided by a carbon nanotube network compared to an equivalent size carbon macroelectrode. The lower background signal allows small Faradaic currents to be observed experimentally, allowing lower concentrations to be distinguished. The enhanced sensitivity is combined with the increased mass transport of channel flow and impinging jet convective systems to determine the limit of detection for particular channel and impinging jet geometries under constant flow rates. This approach allows the successful detection of nano-molar concentrations under hydrodynamic control using standard voltammetric techniques.

Abbreviations

AFM	Atomic force microscopy
CA	Chronoamperometry
CVD	Catalysed chemical vapour deposition
CNT	Carbon nanotube
CV	Cyclic Voltammetry
ET	Electron transfer
$FcTMA^+$	Ferrocenylmethyltrimethylammonium hexafluorophosphate
FEM	Finite element modelling
FE-SEM	Field emission scanning electron microscopy
GC	Glassy carbon
HD	High density
HiPCO	High pressure carbon monoxide conversion
HOPG	Highly orientated pyrolytic graphite
IHP	Inner Helmholtz plane
IJE	Impinging jet electrode
LSV	Linear Sweep Voltammetry
MEMS	Microelectromechanical systems
MFC	Mass flow controlled
MSL	Microstereo lithography
MWNT	Multi walled carbon nanotube
OHP	Outer Helmholtz plane
pBDD	Polycrystalline boron doped diamond
PBS	Phosphate buffered saline solution

RDE	Rotating disc electrode
RE	Reference electrode
RFC	Radial flow cell
RP	Rapid prototyping
RRDE	Rotating ring disc electrode
SCE	Saturated calomel electrode
SWNT	Single walled carbon nanotube
TM	TappingMode^{TM}
UME	Ultra micro electrode
VHD	Very high density
WE	Working electrode
WJE	Wall jet electrode
WTE	Wall tube electrode

Symbols

∇	Vector differential operator
ϕ	Electrostatic potential
ϕ_0	Original potential step
κ	Boltzmann constant
$\bar{U}$	Mean fluid velocity
α	Constant coefficient (wall jet electrode)
A	Area
C	Capacitance
c	Concentration of electroactive analyte
c_b	Bulk concentration
C_h	Chiral vector
D	Diffusion coefficient
d	distance
D_{app}	Apparent diffusion coefficient
D_h	Hydraulic diameter
E	Potential
$E_{a/b}$	a/b part potential
E_{appl}	Potential applied to an electrochemical cell
E_{WE}	Potential difference between the working and reference electrodes
F	Faraday's constant
h	Channel half height

i	Current
i_{lim}	limiting current
J	Flux
j	current density
k_t	Coefficient of mass transport
m	Integer for chiral vector
n	Number of electrons
n	Integer for chiral vector
N	Number of moles
n	Vector normal to a particular boundary
O	Oxidised form of a redox mediator
p	Pressure
p_0	Pressure of the system
Q	Charge
R	Reduced form of a redox mediator
R	Gas constant (8.314 J K^{-1})
r	Radial axis
r_1	Active disc radius
r_2	Insulating cylinder radius
Re	Reynolds number
r_e	Electrode radius
r_n	Nozzle radius
r_t	Radius of cylinder
R_Ω	Resistance
t	Time

T_m	Temperature
T	Vector transpose operator
tanh	Hyperbolic tangent
u	Velocity vector in x direction
u_r	Velocity vector in r direction
$\mathbf{V}$	Velocity vector
v	Velocity vector in y direction
v_e	Potential scan rate of an LSV or CV
V_f	Volume flow rate
W	Rotation frequency
w	Velocity vector in z direction
w_{ch}	Channel width
w_e	Electrode width
x_e	Electrode length
z	Charge on the analyte
η	Dynamic viscosity
ρ	Density of water

1. Introduction

1.1. Overview

This thesis investigates two key areas of electrochemistry; (i) surface activity of electrode materials, focusing on the sites of electron transfer (ET) at the surface of single walled carbon nanotubes (SWNTs), and (ii) the design and development of methods for hydrodynamic control of mass transport to electrode surfaces with particular emphasis on low concentration detection of redox active analyte solutions. This chapter introduces electrochemical concepts pertinent to the results outlined in the thesis and outlines experimental techniques that are used throughout this thesis including the effect of electrode geometries on the electrochemical response, and finite element modelling (FEM).

1.2. Dynamic Electrochemistry

Dynamic electrochemistry is used predominantly to probe the charge transfer of a redox species under non-equilibrium conditions.[1] A potential is applied to a working electrode (WE) with respect to a stable reference electrode (RE), in order to drive ET at the WE surface. Both metallic and a variety of carbon based electrode materials are used within this thesis. The current response observed at an electrode surface is attributed to both Faradaic and non-Faradaic processes.[2, 3] A typical reaction schematic is shown in figure 1.1, where the reduction of the oxidised form of the redox mediator, O, to the reduced product, R, occurs over several steps. The rate

limiting step is the slowest process and can be caused by any one of the processes shown in figure 1.1; for example ET at the WE surface, a chemical step prior to or after ET, a surface reaction (adsorption or desorption), or mass transport to or from the WE surface.[4] The work within this thesis focuses upon reactions which are limited by mass transport under both static and convective regimes.

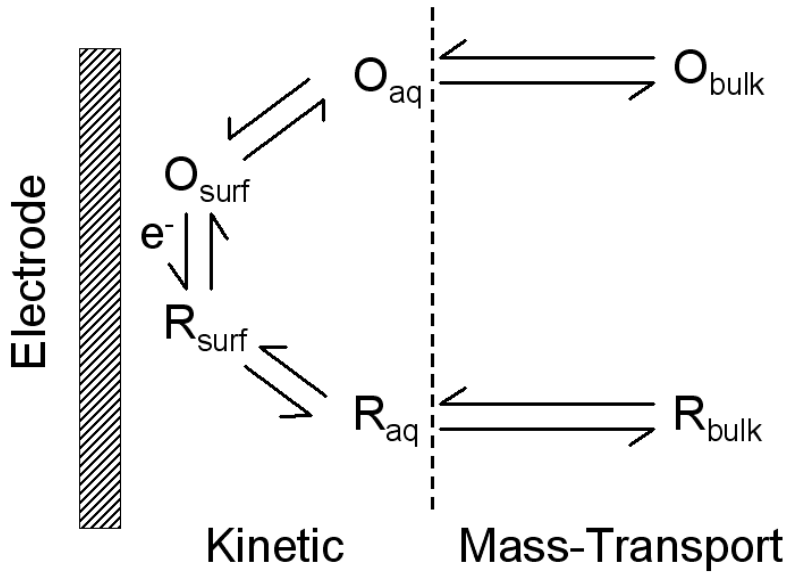

Figure 1.1 Schematic of a basic electrochemical reaction, showing the mass transport and kinetic ET steps in the reduction of species O to R at the electrode surface.

Two types of potential scan are used for electroanalysis within this report, linear sweep voltammetry (LSV) and cyclic voltammetry (CV). An LSV is performed by sweeping the electrode potential in either the positive or negative direction, over a potential range sufficient to cause oxidation or reduction of the analyte of interest. The speed of the sweep can affect the resulting current response as it affects the concentration gradient. A CV is similar to a LSV except that the polarity of the potential ramp is swept in one direction and then reversed, allowing the reversibility of a reaction to be probed. LSV and CV measurements are reported by plotting a current with respect to voltage applied against a stable reference electrode.

Chronoamperometric (CA) measurements involve a potential step, typically from a position where no Faradaic reaction occurs to a point of interest, *e.g.* a potential where the reaction at the electrode surface is not kinetically hindered. CA allows the investigation of current time profiles, for instance to probe a developing diffusion profile.[5]

1.2.1. Faradaic Processes

The transfer of electrons during a reaction is proportional to the number of moles of reactant involved, in accordance with Faraday's laws of electrolysis.[2, 3] For example the reduction of species O to R by electrolysis involves the transfer of a number of electrons (n), equation 1.1.

$$O + ne^- \rightarrow R \quad \textbf{(1.1)}$$

The Faradaic current, i, observed is proportional to the flux (J), rate of the reaction per unit area, which can be expressed by equation 1.2,

$$J = \frac{dN}{dt} \quad \textbf{(1.2)}$$

where N is the number of moles electrolysed and t is time. The number of moles electrolysed (N) is proportional to charge, Q (equation 1.3), hence the flux can be expressed as the transfer of charge as shown in equation 1.4.

$$Q = nFN \tag{1.3}$$

$$J = \frac{dQ}{dt} \times \frac{1}{nF} \tag{1.4}$$

where F is Faraday's constant (96485 C mol^{-1}). Current is the transfer of charge per unit time, which gives rise to equation 1.5,

$$J = \frac{i}{nF} \tag{1.5}$$

As flux is the rate of reaction per unit area, the current produced for a specific area (A) can be calculated from equation 1.6

$$i = nAFJ \tag{1.6}$$

1.2.2. Non-Faradaic Processes

The current observed during an experiment can also have a contribution from non-Faradaic processes. These do not involve electron transfer, but relate to a charge difference at the WE/solution interface.[2] The Faradaic processes are of primary interest throughout this thesis; however for accurate analysis of the data obtained an awareness of these non-Faradaic processes is essential.

The WE/solution interface can be considered analogous to a capacitor, when a change in potential is applied to the WE surface, ions within the solution move to balance the change in electron density at the WE surface, perturbing the "electrical

double layer". The model presented by Bockris, Devanathan and Muller,[6] proposes that the solution side of the "electrical double layer" consists of solvent and solute molecules, which form several layers as shown in figure 1.2. This model is based upon previous models proposed by Helmholtz (1853), Gouy (1910), Chapman (1913), Stern (1924) and Grahame (1947) and takes into consideration that the solvent molecules are in a greater excess than the solvated ions.[3] The layer closest to the electrode surface consists of solvent molecules and desolvated adsorbed ions. The inner Helmholtz plane (IHP) is located through the centre of the desolvated adsorbed molecules. The outer layer is formed from solvated ions and is called the outer Helmholtz plane (OHP).[1-3]

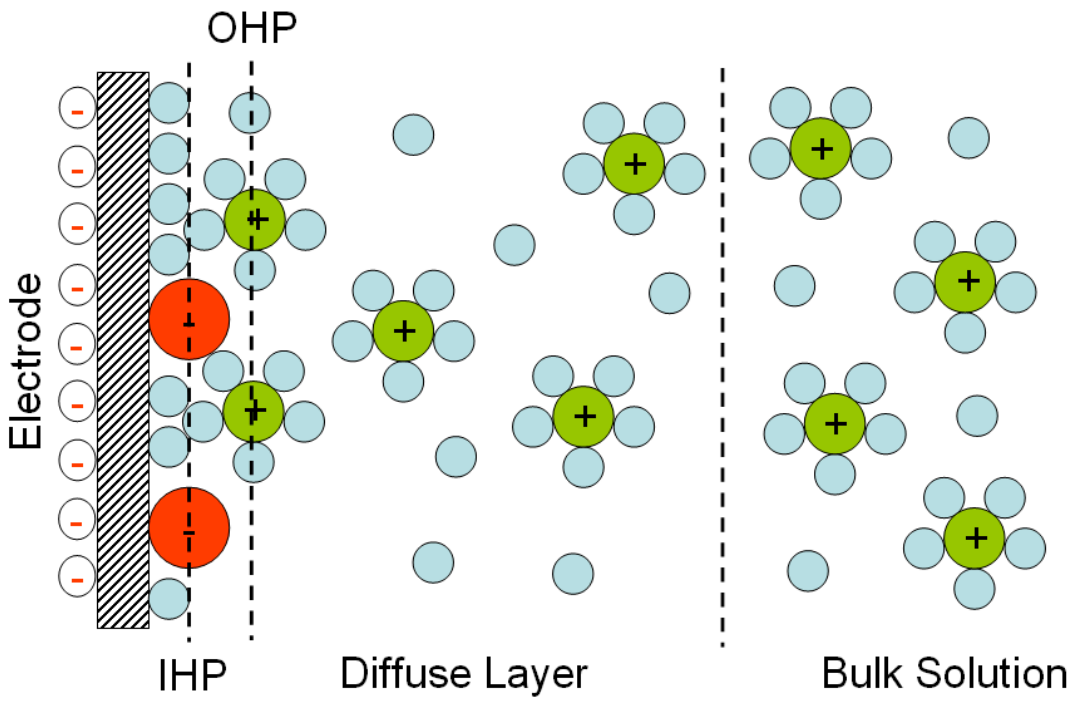

Figure 1.2 Model for the "electrical double layer" as proposed by Bockris *et al.*[6] at an electrode surface assuming a negatively charged electrode. Red molecules are specifically adsorbed anions, green molecules are cations, and blue molecules represent solvent molecules.

Resistance within an electrochemical cell can be attributed to the resistance of the solution and the resistance of the electrode materials employed. Resistive and capacitive effects within electrochemical systems can be treated simply by assuming the electrochemical cell is analogous to a capacitor, of capacitance C, and resistor, of resistance R_Ω, in series as shown in figure 1.3 (a). $R_\Omega C$ effects in an electrochemical system will contribute to the currents flowing during a CA or a CV experiment, and in the case of high R_Ω result in a measurable ohmic drop (section 1.2.4). The $R_\Omega C$ response can be quantified by performing a CA experiment, equation 1.7, or running a LSV, equation 1.8.[2]

$$i = \frac{\Delta E}{R_\Omega} e^{(-t/R_\Omega C)} \quad \textbf{(1.7)}$$

$$i = v_e C[1 - e^{(-t/R_\Omega C)}] \quad \textbf{(1.8)}$$

where E is the potential, and v_e is the scan rate of the LSV or CV. The general shape of the current-time decay in a CA and the effects of $R_\Omega C$ on the background currents in a CV are shown in figure 1.3 (b) and (c) respectively. Note that for a CV, when a constant current response is reached, the hysteresis is dependant only on v and C.

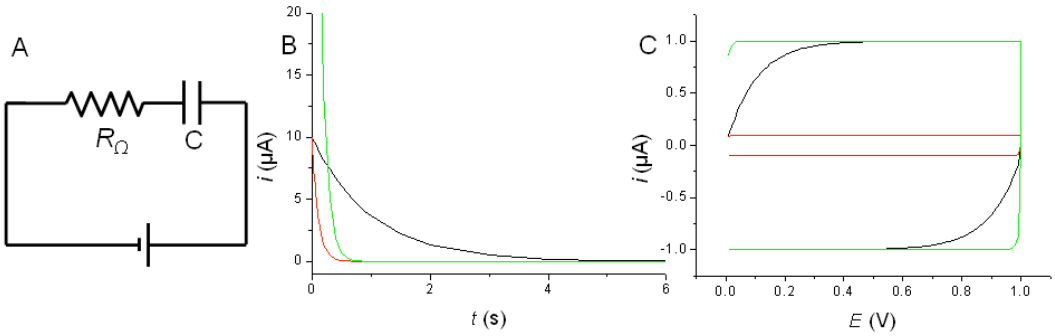

Figure 1.3 (a) The analogy of a resistor and capacitor to an electrochemical cell. (b) The current-time decay for a CA experiment for a 1 V potential step and (c) the hysteresis in a CV for the same system at v_e = 100 mV s^{-1} for systems of C = 10 μF, (-) R_Ω = 0.1 MΩ, (-) R_Ω = 0.01 MΩ, and (-) R_Ω = 0.1 MΩ and C = 1 μF.

1.2.3. Other Background Processes

During an electrochemical measurement the applied potential can result in other reactions occurring that contribute to the overall current response. For example, the oxidation or reduction of the solvent causes the measured current to rapidly increase. The potential range between the oxidation and reduction potentials for a solvent is referred to as the solvent window. The majority of quantitative electrochemical measurements are taken within the solvent window. It is important to note that for different solvents and WE materials the solvent window varies.[7, 8]

In some situations the WE surface may undergo a surface reaction or a reaction with another species in solution, for example a Pt electrode in 0.5 M H_2SO_4 undergoes the electro-adsorption and electro-desorption of hydrogen and oxygen as shown in figure 1.4 (a).[9, 10] Additionally Pt is also prone to reaction with dissolved oxygen as

demonstrated in figure 1.4 (b) where the red line represents an aerated KNO_3 solution, and the black line represents the same solution after being purged with nitrogen.[11] The affect of other background processes on the analysed data are minimised by using species that undergo reduction or oxidation away from the extremes of the solvent window and by thoroughly purging all solutions used on metal electrodes with nitrogen prior to the experiment.

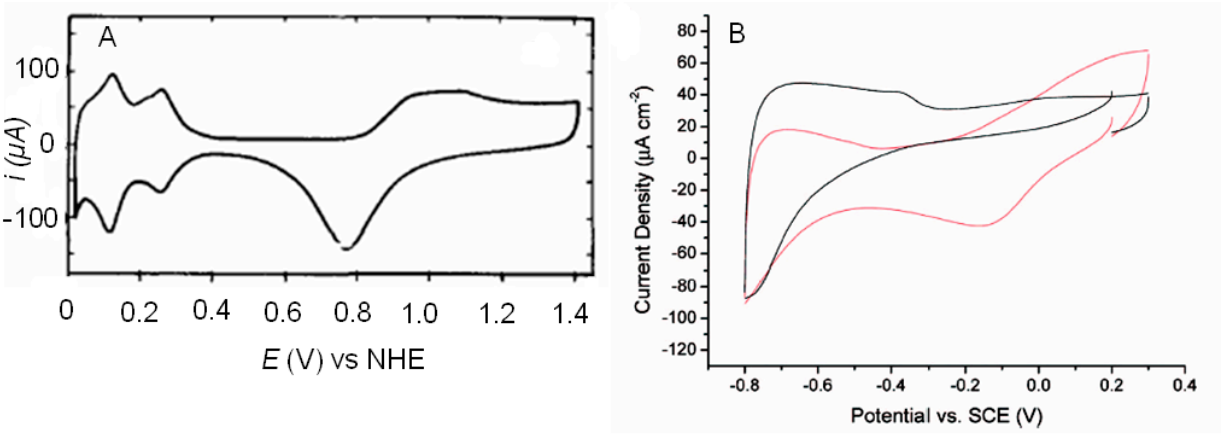

Figure 1.4 (a) CV showing the background surface reactions occuring on a Pt electrode in 0.5 M H_2SO_4, the potential taken relative to the normal hydrogen electrode (NHE).[9] (b) Comparison of (-) aerated and (-) nitrogen purged 0.1 mol dm^{-3} KNO_3 solution on a 3 mm Pt disc electrode.[11]

1.2.4. Ohmic Drop and Counter Electrodes

In addition to the $R_\Omega C$ effects as mentioned above, the resistance within the electrochemical system has an effect upon the applied voltage to the working electrode. For a two electrode system the potential applied to the electrochemical cell is assumed to be the same as the potential difference between the WE and the RE. However, the measured current also passes through the RE causing the potential

difference between the WE and the RE to vary from the potential applied to the electrochemical cell, as shown in equation 1.9,

$$E_{appl} = E_{WE} - iR_{\Omega} \quad \textbf{(1.9)}$$

where E_{appl} and E_{WE} are the applied potential and the potential at the WE, respectively. The difference between the actual potential and the applied potential is known as *Ohmic drop*.[2] This situation is exacerbated for high currents passed and low conductivity solutions. When the iR_{Ω} term becomes significant (greater than 1 mV) the current is passed through a third electrode, called the counter electrode (CE). Typically the counter electrode has a large surface area and is made from a material that does not react with the solution of interest (typically platinum for aqueous salts). Unless the resistance between the RE and WE is zero, the addition of a CE does not entirely stop the current flow through the RE.[2, 3]

1.3. Mass transport

The case of the electrochemically driven reduction of electroactive species O to R as shown in equation 1.1 is considered. If the rate of reaction is limited by the rate that species O moves towards or species R moves away from the WE surface, then the reaction is said to be mass transport controlled.

Mass transport to the WE surface can be broken down into three categories; diffusion, convection, and migration. When a system is under mass transport control the flux can be described by the Nernst-Plank equation[2-4] which combines the

contribution of diffusion, convection and migration terms respectively as shown in equation 1.10:[2-4]

$$J = -D\nabla c + c\mathbf{V} - \frac{zF}{RT_m} Dc\nabla\phi \qquad \textbf{(1.10)}$$

where D is the diffusion coefficient of the electroactive species, ∇ is the vector differential operator, c is the concentration of electroactive analyte, $\mathbf{V}$ is the velocity of the solution, z the charge on the analyte, R the gas constant, T_m the temperature, and ϕ the electrostatic potential.

1.3.1. Migration

Migration is the movement of a charged species under the influence of an electric field. Within an electrolyte solution the electric double layer at an electrode surface creates an electrical shielding, exponentially decreasing the strength of the electric field upon the ion with respect to distance from electrode.[1-3] For example the observed potential (ϕ) 10 nm away from the electrode has decayed to less than 1% of the original potential step (ϕ_0) in a 1:1 electrolyte at a concentration of 0.1 mol dm^{-3} according to equation 1.11.[2]

$$\frac{\tanh(ze\phi / 4\kappa T_m)}{\tanh(ze\phi_0 / 4\kappa T_m)} = e^{-\kappa x} \qquad \textbf{(1.11)}$$

Where tanh is the hyperbolic tangent, e is the charge on an electron, κ is the Boltzmann constant, x is the distance from the electrode surface (cm) and K is defined by equation 1.12,

$$K = (3.29\times10^{7})zc_b^{1/2} \quad \textbf{(1.12)}$$

where c_b is the bulk concentration.

At supporting electrolyte concentrations of 0.1 mol dm^{-3} and higher the potential drop is significant across the first 10 nm of the double layer. For example at a supporting electrolyte concentration of 0.1 mol dm^{-3} observed electrostatic potential is close to zero at ~10 nm from the electrode surface. As the concentration increases to 1 mol dm^{-3} the observed electrostatic potential is approximately zero observed electrostatic potential at 5 nm from the WE surface. As a result the current contribution due to migration is negligible within is thesis (equation 1.10). Therefore the contribution due to migration can be ignored within this thesis.

1.3.2. Diffusion Controlled

In a static solution where mass transport due to convection is negligible and migration has been suppressed, movement of electroactive species from the bulk of the solution to the electrode surface is controlled by diffusion. Diffusion is the movement of species down a concentration gradient. The rate that a species moves due to diffusion is proportional to the concentration gradient, as described by Fick's first law of diffusion for a 1D system, equation 1.13,[2, 3]

$$J = D\frac{\partial c(x,t)}{\partial x} \tag{1.13}$$

where $\frac{\partial c(x,t)}{\partial x}$ is the concentration gradient at a specific point in the x direction at a given time, where the x axis is perpendicular to the electrode surface. Figure 1.5 illustrates the time-dependant concentration profile due to diffusion at an electrode surface under conditions where at $x = 0$, $c = 0$ and where $t_3 > t_2 > t_1$; the diffusion layer thickness is defined as the distance which the concentration changes from 0 to c_b. As the concentration gradient decreases, the flux of the species towards the electrode surface decreases. The time-dependant expansion of the diffusion layer depends upon the experimental conditions employed.

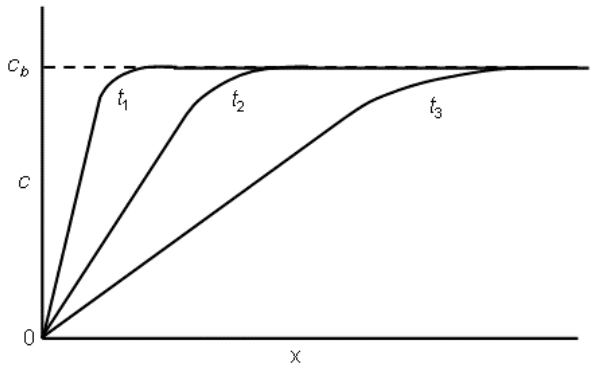

Figure 1.5 The concentration profile within the diffusion layer for a system where the rate of ET is limited by diffusion to the electrode surface.

When Fick's laws are considered in more than one dimension the WE geometry plays a significant effect upon the concentration gradient. Several geometries important to work within this thesis are summarised below.

Figure 1.6(a) shows a 2D representation of a disc macroelectrode, where a flat electrode, assumed to be uniformly active, is embedded within a co-planar insulating surface. When the reaction is driven at the electrode surface the local concentration of the mediator is decreased, creating a difference in concentration from the bulk concentration. Assuming diffusive mass transport control, the ET reaction will proceed at a rate greater than the rate of diffusion to the WE surface. With time the diffusion layer grows. For a macroelectrode the expanding concentration gradient creates a predominantly linear diffusion profile as the contribution due to edge diffusion is small in comparison to the linear diffusion to the WE surface. Over time the expansion of the diffusion layer results in a reduced flux to the electrode surface. This is observed in a CV as a peak current as mass transport cannot support the increasing rate of ET at the electrode surface. For CA measurements, stepping from a potential where no reaction occurs to a potential where ET is diffusion-controlled, the current response can be described by the Cottrell equation (equation 1.14),[2, 3]

$$i_t = \frac{nFAD^{1/2}c_b}{\pi^{1/2}t^{1/2}} \qquad \textbf{(1.14)}$$

where i_t is the current response with respect to time, and c_b is the bulk concentration of the redox active analyte.

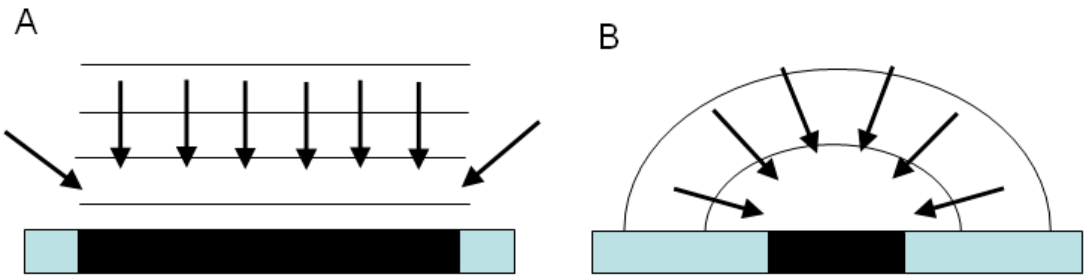

Figure 1.6 Schematic of the diffusion profiles (black lines) caused by (a) the cross section through a macro disc electrode and (b) the cross section of a disc ultra micro electrode.

If the dimensions of the electrode are reduced to the micrometer scale, then diffusion to the edges of the electrode becomes significant. A disc or hemispherical electrode of diameter less than 100 μm is often referred to as an ultramicroelectrode (UME).[12-14] The developed diffusion profile to a UME disc electrode imbedded co-planar within an insulator is shown in figure 1.6 (b). At short times, after a potential has been applied to the electrode which is suitable to initiate diffusion controlled electrolysis, the UME initially behaves as a macroelectrode, where an initial linear profile is established. With time the contribution of edge diffusion to the linear diffusion regime results in a hemispherical concentration profile. The diffusion controlled flux is thus greater for an UME than for a macroelectrode. The initial diffusion regime can be predicted using the Cottrell equation for semi-infinite linear diffusion (equation 1.14) and holds until the diffusional edge effects significantly contribute to the flux to the electrode surface.[15] When edge diffusion becomes significant the flux to the UME surface deviates from that predicted by the Cottrell equation and reaches a steady state where the diffusion layer thickness becomes

constant.[16] The current response for both regimes of a UME can be predicted by the Shoup-Szabo equation (equation 1.15 to equation 1.17),[17]

$$i_t = \frac{4nFADc_b}{\pi r} f(\tau) \quad \textbf{(1.15)}$$

$$f(\tau) = 0.7854 + 0.8862\tau^{-1/2} + 0.2146e^{-0.7823\pi^{-1/2}} \quad \textbf{(1.16)}$$

$$\tau = \frac{4Dt}{r^{1/2}} \quad \textbf{(1.17)}$$

where r is the radius of the disc. Figure 1.7 shows the effect of edge diffusion upon the time-dependant current response at a UME as predicted by the Shoup-Szabo equation, compared to linear diffusion only, predicted by the Cottrell equation.

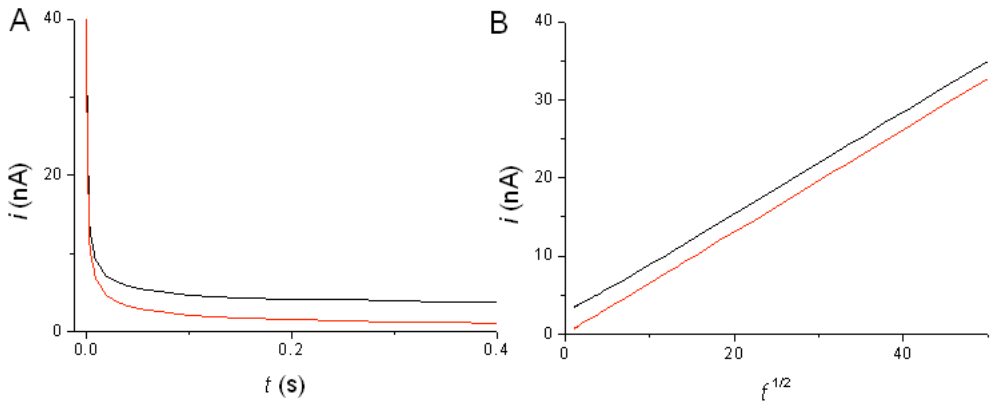

Figure 1.7 Comparison of the Cottrell predicted response (-) to the Shoup-Szabo equation (-) for a disc electrode of r = 12.5 µm, D = 6 x 10^{-6} cm s^{-1}, and c_b = 1 x10^{-3} mol dm^{-3}.

The above cases consider diffusion to an individual electrode within an infinite insulating plane. However if multiple electrodes are present the diffusion profiles to the electrodes can become perturbed. The developing diffusion profiles for two

UMEs positioned so that the diffusion profiles will overlap on a typical timescale is shown in figure 1.8.[18-20] Initially the diffuse layer expands at each UME as described previously for an individual UME (profiles 1-3). As the diffuse layer expands with time the presence of the diffusion field associated with the neighbouring UME perturbs the regular hemispherical profile; an effect referred to as diffusional overlap. This is shown in profiles 4 and 5 of figure 1.8. As time progresses overlap results in an essentially linear profile.[21, 22] As the thickness of the diffusion layer is dependant upon the diffusion coefficient of the electroactive analyte and geometry of the UME employed the critical inter-electrode spacing for diffusional overlap is dependant on the experimental conditions utilised.[20]

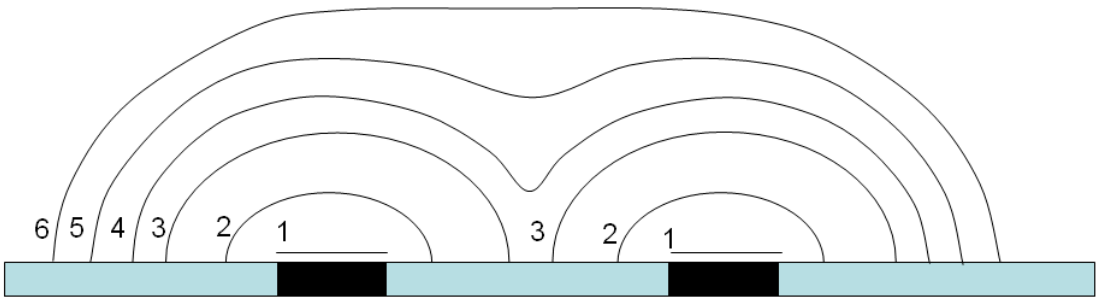

Figure 1.8 The expansion of the diffuse layer with time to two UMEs, profiles 1-6 represent the movement of c_b away from the electrode surface with time. Profile 1 represents the initial linear diffusion, profiles 2 and 3 show the establishment of hemispherical diffusion to the individual UMEs, profiles 4 and 5 show diffusional overlap occurring, and profile 6 shows the development of a diffusion profile similar to the profile that would be obtained if the central insulating region was active.

Expanding the two electrode example further to an array of UMEs where complete diffusional overlap is possible on the timescale of the electrochemical experiment, a measured current response is the same as that for an entirely active macroelectrode of the same geometric area. If the conditions are such so that

diffusional overlap does not occur (*e.g.* UMEs are spaced sufficiently far apart) then the array will maintain the characteristic electrochemical response of an UME (*e.g.* a CV with a limiting current for a mass transport controlled reaction), however the overall current response will be the sum of the currents from each individual UME in the array. Simulations of uniform[21] and random[22] UME arrays have been used to visualise the diffusional profiles to arrays. A significant advantage of using the array geometry is the reduction in the active electrode area compared to an electrode of the same geometric area (*i.e.* including the insulator area), resulting in the capacitance of the array system being smaller.[23] The reduced non-Faradaic background signal provides an enhancement in the signal-to-noise levels allowing for lower concentrations to be detected than for a conventional all active electrode material.[24]

1.3.3. Convection and Diffusion

Convection is the physical motion of a solution, and as described by the Nernst-Planck equation (equation 1.10), contributes to mass transport to an electrode surface. The combination of convection and diffusion to increase and vary the rate of mass transport to an electrode surface is particularly valuable in electroanalysis. Hydrodynamic control has been used to (a) increase the signal-to-noise ratio,[25-28] (b) for trace level detection,[29, 30] and (c) for kinetic studies.[31-37] Figure 1.9 shows the effect on the CV response of a macroelectrode of increasing mass transport using convection. Under diffusion only conditions, the typical peak-shaped current-voltage response can be observed, figure 1.9 (a). Under convective control the size of the diffuse layer is reduced compared to diffusion only conditions, and the convective contribution increases the current response as predicted by the Nernst-Planck

equation. When the convective term dominates the electrochemical response a steady-state response is typically observed due to the increased mass transport, figure 1.9 (b).

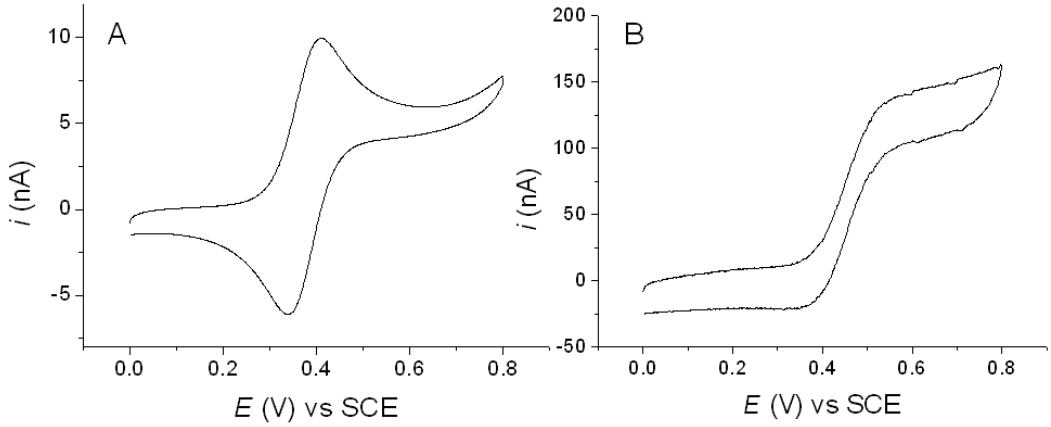

Figure 1.9 CVs showing the effect of increasing mass transport to a macro-electrode, (a) diffusion controlled, (b) convection and diffusion.

The velocity profile within a convective system can be simulated using the Navier-Stokes equations for momentum balance (equation 1.18) and continuity (equation 1.19),

$$\rho \mathbf{V} \cdot \nabla \mathbf{V} = -\nabla (p + \eta (\nabla \mathbf{V} + (\nabla \mathbf{V})^T)) \quad \textbf{(1.18)}$$

$$\nabla \cdot \mathbf{V} = 0 \quad \textbf{(1.19)}$$

where ρ is the density of water (assumed reasonably to be 1.00 g cm^{-3}),[38] $\mathbf{V}$ is the velocity vector, p is pressure, η is the dynamic viscosity of water, which is reasonably 1.00 mPa s for the experimental conditions used herein, and T is the total pressure (Pa). The Navier-Stokes equations are derived from Newton's second law of motion and assume that the solution is incompressible. All simulations of velocity within this

thesis are performed by applying equation 1.18 and equation 1.19 within a finite element model of the system, which will be discussed in more detail in chapters 4 and 6.

1.4. Hydrodynamic Methods

There are different methods for generating and controlling convection to the surface of the electrode. Typically these techniques involve the movement of either the electrode with respect to the solution or by inducing motion in the solution. Specific examples are described below.

1.4.1. Laminar and Turbulent Convection

Laminar flow within a cylindrical pipe has a velocity profile that is greatest along the centre of the pipe and decreases as the distance from the centre (r) increases (figure 1.10 (a)).[39] The solution is considered to flow perpendicular to r, as such the radial decrease in velocity along the channel is thought of as a series of concentric rings or lamina around the centre of the pipe. Turbulent flow is the chaotic motion of solution, where the motion of solution at a particular point is not predictable as for laminar flow, and is shown schematically in figure 1.10 (b). Whether a solution is laminar or turbulent depends upon the velocity of the solution, the geometry of the hydrodynamic system and the viscosity of the solution and is described by the Reynolds number (Re) of the system.[39]

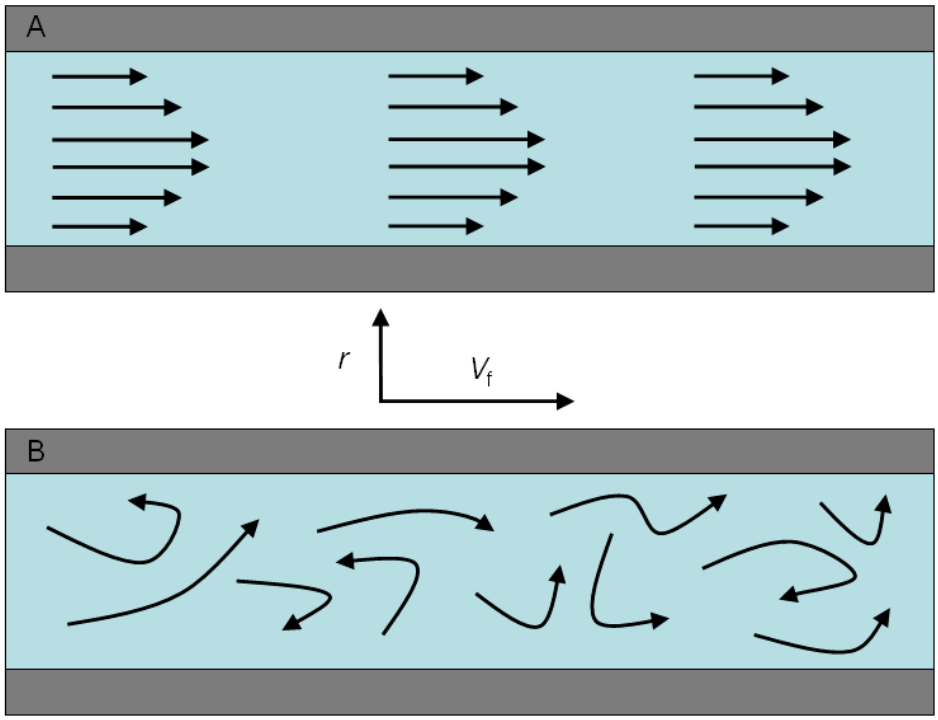

Figure 1.10 (a) 2D schematic of a laminar velocity profile within a pipe and (b) turbulent flow within a pipe. Size and direction of arrows represents local velocity.

1.4.2. Rotating Electrodes

The rotating electrode provides well defined hydrodynamics to the electrode surface.[40, 41] Common electrode geometries for the rotating electrode include the rotating disc electrode (RDE),[42] and the rotating ring disc electrode (RRDE).[43, 44] The WE is mounted centrally within a cylindrical insulating material and attached to a motor. By rotating the electrode, solution is drawn into the centre of the electrode before flowing outwards. The coefficient of mass transport (k_t) to the electrode surface for a RDE can be quantified using equation 1.20,[2]

$$k_t = 1.554 D^{2/3} W^{1/2} v^{-1/6} \quad \textbf{(1.20)}$$

where W is the rotation frequency and v is the solution viscosity. The flow profile at the RDE is shown in figure 1.11.

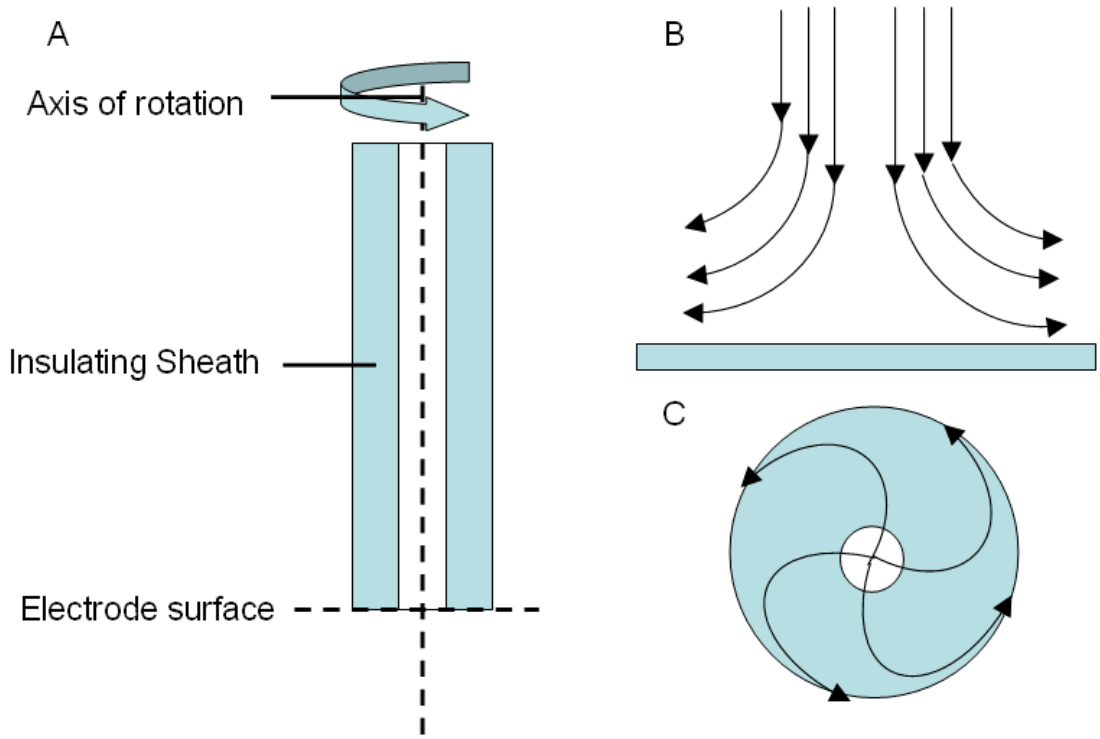

Figure 1.11 (a) A cross section of a RDE and the flow profile with respect to a rotating disc electrode surface, (b) perpendicular to the surface and, (c) in the plane of the surface.

Due to the enhanced mass transport to the electrode surface the rotating electrode geometries have been a fundamental tool for electrochemically investigating reaction kinetics.[45-49] The RRDE has been successfully modified with enzyme films[50-52] and with polymer films[53-55] to allow the catalytic effects of the films to be studied beyond the limit of diffusion, under well defined hydrodynamic control. More recently, the RDE has proved a popular technique for investigating fuel cell catalysts and other

electro-catalysts.[56-59] However due to the mechanical motion of the electrode the ability to access higher rotation rates is limited by how quickly the electrode can be rotated whilst maintaining an electrical contact, typically an upper limit of ~300 Hz.[60]

1.4.3. Channel and Tubular Flow

The tubular and channel flow cells for electrochemical detection typically consist of an electrochemical detector situated within a cylindrical pipe (a) or a rectangular duct (b), as illustrated in figure 1.12.

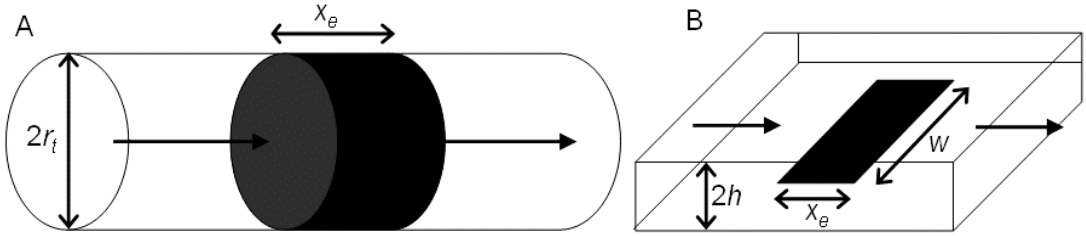

Figure 1.12 Schematics showing the key dimensions of (a) a tubular flow cell and (b) a channel flow cell

In theory, laminar flow occurs in tubes and channels when Re, defined in equation 1.21, is less than 2000[39]

$$\mathrm{Re} = \frac{\bar{U}\, D_h}{v} \qquad \textbf{(1.21)}$$

$\bar{U}$ is the mean fluid velocity (cm s^{-1}), v is the kinematic viscosity (~0.01 cm^2 s^{-1} for water at 20 °C),[38] and D_h is the hydraulic diameter (cm), which is dependant upon the channel geometry and dimensions.

For the case of the tubular flow cell it is important to know the radius (r_t) of the cylinder and the electrode length (x_e). The radius can be used to predict if flow within the pipe will be Laminar or turbulent by substituting the values calculated for $\bar{U}$ and D_h from equation 1.22 and equation 1.23 respectively, into equation 1.21.[39]

$$\bar{U} = \frac{V_f}{\pi r^2} \quad \textbf{(1.22)}$$

$$D_h = 2r_t \quad \textbf{(1.23)}$$

where V_f is the volume flow rate ($cm^3\ s^{-1}$).

For a channel flow electrode the critical dimensions are the channel height ($2h$), width (w) and electrode length (x_e). The values for $\bar{U}$ and D_h can be calculated from equation 1.24 and equation 1.25 for a channel flow electrode,

$$\bar{U} = \frac{V_f}{2hw} \quad \textbf{(1.24)}$$

$$D_h = \frac{8hw}{2h + w} \quad \textbf{(1.25)}$$

Once flow has been determined to be well-developed and laminar the current response can be predicted by equation 1.26 for a pipe[61] and equation 1.27 for a rectangular channel,[61]

$$i_{lim} = 5.43nFc_b D^{2/3} V_f^{\ 1/3} x_e^{\ 1/3} \quad \textbf{(1.26)}$$

$$i_{lim} = 1.165nFc_b D^{2/3} \bar{U}^{1/3} h^{-1/3} w x_e^{\ 2/3} \quad \textbf{(1.27)}$$

The approximations made for both tubular and channel flow electrodes are that there are no mass transport edge effects to the electrode (*e.g.* a band electrode is not near a side wall), mass transport to the electrode is dominated by uniform convective flow within the channel or pipe, and that the reaction at the electrode is mass-transport limited.

Originally pipe flow electrodes consisted of insulating delivery and waste pipes that were secured to a metal ring, or metal piping.[62] This effectively gave the electrode no lead-in length from the change of delivery pipe to electrode, which could result in the flow at the electrode surface not being fully developed and laminar in nature. Stulik *et al.*[63] presented a multipart tubular electrode (TE) consisting of two main Teflon sections. The electrode section is readily assembled by sandwiching metal foils between these Teflon supports which fit into the electrode housing; typically the foils are pierced post assembly to ensure a smooth interface (figure 1.13). Similar designs have been adopted, however to simplify the design the reference and counter electrodes are typically positioned outside of the main Teflon body.[64, 65]

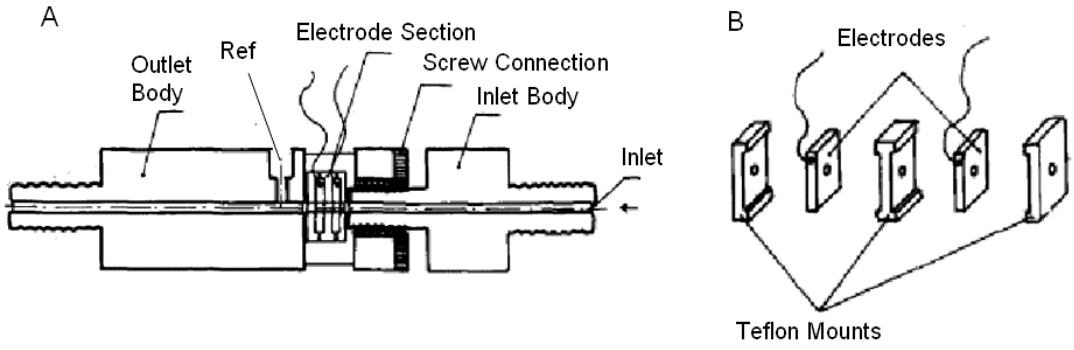

Figure 1.13 (a) Schematic of an assembled multipart TE cell where (b) is the dismantled electrode section, showing two electrodes. [63]

An alternative design involves imbedding the electrode within an insulating support that can be attached to the delivery and waste pipes.[66] Typically this approach involves sealing a metal ring inside a resin. This design methodology has very recently been further refined where the material for electrode and insulator is the same; in this case intrinsic and boron doped diamond (BDD) to create an intrinsic (insulating) diamond entry channel that feeds directly to a BDD electrode ring.[67]

The tubular electrode has been applied to low concentration detection using constant flow,[62] pulsed flow,[68] and stripping analysis.[65] The TE geometry is amenable to the continuous monitoring of an analytical solution for long periods of time.[63] The combination of electron spin resonance (ESR) with the tubular electrode has also facilitated the study of reaction kinetics.[69]

Theoretically the axial symmetry of a pipe is very appealing, allowing an axially symmetric 2D approximation of the flow system to be established.[70] Experimentally, the pipe system suffers from several drawbacks. For example, cleaning the electrode is difficult if abrasion is required as the electrode sits within the pipe. The surface roughness within the TE cannot be assessed by conventional topographic techniques (*e.g.* atomic force microscopy), and refraction at the curved electrode surface and variable path length through the cross section of the tube can be problematic for optical spectroscopy. These drawbacks make the channel flow geometry an experimentally appealing alternative due to the electrode being easily accessible, planar, and the uniform cross section of a channel.

The channel flow cell is amenable to many electroanalytical experiments and can be easily combined with spectroscopic techniques. The channel flow electrode allows for on-line and flow injection analysis of analyte concentration,[71-73] and has also found considerable use for kinetic and mechanistic studies of electrode processes,[74-77]

homogenous kinetics,[78, 79] dissolution studies and general reactions at solid/liquid interfaces.[33, 35, 80-87] These fundamental studies and related comprehensive treatments of mass transport in channel electrodes[88, 89] have provided a foundation for the recent use of channel flow in microfluidic devices[90, 91] and also for the characterisation of fuel cell catalysts.[37] A particularly attractive feature of the channel flow electrode is the possibility of making simultaneous spectroscopic measurements using, for example, UV-visible spectroscopy[77] and electron paramagnetic resonance.[74,69, 92, 93]

The channel flow cell is typically constructed from either a two part assembly or more commonly, a three part assembly. The three part assembly, illustrated in figure 1.14, consists of a planar electrode forming the channel base, a spacer part that forms the four side walls of the channel and defines the length, width, and height of the channel, with the third part providing the inlet and outlet ports and completes the channel roof.[61, 94] The two part design is made from a planar electrode base and a second piece that provides the inlet, outlet and remaining five channel walls. Importantly, both designs allow easy access to the electrode surface to allow cleaning and post experimental studies. The methodologies for constructing these types of channel are discussed in more detail in chapter 4.

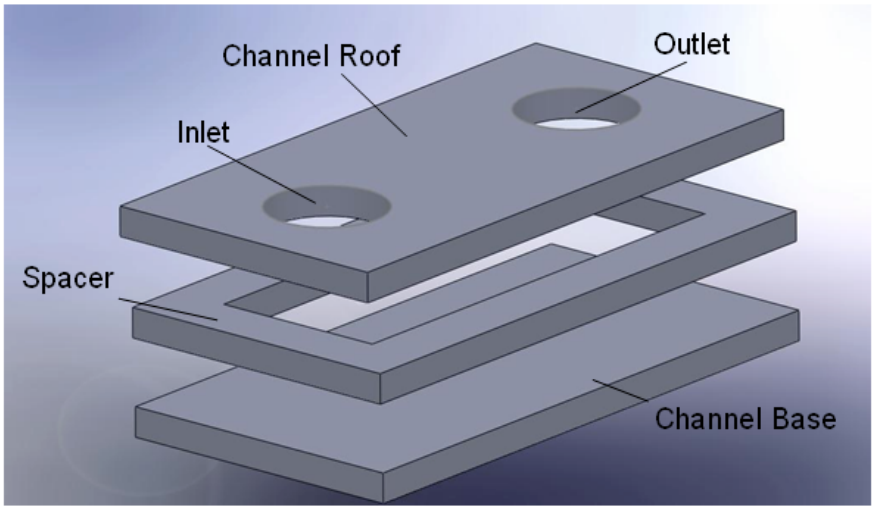

Figure 1.14 Schematic of a three part channel flow cell design where the electrode is incorporated in the channel base, a spacer defines the height and width of the channel, and the channel roof incorporates the inlet and outlet connections

1.4.4. Impinging Jet Electrodes

The impinging jet electrode (IJE) controls convection by fluid exiting a nozzle perpendicular to the electrode surface. The jet of fluid flows radially away from the centre of the nozzle. Depending on the wall thickness of the nozzle, and the height above the electrode surface, the radial flow profile is either undistorted,[95] or distorted due to the formation of a "thin layer cell" wall jet configuration, *i.e.* the nozzle is close to the surface and the nozzle wall thickness is large.[96, 97] The schematics and flow profiles of these two types of IJEs are shown in figure 1.15.

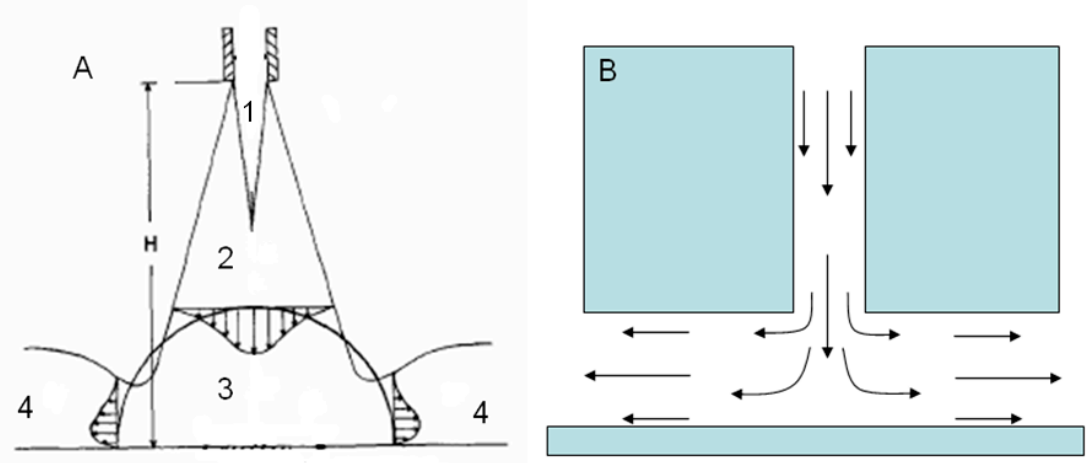

Figure 1.15 (a) Schematic of an impinging jet electrode with a small nozzle in relation to the size of the substrate the jet impinges on showing the four predicted flow zones.[98] (b) A large nozzle outer diameter close to the electrode surface showing the formation of a thin layer cell and distortion of the flow profile in (a).

For the case of figure 1.15 (a) four regions exist within the flow profile; (1) the zone where solution exits the nozzle, known as the potential core; (2) a region of laminar axial flow towards the electrode; (3) a stagnation zone, directly underneath the nozzle, and (4) a developed radial flow zone, where solution flows outwards decreasing in velocity.[98] The same regions exist in figure 1.15 (b) but are distorted by the proximity of the nozzle side walls compared to figure 1.15 (a). The hydrodynamics of both these cases have been solved analytically[98, 99] and are analysed in detail using finite element modelling, shown in chapter 6.

In addition to the two hydrodynamic geometries there are two limiting cases that depend upon the location and size of the WE on the substrate with respect to the flow profile of the IJE. The situation where the WE extends into the fully developed radial flow regime within an IJE is called the wall jet electrode (WJE),[100, 101] shown in figure 1.16 (a). Here the electrode is always bigger than the nozzle. If the WE is located fully within the stagnation zone, figure 1.16 (b), then the term wall tube electrode

(WTE) is used.[102-104] The WE is typically smaller than the nozzle for the WTE geometry.

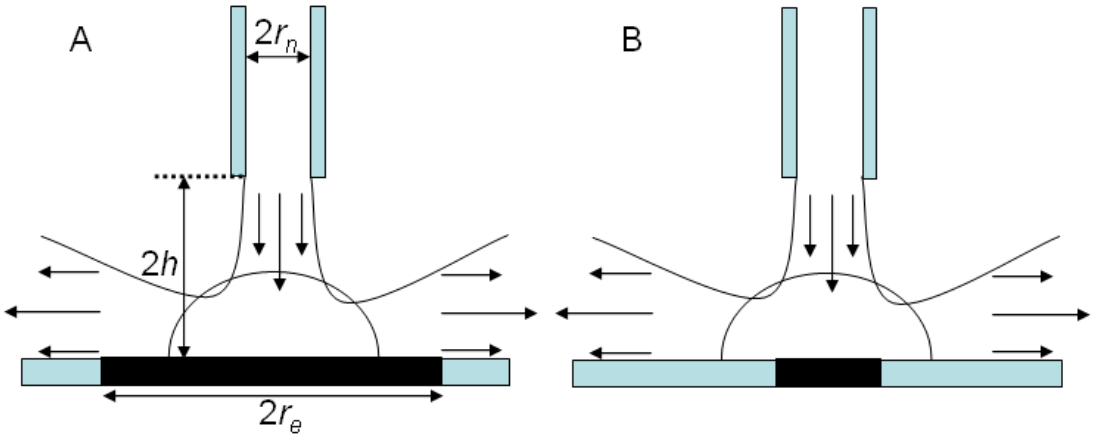

Figure 1.16 representation of a wall jet electrode (a) and a wall tube electrode (b)

The flux to the WE in the WJE is not uniform and decays with the radial decrease in fluid velocity. For the WJE the limiting current response can be described by equation 1.28,[105]

$$i_{\text{lim}} = \frac{1}{38} nF c_{\text{b}} D^{2/3} V_f{}^{3/4} r_n{}^{3/4} v^{-5/12} r_e{}^{-1/2} \qquad \textbf{(1.28)}$$

where r_n and r_e are the radii of the nozzle and electrode respectively.

Importantly, the assumptions that the concentration is not perturbed at the centre of the electrode, and that the nozzle does not interfere with the radial flow profile are made. These assumptions are adequate for the treatment of a WJE where the contribution to the overall current from the centre of the electrode is negligible and where the hydrodynamics are not distorted by the experimental setup. For the WTE the current contribution close to the axis of symmetry contributes significantly to the

measured limiting current response. At sufficiently high volume flow rates the WTE behaves similarly to a uniformly accessible electrode,[106, 107] and the current response can be predicted using equation 1.29.[36, 98, 108]

$$\frac{i_{WTE}}{i_{UME}} = \alpha \overline{U}^{1/2} \pi r_e^{\,2} D^{2/3} \nu^{-1/6} r_n^{\,-1/2} c_b \left(\frac{\pi}{4}\right)\left(\frac{2h}{r_n}\right)^{-0.054} \qquad \textbf{(1.29)}$$

where α is a constant coefficient (determined to be 1.51 by Chin and Tsang,[98] and Macpherson *et al.*[108]). Numerical investigations of the WTE have been performed by finite element modelling.[102, 104, 109]

The IJE is typically employed as an end of column detector in flow through detection,[110-114] *e.g.* high performance liquid chromatography (HPLC).[115, 116] As for the channel electrode the increased mass transport due to convection has also allowed kinetic and mechanistic studies to be performed.[117-120]

The combination of a UME in the IJE setup is referred to as a micro jet electrode (MJE). This set-up is analogous to the WTE except that both the nozzle and the WE are miniaturised, typically a UME of 25 μm and nozzle 100 μm are employed.[102, 104, 114, 115, 121] This method deserves particular attention due to the greatly increased mass transport it provides. Diffusional mass transport to an UME is already greater than that to a macro electrode, as discussed above, but when employed in the MJE setup the steady-state current can be increased by up to two orders of magnitude enabling k_t values of 0.5 cm s^{-1} to be generated. A RDE would have to rotate at 200 kHz to achieve a similar k_T which is practically impossible.[36, 108] Thus the increased mass transport makes this system particularly powerful for fast kinetic studies and the electroanalysis of heterogeneous reactions.[106]

Furthermore, by attaching the nozzle to piezo positioners it is possible to image the hydrodynamic profile of the MJE at the UME by recording the limiting current as a function of *x* and *y* nozzle position. [102, 106, 108] By using a UME as the WE the local mass transports can be probed, this allows the lower rate of convection directly under the centre of the nozzle, the stagnation zone, to be probed. As figure 1.17 shows the stagnation zone[98] is clearly visible with figure 1.17 (b) showing a central area of low current. The maximum current, and hence highest rate of mass transport, occurs when the electrode is offset from the centre of the nozzle. The locations that provide the maximum limiting current to the UME is a ring centred on the nozzle. As the distance of the UME from the centre of the nozzle increases, the mass transport to the UME decreases. This results in the observed decrease in the limiting current.[106]

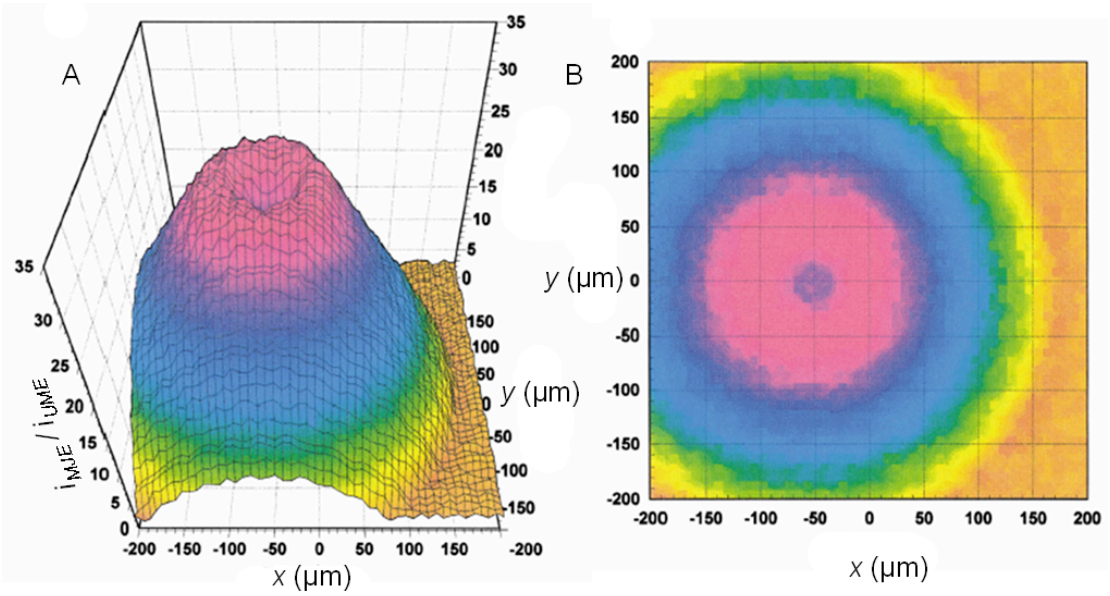

Figure 1.17 (a) 3D plot showing the variation of the steady-state current response of a UME at different positions within an impinging jet, (b) 2D plot highlighting the stagnation zone in the centre of the impinging jet (colours relate to currents from (a)). Note: Centre of jet at x = -50 µm, y = 0 µm.[106]

Figure 1.17 demonstrates the variation in mass transport with respect to the radial position of the electrode from the centre of the nozzle. Equation 1.28 assumes that the

electrode is positioned centrally within the impinging jet, as any offset will not provide the electrode with the axially symmetric radial flow from the impinging jet. Equation 1.29 assumes that the electrode is sufficiently smaller than the nozzle so that the mass transport to the electrode surface is effectively constant across the surface; however figure 1.17 demonstrates that due to the stagnation zone this is a rough approximation.

The IJE geometries have proven to be powerful electroanalytical devices in a variety of configurations. Typically the nozzle or WE is mounted on a stage with *x*, *y* and *z* controllers, as shown in figure 1.18 (a). Alternatively, it is possible to place the electrode on the nozzle itself and create a ring electrode which when brought close to the surface defines a "thin layer cell" arrangement. The "thin layer cell" ring electrode behaves similarly to a channel flow cell.[60] This geometry has been used to successfully probe fast heterogeneous ET kinetics.[122]

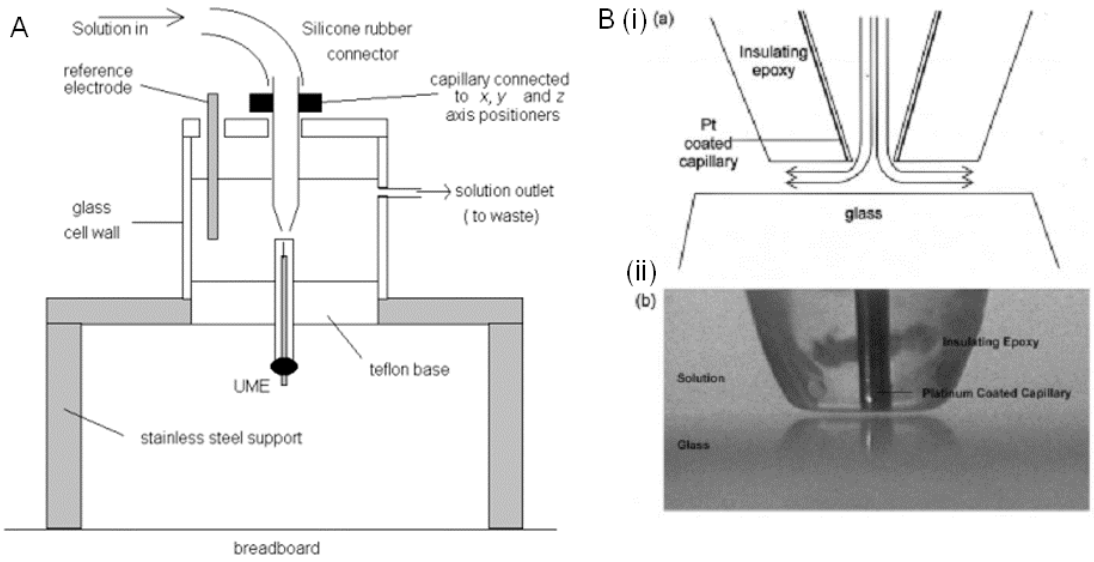

Figure 1.18 (a) Schematic of a wall jet cell with x,y, and z mobility of the nozzle and (b (i)) where the WE is a ring incorporated into the nozzle,[108] (b (ii)) is a photograph of the experimental setup.[60]

1.4.5. Modulation of Flow Rates

By varying the rate of mass transport discrimination between the background signal, and the current response due to the mediator of interest can be significantly enhanced.[123] This can provide an advantage over both (i) potential step voltammetric studies where the current time signal has a contribution from R_{Ω} and C and; (ii) CVs recorded at a low electroactive concentrations, where the redox signal can be obscured by the background current-voltage response.[124]

With hydrodynamic techniques it is easy to modulate the mass transport rate by varying the rate of convection, *e.g.* modulating the rate of stirring.[125] For the RDE the speed of rotation can be varied.[126] Wang *et al.*[127] and Miller *et al.*[128] demonstrated both (i) the stopped-rotation RDE, where the rotation rate was turned on and off, and (ii) modulated rotation RDE, where the rotation rate was varied from high to low rates. As the limiting current response for a RDE is dependant upon the rate of rotation of the electrode, by varying the rate of rotation, and hence the mass transfer rate, the difference in the limiting current response can be measured. By holding the WE at a fixed potential whilst modulating the rate of rotation the background signal remains constant (figure 1.19). This approach obtained the detection limits of ~40 nmol dm^{-3} for nitrobenzene on a gold electrode, and for Fe (II) – Fe (III) on a graphite electrode.[128]

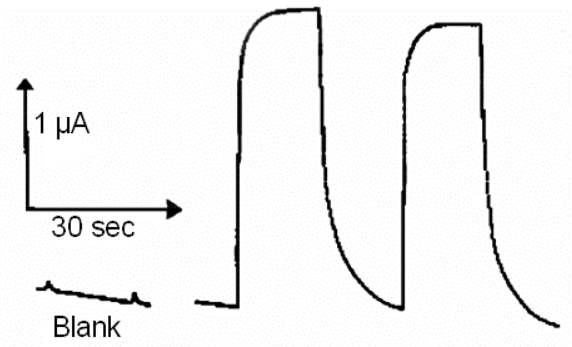

Figure 1.19 Example of a stopped-rotation RDE CA response for 7 µmol dm^{-3} ascorbic acid.[127]

For the channel flow, tubular flow cells with electrochemical detection and IJE configurations the volume flow rate can be varied.[36] The pulsed and stop flow techniques were initially employed by Blaedel and Boyer,[68, 129] where the rate of solution delivered through the channel was varied. Combining this technique with vitreous carbon discs enabled a detection limit of ~1 nmol dm^{-3} to be obtained for $Fe(CN)_6^{4-}$.[27] In addition to varying the volume flow rate, the IJE also provides the interesting possibility of varying the nozzle height over the electrode to create an oscillating rate of mass transport.[114] This technique was used to enhance the signal-to-noise for the "thin layer cell" micro ring electrode by oscillating the nozzle up and down and thus changing the height between electrode and a planar surface.[130]

An enhancement in detection limits similar to the stop-rotation method can be achieved by using an oscillating MJE. As shown in figure 1.17, by varying the **lateral** position (*i.e.* x and y) of the electrode with respect to the nozzle the limiting current response varies from that of an UME in static solution when the nozzle is not over the electrode (figure 1.20 (b)), to the convectively enhanced limiting current of an IJE configuration (figure 1.20 (a)). By oscillating the lateral position during a CV the change in the mass transport rates can be observed producing the oscillating

change in current observed in figure 1.20 (c). It is important to use UMEs with small insulating sheathes to minimise the lateral displacement of the nozzle. A detection limit of ~5 nmol dm^{-3} for $IrCl_6^{3-}$ on a Pt disc UME was obtained by Macpherson *et al.*.[121]

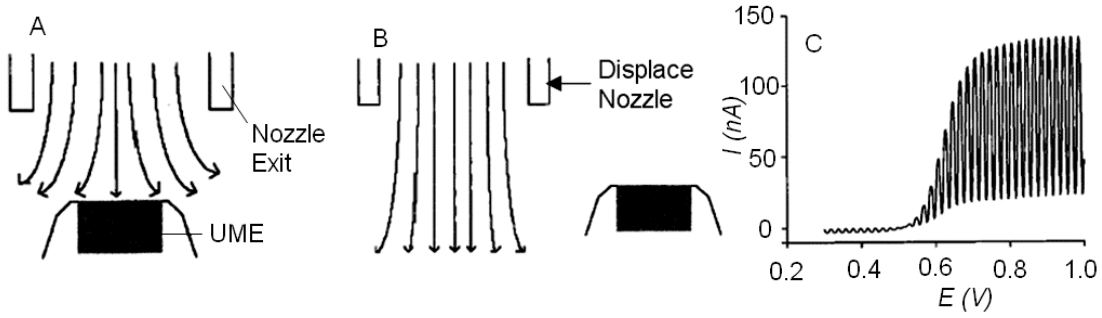

Figure 1.20 Schematic of the hydrodynamic profiles to a MJE where the UME has a small insulating sheath, (a) where the solution impinges directly onto the centre of the UME, (b) when the fluid does not impinge onto the substrate. (c) A typical CV produced by modulating the lateral position.[121]

1.5. Carbon as an Electrode Material

This section introduces carbon as a WE material, and discusses several of the commonly used forms of carbon. The carbon atom has six electrons, four of which are in the valence orbitals, allowing a carbon atom to form sp, sp^2 and sp^3 bonds.[131] Carbon covalently bonds to 4 atoms in the sp^3 hybridization, for example in diamond each carbon is bonded to 4 neighbouring carbon atoms a tetrahedral geometry. With a sp^2 hybridization carbon bonds to 3 neighbouring atoms in a planar triangle configuration, the fourth valence electron can be localised into a double bond (*e.g.* CH_2O), or delocalised in conjugated systems. In the sp bonding hybridization the

carbon atom bonds linearly to two atoms, forming a triple bond and a single bond, for example acetylene (C_2H_2).

Carbon materials, such as highly oriented pyrolytic graphite (HOPG), glassy carbon (GCE), and carbon fibre, have been used extensively as electrode materials as they offer many advantages over metallic electrodes.[132] For example, the chemical stability of carbon, the wide potential window[8] in aqueous solution, and biocompatibility with biological and organic redox mediators make these materials of electroanalytical interest.[133-136] The forms of carbon referred to and used within this thesis are discussed below, with an overall focus on carbon nanotubes (CNTs) for use as an electrochemical detector.

1.5.1. Highly Oriented Pyrolytic Graphite

This material is of particular importance throughout this thesis due to the analogies drawn between the surface sites of highly orientated pyrolytic graphite (HOPG) and CNTs. Figure 1.21 (a) shows the crystal structure of HOPG consisting of layers of sp^2 bonded planar hexagons, individually known as graphene (figure 1.21 (a i)).[132] As each carbon has only 3 neighbouring carbon atoms this leaves a dangling bond which weakly connects neighbouring planes together, (figure 1.21 (a ii)) and of particular importance for an electrode, allows conduction through the material.[137] Defects occur on the surface of HOPG, either in the disruption of the regular lattice structure, or where a graphene layer is broken forming step edges.[138] Figure 1.21 (b) shows the typical surface features of HOPG consisting of basal plane (sp^2) sites, which consist of the hexagonal structure of a graphene sheet and edge plane (sp^3) sites, which occur at step edges and constitute the end of a graphene sheet.[139, 140]

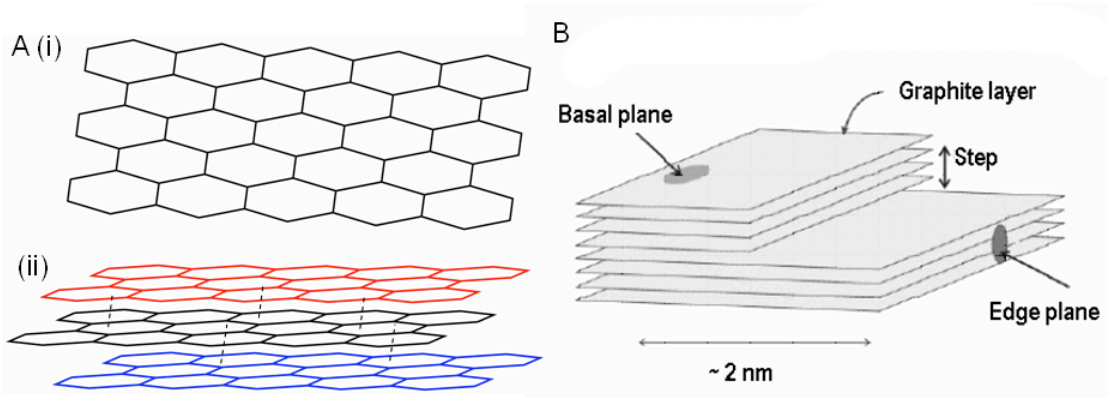

Figure 1.21 (a) The crystal structure of HOPG, (i) a single layer or graphene sheet, and (ii) three layers stacked, dashed lines represent weak bonding between the plances, (b) illustrates the surface features of HOPG.[138]

HOPG is synthesised by the high temperature decomposition of hydrocarbons, typically acetylene, followed by hot pressing at a high temperature and high pressure.[132] The regular lattice structure and nano-meter flat surface over extended regions of HOPG makes the material surface appealing for a range of studies. The well defined structure of HOPG provides an appealing surface for investigations into controlling the morphology and quantity of metal nano-particles deposited on a carbon surface using electrodeposition techniques.[141-144] HOPG has also been used as a carbon support for investigations into the catalytic effect of electrodeposited nanoparticles for fuel cell investigations.[145, 146] For example the extended flat surface of HOPG facilitates the combination of atomic force microscopy (AFM) and scanning electrochemical microscopy to probe the catalytic properties of different metal nanoparticles to be for a variety of reactions (*e.g.* proton generation and oxygen reduction).[146]

However, there is still consideral debate about the electroactivity of the basal plane and edge sites on HOPG. Some claim that the electroactivity of HOPG is predominantly due to edge plane sites, with strongly hindered ET at the basal plane.[22, 147-150] However, others believe that the basal plane is able to support ET at significant rates.[5, 151, 152] This debate is of particular interest as the surface structure of HOPG has been considered as analogous to that of a CNT, and will be discussed in more detail in chapter 3.

1.5.2. Carbon Nanotubes

CNTs possess remarkable structural, mechanical and electronic properties, making CNTs of interest to a broad range of fields. These include the use of CNTs as probes in scanning probe microscopy,[153-157] composite materials,[158-160] nanoelectronics[161-164] and solar cell technology.[165, 166] The low resistance[167] and low capacitance[168] of "pristine" CNTs (*i.e.* clean and unpurified) makes them particularly attractive to electrochemistry and applications in electrochemical sensing.

The basic component of a CNT is considered analogous to a rolled graphene sheet, resulting in a single walled nanotube (SWNT) (figure 1.22 (a)), with a typical diameter between 0.5 - 3 nm.[169] A multi walled nanotube (MWNT), contains several layers of rolled graphene. For a SWNT the chiral vector, C_h, of the circumference of the SWNT determines whether the SWNT is metallic or semiconducting.[170, 171] The chiral vector is derived from equation 1.30,

$$C_h = n\mathbf{a_1} + m\mathbf{a_2} \qquad \textbf{(1.30)}$$

where $\mathbf{a}_1$ and $\mathbf{a}_2$ are vector components of the graphene sheet as defined in figure 1.22 (b), and *n* and *m* are integer values. Equation 1.31 can be used to determine if the SWNT is metallic or semiconducting.

$$\text{If } \frac{n-m}{3} = \text{integer} \text{ then the SWNT is metallic} \quad \textbf{(1.31)}$$

Thus for random growth probability dictates one out of three SWNTs will be metallic.

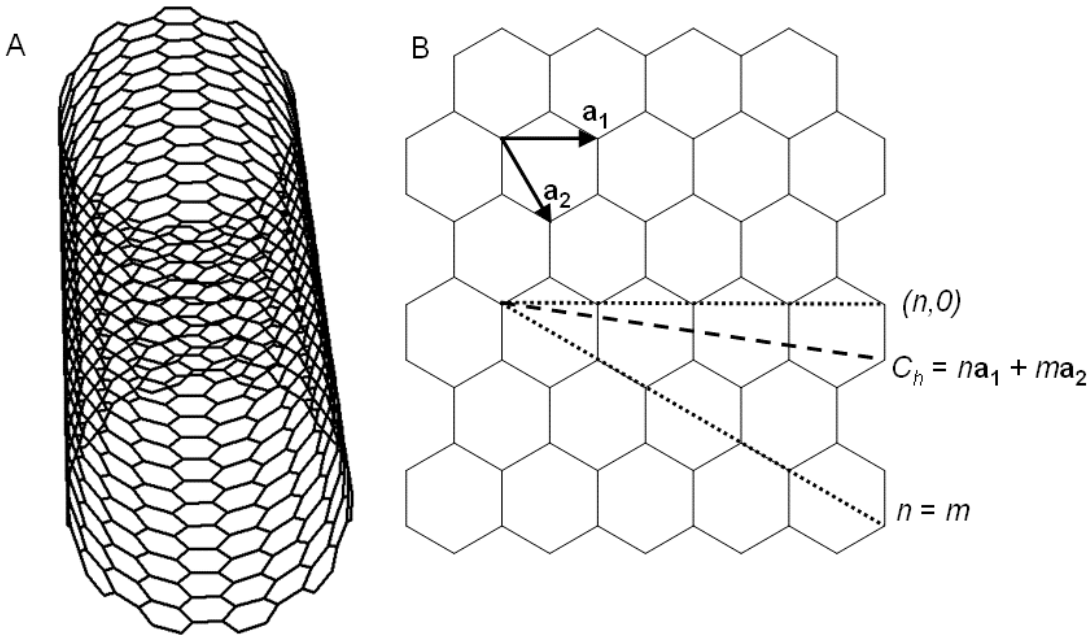

Figure 1.22 (a) A graphene sheet rolled to form a SWNT, (b) diagram illustrating the labelling conventions for the chiral vector of SWNT circumference.

Both SWNTs and MWNTs have been used for electrochemical studies, however it is important to note that as a SWNT consists of one graphene sheet, effectively the

electrode is all surface atoms. In contrast a MWNT consists of many layers,[172] which can be arranged in different ways as shown in figure 1.23.[131, 147] Thus, when the layers are non-concentric the MWNT is referred to as herring bone or bamboo-like. Depending upon the structure of the MWNT employed for electrochemical studies the proportion of sidewall and step edge sites on the MWNT will vary. Thus it is essential CNTs are fully charaterised prior to use. This is even more important as the different synthesis and cleaning techniques employed will result in different CNT structures *e.g.* acid functionalised[173] and surfactant stabilised[174].

This thesis is primarily interested in the use of SWNTs as an electrode material, however as MWNTs have been used extensively for electrochemistry and for determination of the electroactivity of CNTs it is important to discuss both materials (chapter 3).

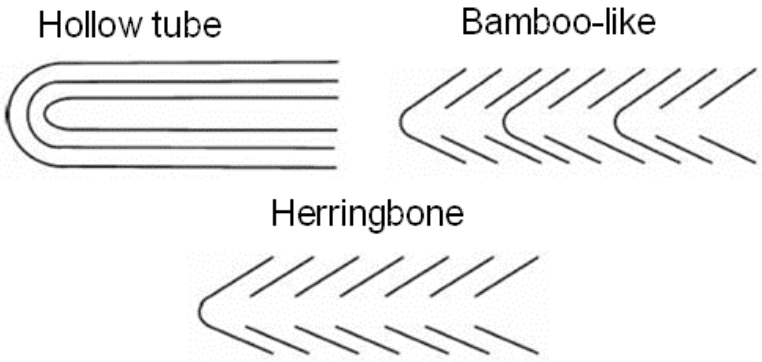

Figure 1.23 Various configurations of MWNTs (a) concentric, (b) bamboo and (c) herring bone[147]

1.5.3. Synthesis of Carbon Nanotubes

There are several methods for the synthesis of CNTs; arc discharge,[175-177] catalysed chemical vapour deposition (cCVD),[178-180] laser ablation[181, 182] and high

pressure carbon monoxide conversion (HiPCO).[183, 184] Arc discharge is the original method for fullerene[185] and CNT synthesis.[175] Here graphite electrodes are placed ~1 mm apart in an inert atmosphere and a bias of 10 – 35 V is applied to produce an electrical discharge, resulting in soot formation, which contains the CNTs and amorphous carbon. Metallic catalysts can be added to the anode to control the CNT composition, for example Co, Fe, Y and Ni are known to promote the growth of SWNTs.[177, 181, 186, 187] Due to the carbon on the anode being transferred to the cathode and surroundings the anode is progressively moved towards the cathode to maintain the separation distance. A major drawback of arc discharge is that the resultant product often has more than a 2:1 weight ratio of catalyst nanoparticles to CNTs.[188]

Laser ablation involves heating a graphite target which incorporates a metal catalyst, for example Co and Ni for the synthesis of SWNT,[189] to 1200 °C under an inert gas flow, CNTs are produced by directing Nd:YAG laser pulses onto the carbon source. Depending on where the product forms inside the oven the yield of CNTs to amorphous carbon varies from ~90% to under 50%.[182, 189]

HiPCO was developed at Rice university by Smalley *et al*[169, 184, 190] with the aim to mass produce SWNTs. The HiPCO method involves the flow of a carbon containing gas mixed with a catalyst in the vapour phase (*e.g.* $Fe(CO)_5$ in CO)[184] through an oven heated to ~1000 °C at 1-10 atm of pressure. The SWNTs form in the gas flow and are removed either from a collection area or from the furnace walls.[184] The produced SWNTs typically have catalyst residue on the sidewall with a density of approximately 1 metal atom per 10 carbon atoms.[184] As with arc discharge and laser ablation the HiPCO CNTs need post-growth purification in order to remove the catalyst and carbon residues. It is important to note that many early electrochemical

studies used unpurified CNTs and were effectively making measurements on composite materials (*e.g.* CNTs/metal nanoparticles/amorphous carbon).[191, 192]

Synthesis of CNTs by cCVD produces CNTs with little amorphous carbon and is thus considered a clean process.[193, 194] Also one catalyst nano particle yields one SWNT and the catalyst nano particle is typically encapsulated in the SWNT thus the metal nano particle contamination is minimised. The method will be described in detail in the section 2.1. Figure 1.24 outlines the general cCVD methodology, where a substrate loaded with catalyst particles is heated inside an oven under the flow of hydrogen, argon and a carbon feedstock gas. After a defined period of time the substrate is cooled and removed from the oven.[178, 195] This technique is used exclusively for the in-house synthesis of SWNTs used for the electrochemical studies herein. This is a direct result of the SWNTs containing negligible amounts of amorphous carbon, having a low defect density[196] and the fact they can be directly synthesised on the substrate of interest.[152, 195, 197-199]

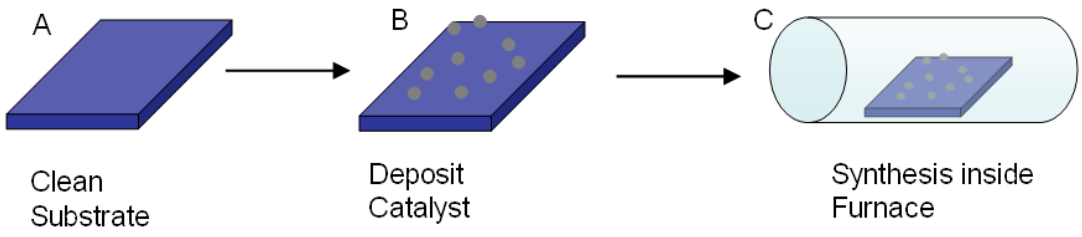

Figure 1.24 Outline of the basic method for synthesising CNTs by cCVD where (a) the clean substrate has catalyst deposited upon the surface (b), before (c) being placed inside the cCVD furnace.

1.5.4. Purification of CNTs

As SWNTs synthesised by arc discharge, laser ablation and HiPCO are formed in soot containing a high proportion of undesired material (*e.g.* catalyst particles and amorphous carbon) the CNTs are typically purified prior to use in electroanalysis.

Purification of CNTs is typically performed using strongly acidic solutions at elevated temperatures.[200-203] Acid cleaning of SWNTs provides a significant reduction in the amount of impurities however it does not always remove all of the impurities and thus post cleaning characterisation is essential.[204-206] Dumitrescu *et al.*[207] demonstrated how an acid reflux CNT treatment step caused the reduction in length of CNTs (figure 1.25) and functionalises the outer wall. Vibrational spectroscopy studies indicates acid treatment provides a mixture of C-O and C=O functional groups on the sidewall of the SWNT.[208-210] Functionalising the sidewall disrupts the regular structure of the CNT, in the case of metallic SWNTs this could result in points of higher resistance.[211, 212]

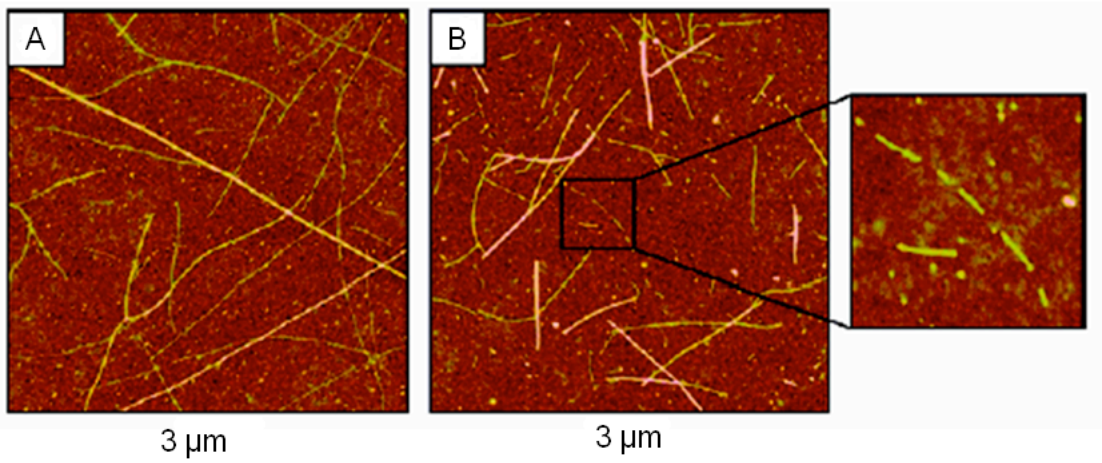

Figure 1.25 AFM images showing SWNTs (a) prior to treatment and (b) after 14 hours reflux treatment in HNO_3.[207]

Ultra sound treatment of CNTs is typically used during the cleaning of CNTs and for the separation of CNTs. The sonic treatment can damage the CNT structure resulting in the shortening of the CNTs.[173, 174, 213] For the creation of drop cast films a surfactant can be used to prevent aggregation, *e.g.* sodium dodecylsulfate (SDS)[214] or benzylalkonium chloride.[215] The surfactant can be difficult to remove, or like acid cleaning, functionalise the outer wall.[172]

1.5.5. Carbon Nanotubes as Electrodes

The first reported use of CNTs as an electrode material was for the detection of dopamine in 1996 by Britto *et al.*[191] The CNTs were prepared by arc discharge and made into a paste with bromoform. The electrode was prepared by packing the CNT/bromoform paste into a glass tube. An electrical contact was made by inserting a copper or platinum wire into the paste. This method provided a reversible electrochemical response for the electrolysis of dopamine upon a large capacitive background signal as shown in figure 1.26.

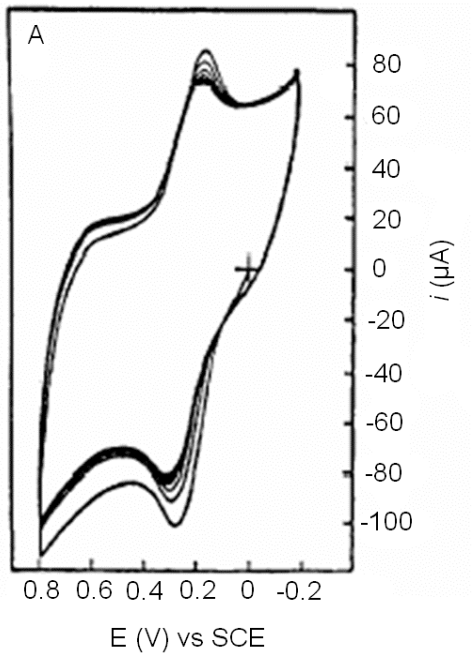

Figure 1.26 CV of 5 mM dopamine in PBS (pH 7.4) at a carbon nanotube electrode (sweep rate, 20mV s^{-1} reference electrode, SCE).[191]

As an alternative to making a CNT-paste electrode, CNT samples have been drop cast onto conducting supports (*e.g.* metals[174, 216, 217] and glassy carbon[218, 219]). Luo *et al.*[218] showed that deposition of CNTs onto a glassy carbon support resulted in improved sensitivity towards dopamine detection compared to a bare glassy carbon electrode. These early reports indicated an enhanced electrochemical signal which was attributed to the presence of the CNTs. However, work by Moore *et al.*[220] on modified basal plane HOPG showed that the same electrochemical enhancement for several redox species could be achieved using either an abrasively attached graphitic powder or a drop cast MWNT film (>95% purity). This report questioned the previously claimed "electrocatalytic effects" of CNTs[221] and highlighted the need to fully characterise the electrode material being used for structure and purity.

It should be noted that drop cast deposition procedures require suspending the CNT solution in an organic solvent or with a surfactant which coat the CNT, and the

use of sonication which can damage the structure of the CNT.[174, 213] Also the method produces an uneven distribution of CNTs across the surface; resulting in clumps of CNTs[218]. Finally the use of an electrochemically active support makes discrimination of the electrochemical response due to the CNTs alone difficult.

Importantly these treatment steps can be avoided by the use of cCVD for the synthesis of SWNTs directly onto an insulating substrate. Individual SWNT,[151, 199] array SWNT[222, 223] and random 2D network SWNT[152, 195] electrodes have been prepared this way. For example, work by Bertoncello *et al.*[196] demonstrated that the use of a SWNT 2D network covering less than 1% of the surface of the underlying insulating substrate produced an electrode, figure 1.27 (a), with greatly reduced capacitive currents compared to a glassy carbon electrode of the same geometric dimensions (figure 1.27 (b)). This enabled CV detection of the outer sphere redox mediator ferrocenylmethyl trimethylammonium hexaflorophosphate ($FcTMA^+$) at 25 nmol dm^{-3} directly using CV alone. The synthesis of SWNT 2D network UMEs was demonstrated by Dumitrescu *et al.*[224] and proved that the electrode behaved as a conventional UME but with the advantage of reduced capacitive currents.

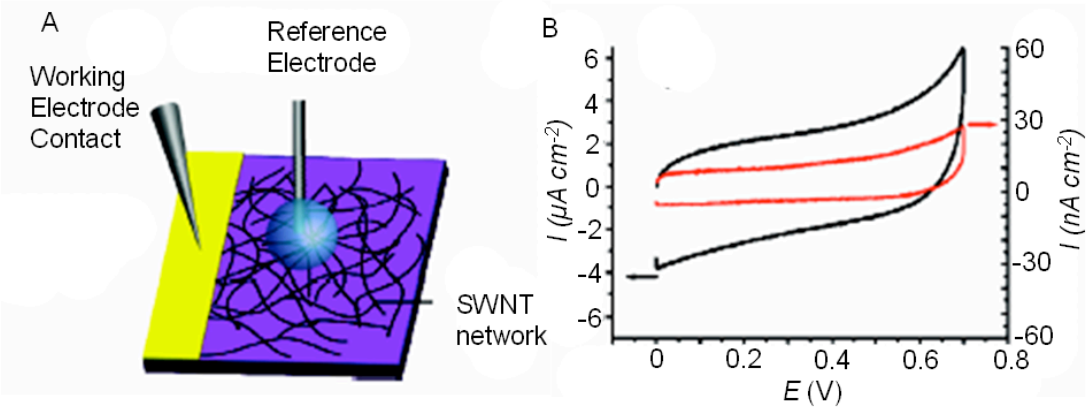

Figure 1.27 (a) Schematic of the droplet cell used on the 2D SWNT network, (b) the reduced capacitive background of the 2D SWNT network (-) compared to a GCE (-), note different current density scales.

However, despite the many applications of CNTs to electrochemistry there is still debate about where electron transfer occurs on a CNT and whether MWNTs and SWNTs can be treated in the same way, see chapter 3 for further discussion.

1.6. Finite Element Modelling

The theoretical prediction of the current response to an applied voltage at an electrode surface is performed using the finite element modelling (FEM) package FEMlab^{TM} (Comsol) in this thesis. This technique uses a computer to solve a defined set of equations (*i.e.* Fick's second law of diffusion and Navier-Stokes equations for the work within this thesis) within a user defined domain. For both 2D and 3D simulations the problem is broken down into a set of triangular elements, known as a mesh, which is used to approximate the domain being simulated (figure 1.28).[225, 226]

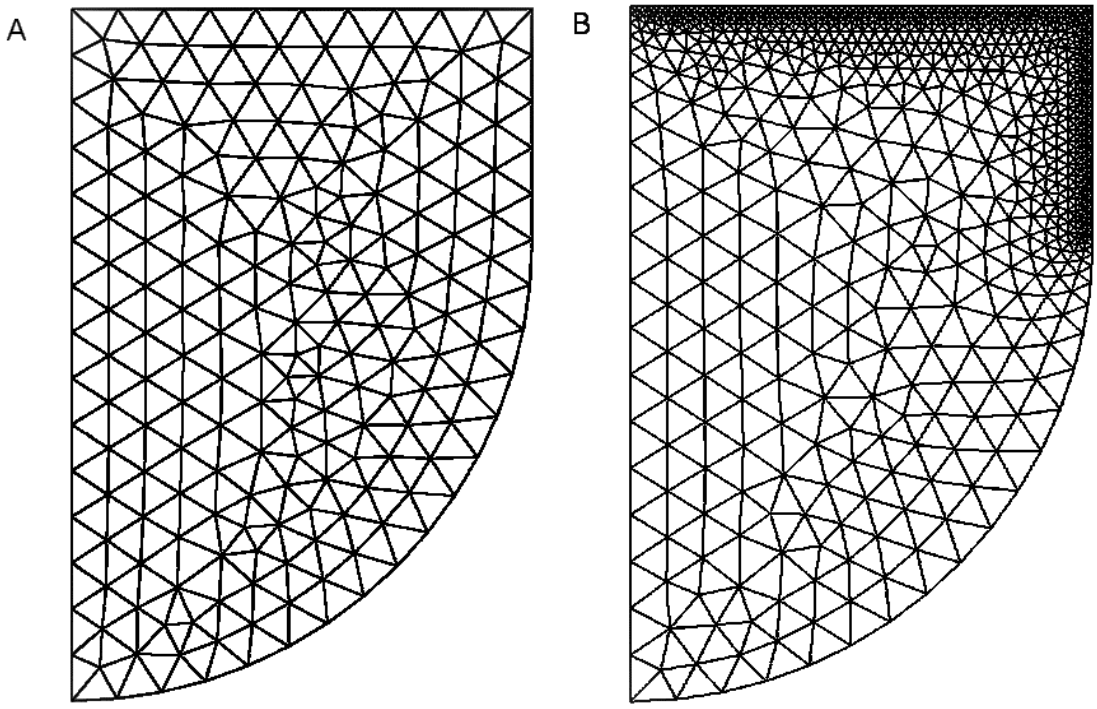

Figure 1.28 An example of a simple triangular mesh used for FEM (a) and the same domain where the mesh is finer at two edges (b)

After generating a mesh the chosen equations are calculated at the corners of each triangular element. For areas where the result is likely to change the most, for example a concentration gradient near an electrode surface, the mesh density is increased (figure 1.28 (b)). This can be either defined by the user or using an algorithm to focus on areas of greatest change in a property (*e.g.* fluid velocity and concentration). Both mesh refinement approaches allow simulations to be run efficiently without sacrificing accuracy.[102, 104, 109, 227] For situations where multiple sets of equations are being solved, the problem can be broken down into multiple domains. This technique is used in the 2D simulations of the wall jet electrode (section 6.3.8) to ensure a high level of accuracy for the predicted limiting currents.[99]

With the increasing power of computers the use of FEM within electrochemistry has risen.[228-231] For example Kwak and Bard[232] showed how FEM could be used to predict the limiting current response of an UME at different distances from a surface. Initially this was done for insulating and conducting cases[232] but now any surface reaction can be studied provided it can be approximated with the correct equations.[233] Work by Holder *et al.*[234] used FEM 3D modelling to explore the effect of probe tip and cantilever geometry for SECM-AFM studies. An adaptive mesh routine within the solver was used for the investigation of the current response at an electrode due to the increased mass transport caused by acoustic agitation of the solution.[235] The investigation of diffusional cross talk between micro-bands inside a channel flow cell.[236] Numerical simulations and experimental results were in agreement at both the electrodes in a dual micro band system, for both the generator-generator and generator-collector electrode modes over a range of flow rates and diffusion coefficients.[237] Norton *et al.*[238] applied FEM to the mass transport limited reduction or oxidation of bio-molecules in variable concentrations of supporting electrolyte. This approach also enabled the limiting current to be analysed for mediator species of different charge to be predicted. Grime *et al.*[239] showed that the proton transport across a lipid bilayer can be accurately modelled. Protons were generated at an UME and the pH was monitored by fluorescence microscopy. By analysing the experimental and theoretical data the permeation coefficient across the membrane was determined. The electrochemically induced transport across the interface of two immiscible liquids has been modelled by Qui *et al.*[240] In particular, the affect of the boundary layer geometry upon the CV response was investigated.

FEM has been used to investigate non-planar electrodes, for example the effect of having a disc or ring raised or recessed with respect to the surrounding insulating

surface. The resultant diffusion profiles established at the electrodes were predicted and the effect of the geometry studied.[241] FEM has also been employed for a range of hydrodynamic techniques, including IJEs,[99, 102-104, 242] and RDEs.[243, 244] The technique is particularly powerful for situations where the electrode does not experience a uniform flow profile, or the hydrodynamics are distorted from a conventional or idealised set up (*e.g.* a hindered RDE[243]).

The FEM calculations performed throughout this thesis are based upon Fick's second law of diffusion[2, 3] and incompressible Navier-Stokes fluid mechanics.[39] Simulations will be described in more detail in their relevant sections.

1.7. Thesis Aims

The use of CNTs within electrochemistry is a growing field, with a wide range of techniques for synthesis and applications as electrode materials. Despite the increased use of CNTs within electrochemistry there is still debate about the sites of ET at the CNT surface. Some claim that the step edge-like defects, catalyst particles and amorphous carbon all contribute, whilst the sidewall remains effectively inert, although there is evidence to the contrary, which indicates the sidewall is active. One of the main aims of this thesis is to investigate the sites of ET at well characterised SWNT electrode systems. In conjunction with this work the use of SWNTs for ultra-low concentration detection has also been explored. This has involved the construction of new flow cells which are compatible with the SWNT network electrodes employed and a full characterisation of the hydrodynamics of the resultant flow devices.

In more detail; chapter 2 discusses the experimental techniques used throughout this thesis, in particular the synthesis and characterisation of SWNT networks for use as electrode materials. The fabrication techniques for a range of electrode materials are introduced. The microstereo lithography (MSL) process is described for applications to create novel hydrodynamic devices. Finally, a list of all chemicals and the purities employed throughout the work herein is given.

The sites for electron transfer at a SWNT network electrode are investigated in chapter 3. By reducing the rate of diffusion to the electrode using a drop-cast Nafion^{TM} film, it is possible to distinguish between defect and sidewall electroactivity. Theoretical models for the two limiting cases of discrete site activity and entire sidewall activity are proposed and critically compared to experimental data.

Chapter 4 introduces current methods for channel flow cell construction, where the advantages and disadvantages of all are considered. The design and development of an improved flow cell using MSL is presented and rigorously tested on both gold and polycrystalline boron doped diamond band electrodes. The channel produced is amenable to mass production, and importantly for analytical applications is easily assembled and does not distort during assembly. The FEM simulation is compared to the Levich predicted response for several electrode geometries. Chapter 5 describes the employment of the MSL produced flow cell in conjunction with SWNT network electrodes. This combination is used for the low concentration detection of $FcTMA^+$ and dopamine.

Chapter 6 continues the application of MSL produced hydrodynamic devices with the development of a MSL fabricated IJE. FEM is used to determine the hydrodynamics in a range of configurations, ensuring that the MSL IJE device provides well-defined radial flow to an electrode surface. FEM is also used to predict

the limiting current response for the experimental testing of the flow cell. This device is compared to existing IJE experimental set-ups, and is used experimentally in conjunction with both metal and SWNT network electrodes.

Finally chapter 7 summarises the findings of chapters 3-6, and proposes future work based upon the designs presented.

1.8. References

(1) Fisher, A. C. *Electrode Dynamics*; Oxford Science Publications: Oxford, 1996.
(2) Bard, A. J.; Faulkner, L. R. *Electrochemical Methods*, 2nd ed.; John Wiley and Sons: New York, 2001.
(3) Brett, C. M. A.; Brett, A. M. O. *Electrochemistry Principles*; Oxford Press: Oxford, 1993.
(4) Compton, R. G.; Sanders, G. H. W. *Electrode Potentials*; Oxford Science Publications: Oxford, 2006.
(5) Edwards, M. A.; Bertoncello, P.; Unwin, P. R. *The Journal of Physical Chemistry C* **2009**, *113*, 9218.
(6) Bockris, J. O. M.; Devanathan, M. A. V.; Muller, K. *Proceedings of the Royal Society of London. Series A. Mathematical and Physical Sciences* **1963**, *274*, 55.
(7) McGaw, E. A.; Swain, G. M. *Analytica Chimica Acta* **2006**, *575*, 180.
(8) Pleskov, Y. V. *Russian Journal of Electrochemistry* **2002**, *38*, 1275.
(9) Chialvo, A. C.; Triaca, W. E.; Arvia, A. J. *Journal of Electroanalytical Chemistry* **1983**, *146*, 93.
(10) Farebrother, M.; Goledzinowski, M.; Thomas, G.; Birss, V. I. *Journal of Electroanalytical Chemistry* **1991**, *297*, 469.
(11) Hutton, L.; Newton, M. E.; Unwin, P. R.; Macpherson, J. V. *Analytical Chemistry* **2009**, *81*, 1023.
(12) Wightman, R. M.; Wipf, D. O. *Electroanalytical Chemistry* **1989**, *15*, 267.
(13) Deakin, M. R.; Wipf, D.; Wightman, R. M. *Journal of the Electrochemical Society* **1986**, *133*, C135.
(14) Wightman, R. M. *Analytical Chemistry* **1981**, *53*, 1125.
(15) Bard, A. J.; Denault, G.; Friesner, R. A.; Dornblaser, B. C.; Tuckerman, L. S. *Analytical Chemistry* **1991**, *63*, 1282.
(16) Heinze, J. *Angewandte Chemie-International Edition in English* **1993**, *32*, 1268.
(17) Shoup, D.; Szabo, A. *Journal of Electroanalytical Chemistry* **1982**, *140*, 237.
(18) Amatore, C.; Saveant, J. M.; Tessier, D. *Journal of Electroanalytical Chemistry* **1983**, *147*, 39.
(19) Shoup, D.; Szabo, A. *Journal of Electroanalytical Chemistry* **1984**, *160*, 19.

(20) Gueshi, T.; Tokuda, K.; Matsuda, H. *Journal of Electroanalytical Chemistry* **1978**, *89*, 247.
(21) Davies, T. J.; Ward-Jones, S.; Banks, C. E.; del Campo, J.; Mas, R.; Munoz, F. X.; Compton, R. G. *Journal of Electroanalytical Chemistry* **2005**, *585*, 51.
(22) Davies, T. J.; Moore, R. R.; Banks, C. E.; Compton, R. G. *Journal of Electroanalytical Chemistry* **2004**, *574*, 123.
(23) Penner, R. M.; Martin, C. R. *Analytical Chemistry* **1987**, *59*, 2625.
(24) Cheng, I. F.; Martin, C. R. *Analytical Chemistry* **1988**, *60*, 2163.
(25) Jedral, W. *Journal of Electroanalytical Chemistry* **1988**, *251*, 349.
(26) Rees, N. V.; Klymenko, O. V.; Coles, B. A.; Compton, R. G. *Journal of Electroanalytical Chemistry* **2003**, *557*, 99.
(27) Blaedel, W. J.; Wang, J. *Analytical Chemistry* **1979**, *51*, 799.
(28) Blaedel, W. J.; Yim, Z. *Analytical Chemistry* **1980**, *52*, 564.
(29) Economou, A.; Voulgaropoulos, A. *Talanta* **2007**, *71*, 758.
(30) Wang, J.; Musameh, M. *Analytica Chimica Acta* **2004**, *511*, 33.
(31) Wang, Z. H.; Scherson, D. *Journal of the Electrochemical Society* **1995**, *142*, 4225.
(32) Fosdick, L. E.; Anderson, J. L. *Analytical Chemistry* **1988**, *60*, 156.
(33) Rosset, E.; Datta, M.; Landolt, D. *Journal of Applied Electrochemistry* **1990**, *20*, 69.
(34) Bernstein, C.; Heindrichs, A.; Vielstich, W. *Journal of Electroanalytical Chemistry* **1978**, *87*, 81.
(35) Orton, R.; Unwin, P. R. *Journal of the Chemical Society-Faraday Transactions* **1993**, *89*, 3947.
(36) Macpherson, J. V.; Simjee, N.; Unwin, P. R. *Electrochimica Acta* **2001**, *47*, 29.
(37) Seidel, Y. E.; Schneider, A.; Jusys, Z.; Wickman, B.; Kasemo, B.; Behm, R. J. *Faraday Discussions* **2008**, *140*, 167.
(38) Lide, D. R. *CRC Handbook of Chemistry and Physics*; CRC Press: USA, 2001.
(39) Nakayama, Y. *Introduction to Fluid Mechanics*; Arnold, 1999.
(40) Bruckenstein, S.; Miller, B. *Accounts of Chemical Research* **1977**, *10*, 54.
(41) Miller, B.; Bruckens.S *Journal of the Electrochemical Society* **1970**, *117*, 1032.
(42) Riddiford, A. C.; Delahay, P., Ed.; Wiley-Interscience: New York, 1966; Vol. 4, pp 7.
(43) Albery, W. J.; Robert Svanberg, L.; Wood, P. *Journal of Electroanalytical Chemistry* **1984**, *162*, 29.
(44) Albery, W. J.; Drury, J. S.; Hitchman, M. L. *Transactions of the Faraday Society* **1971**, *67*, 2162.
(45) Frumkin, A.; Nekrasov, L.; Levich, B.; Ivanov, J. *Journal of Electroanalytical Chemistry* **1959**, *1*, 84.
(46) Anastasijevic, N. A.; Vesovic, V.; Adzic, R. R. *Journal of Electroanalytical Chemistry* **1987**, *229*, 305.
(47) Morrison, B.; Striebel, K.; Ross, P. N.; Andricacos, P. C. *Journal of Electroanalytical Chemistry* **1986**, *215*, 151.
(48) Hofseth, C. S.; Chapman, T. W. *Journal of the Electrochemical Society* **1992**, *139*, 2525.
(49) Okajima, T.; Ohsaka, T.; Hatozaki, O.; Oyama, N. *Electrochimica Acta* **1992**, *37*, 1865.

(50) Kamin, R. A.; Wilson, G. S. *Analytical Chemistry* **1980**, *52*, 1198.
(51) Lindgren, A.; Munteanu, F. D.; Gazaryan, I. G.; Ruzgas, T.; Gorton, L. *Journal of Electroanalytical Chemistry* **1998**, *458*, 113.
(52) Kulys, J.; Drungiliene, A.; Wollenberger, U.; Krikstopaitis, K.; Scheller, F. *Electroanalysis* **1997**, *9*, 213.
(53) Oyama, N.; Anson, F. C. *Analytical Chemistry* **1980**, *52*, 1192.
(54) Gopalan, A. I.; Lee, K. P.; Manesh, K. M.; Santhosh, P.; Kim, J. H. *Journal of Molecular Catalysis a-Chemical* **2006**, *256*, 335.
(55) Manesh, K. M.; Santhosh, P.; Gopalana, A. L.; Lee, K. P. *Electroanalysis* **2006**, *18*, 1564.
(56) Thorum, M. S.; Yadav, J.; Gewirth, A. A. *Angewandte Chemie-International Edition* **2009**, *48*, 165.
(57) Bae, S. E.; Stewart, K. L.; Gewirth, A. A. *Journal of the American Chemical Society* **2007**, *129*, 10171.
(58) Li, X.; Gewirth, A. A. *Journal of the American Chemical Society* **2003**, *125*, 7086.
(59) Ye, H.; Crooks, J. A.; Crooks, R. M. *Langmuir* **2007**, *23*, 11901.
(60) Macpherson, J. V.; Unwin, P. R. *Analytical Chemistry* **1998**, *70*, 2914.
(61) Compton, R. G.; Unwin, P. R. *Journal of Electroanalytical Chemistry* **1986**, *205*, 1.
(62) Blaedel, W. J.; Olson, C. L.; Sharma, L. R. *Anal. Chem.* **1963**, *35*, 2100.
(63) Stulik, K.; Hora, V. *Journal of Electroanalytical Chemistry* **1976**, *70*, 253.
(64) Meschi, P. L.; Johnson, D. C. *Analytical Chemistry* **1980**, *52*, 1304.
(65) Schieffer, G. W.; Blaedel, W. J. *Analytical Chemistry* **1977**, *49*, 49.
(66) Albery, W. J.; Coles, B. A.; Couper, A. M. *Journal of Electroanalytical Chemistry* **1975**, *65*, 901.
(67) Vidotti, M.; Unwin, P. R.; Macpherson, J. V. *In Prep.*
(68) Blaedel, W. J.; Boyer, S. L. *Analytical Chemistry* **1971**, *43*, 1538.
(69) Albery, W. J.; Chadwick, A. T.; Coles, B. A.; Hampson, N. A. *Journal of Electroanalytical Chemistry* **1977**, *75*, 229.
(70) Blaedel, W. J.; Klatt, L. N. *Analytical Chemistry* **1966**, *38*, 879.
(71) Trojanowicz, M. *Analytica Chimica Acta* **2009**, *653*, 36.
(72) Prado, C.; Murcott, G. G.; Marken, F.; Foord, J. S.; Compton, R. G. *Electroanalysis* **2002**, *14*, 975.
(73) Blaedel, W. J.; Wang, J. *Analytical Chemistry* **1979**, *51*, 1724.
(74) Compton, R. G.; Daly, P. J.; Unwin, P. R.; Waller, A. M. *Journal of Electroanalytical Chemistry* **1985**, *191*, 15.
(75) Wakabayashi, N.; Takeichi, M.; Uchida, H.; Watanabe, M. *Journal of Physical Chemistry B* **2005**, *109*, 5836.
(76) Rees, N. V.; Dryfe, R. A. W.; Cooper, J. A.; Coles, B. A.; Compton, R. G.; Davies, S. G.; McCarthy, T. D. *Journal of Physical Chemistry* **1995**, *99*, 7096.
(77) Wang, Z.; Zhao, M.; Scherson, D. A. *Analytical Chemistry* **1994**, *66*, 4560.
(78) Prieto, F.; Aixill, W. J.; Alden, J. A.; Coles, B. A.; Compton, R. G. *The Journal of Physical Chemistry B* **1997**, *101*, 5540.
(79) Thompson, M.; Klymenko, O. V.; Compton, R. G. *Journal of Electroanalytical Chemistry* **2005**, *576*, 333.
(80) Compton, R. G.; Sanders, G. H. W. *Journal of Colloid and Interface Science* **1993**, *158*, 439.
(81) Unwin, P. R.; Barwise, A. J.; Compton, R. G. *Journal of Colloid and Interface Science* **1989**, *128*, 208.

(82) Thompson, M.; Wilkins, S. J.; Compton, R. G.; Viles, H. A. *Journal of Colloid and Interface Science* **2003**, *259*, 338.
(83) Tsuru, T. *Materials Science and Engineering a-Structural Materials Properties Microstructure and Processing* **1991**, *146*, 1.
(84) Barwise, A. J.; Compton, R. G.; Unwin, P. R. *Journal of the Chemical Society-Faraday Transactions* **1990**, *86*, 137.
(85) Compton, R. G.; Unwin, P. R. *Philosophical Transactions of the Royal Society of London Series a-Mathematical Physical and Engineering Sciences* **1990**, *330*, 1.
(86) Ahmed, S.; Fonseca, S. M.; Kemp, T. J.; Unwin, P. R. *Journal of Physical Chemistry B* **2003**, *107*, 5892.
(87) Ahmed, S.; Kemp, T. J.; Unwin, P. R. *Journal of Photochemistry and Photobiology a-Chemistry* **2001**, *141*, 69.
(88) Anderson, J. L.; Moldoveanu, S. *Journal of Electroanalytical Chemistry* **1984**, *179*, 107.
(89) Compton, R. G.; Pilkington, M. B. G.; Stearn, G. M.; Unwin, P. R. *Journal of Electroanalytical Chemistry* **1987**, *238*, 43.
(90) Henley, I. E.; Fisher, A. C. *Journal of Physical Chemistry B* **2003**, *107*, 6579.
(91) Wain, A. J.; Compton, R. G.; Le Roux, R.; Matthews, S.; Fisher, A. C. *Analytical Chemistry* **2007**, *79*, 1865.
(92) Coles, B. A.; Compton, R. G. *Journal of Electroanalytical Chemistry* **1983**, *144*, 87.
(93) Tam, K. Y.; Wang, R. L.; Lee, C. W.; Compton, R. G. *Electroanalysis* **1997**, *9*, 219.
(94) Unwin, P. R.; Compton, R. G. In *Comprehensive Chemical Kinetics*; Compton, R. G., Hamnett, A., Eds.; Elsevier, 1989; Vol. 29, pp 173.
(95) Bouet, V.; Gabrielli, C.; Maurin, G.; Takenouti, H. *Journal of Electroanalytical Chemistry* **1992**, *340*, 325.
(96) Powell, F. E.; Fogg, A. G. *Analyst* **1988**, *113*, 483.
(97) Powell, F. E.; Fogg, A. G. *Electroanalysis* **1990**, *2*, 463.
(98) Chin, D. T.; Tsang, C. H. *Journal of the Electrochemical Society* **1978**, *125*, 1461.
(99) Bitziou, E.; Rudd, N. C.; Unwin, P. R. *Journal of Electroanalytical Chemistry* **2007**, *602*, 263.
(100) Yamada, J.; Matsuda, H. *Journal of Electroanalytical Chemistry* **1973**, *44*, 189.
(101) Albery, W. J.; Brett, C. M. A. *Journal of Electroanalytical Chemistry* **1983**, *148*, 201.
(102) Melville, J. L.; Coles, B. A.; Compton, R. G.; Simjee, N.; Macpherson, J. V.; Unwin, P. R. *Journal of Physical Chemistry B* **2003**, *107*, 379.
(103) Melville, J. L.; Simjee, N.; Unwin, P. R.; Coles, B. A.; Compton, R. G. *Journal of Physical Chemistry B* **2002**, *106*, 10424.
(104) Melville, J.; Simjee, N.; Unwin, P. R.; Coles, B. A.; Compton, R. G. *Journal of Physical Chemistry B* **2002**, *106*, 2690.
(105) Albery, W. J. *Journal of Electroanalytical Chemistry* **1985**, *191*, 1.
(106) Macpherson, J. V.; Beeston, M. A.; Unwin, P. R. *Journal of the Chemical Society-Faraday Transactions* **1995**, *91*, 899.
(107) Coeuret, F. *Chemical Engineering Science* **1975**, *30*, 1257.
(108) Macpherson, J. V.; Marcar, S.; Unwin, P. R. *Anal. Chem.* **1994**, *66*, 2175.

(109) Klymenko, O. V.; Gavaghan, D. J.; Harriman, K. E.; Compton, R. G. *Journal of Electroanalytical Chemistry* **2002**, *531*, 25.
(110) Brett, C. M. A.; Brett, A. M. O.; Mitoseriu, L. C. *Electroanalysis* **1995**, *7*, 225.
(111) Elbicki, J. M.; Morgan, D. M.; Weber, S. G. *Analytical Chemistry* **1984**, *56*, 978.
(112) Soucaze-Guillous, B.; Kutner, W. *Electroanalysis* **1997**, *9*, 32.
(113) Itagaki, M.; Tagaki, M.; Watanabe, K. *Journal of Electroanalytical Chemistry* **1997**, *440*, 139.
(114) Simjee, N.; Unwin, P. R.; Macpherson, J. V. *Electroanalysis* **2003**, *15*, 1445.
(115) Cannan, S.; Unwin, P. R. *Electroanalysis* **2004**, *16*, 712.
(116) Swartzfager, D. G. *Analytical Chemistry* **1976**, *48*, 2189.
(117) Brett, C. M. A.; Brett, A.; Pereira, J. L. C. *Electroanalysis* **1991**, *3*, 683.
(118) Brett, C. M. A.; Brett, A.; Fisher, A. C.; Compton, R. G. *Journal of Electroanalytical Chemistry* **1992**, *334*, 57.
(119) Compton, R. G.; Fisher, A. C.; Latham, M. H.; Brett, C. M. A.; Brett, A. *Journal of Physical Chemistry* **1992**, *96*, 8363.
(120) Compton, R. G.; Fisher, A. C.; Tyley, G. P. *Journal of Applied Electrochemistry* **1990**, *20*, 912.
(121) Macpherson, J. V.; Unwin, P. R. *Analytical Chemistry* **1999**, *71*, 4642.
(122) Macpherson, J. V.; Jones, C. E.; Unwin, P. R. *Journal of Physical Chemistry B* **1998**, *102*, 9891.
(123) Williams, D. E.; Macpherson, J. V. In *Comprehenisve Chemical Kinetics*; Compton, R. G., Hancock, G., Eds.; Elsevier, 1999; Vol. 37, pp 369.
(124) Wang, J. *Talanta* **1981**, *28*, 369.
(125) Wang, J. *Analytica Chimica Acta* **1981**, *129*, 253.
(126) Tokuda, K.; Bruckenstein, S.; Miller, B. *Journal of the Electrochemical Society* **1975**, *122*, 1316.
(127) Wang, J. *Analytical Chemistry* **1981**, *53*, 1528.
(128) Miller, B.; Bruckens.S *Journal of the Electrochemical Society* **1974**, *121*, 1558.
(129) Blaedel, W. J.; Iverson, D. G. *Analytical Chemistry* **1977**, *49*, 1563.
(130) Macpherson, J. V.; Unwin, P. R. *Analytical Chemistry* **1999**, *71*, 2939.
(131) Meyyappan, M., Ed. *Carbon Nanotubes: Science and Applications*; CRC Press, 2005.
(132) McCreery, R. L. *Chemical Reviews* **2008**, *108*, 2646.
(133) Wightman, R. M. *Science* **2006**, *311*, 1570.
(134) Venton, B. J.; Wightman, R. M. *Analytical Chemistry* **2003**, *75*, 414A.
(135) Qureshi, A.; Kang, W. P.; Davidson, J. L.; Gurbuz, Y. *Diamond and Related Materials* **2009**, *18*, 1401.
(136) Uslu, B.; Ozkan, S. A. *Analytical Letters* **2007**, *40*, 817.
(137) Wang, Y.; Alsmeyer, D. C.; McCreery, R. L. *Chemistry of Materials* **1990**, *2*, 557.
(138) Banks, C. E.; Compton, R. G. *Analyst* **2006**, *131*, 15.
(139) Chang, H. P.; Bard, A. J. *Journal of the American Chemical Society* **1991**, *113*, 5588.
(140) Chang, H. P.; Bard, A. J. *Langmuir* **1991**, *7*, 1143.
(141) Cherstiouk, O. V.; Simonov, P. A.; Savinova, E. R. *Electrochimica Acta* **2003**, *48*, 3851.
(142) McCreery, R. L.; Cline, K. K.; McDermott, C. A.; McDermott, M. T. *Colloids and Surfaces a-Physicochemical and Engineering Aspects* **1994**, *93*, 211.

(143) Liu, H.; Favier, F.; Ng, K.; Zach, M. P.; Penner, R. M. *Electrochimica Acta* **2001**, *47*, 671.
(144) Peruffo, M.; Contreras-Carballada, P.; Bertoncello, P.; Williams, R. M.; De Cola, L.; Unwin, P. R. *Electrochemistry Communications* **2009**, *11*, 1885.
(145) Lu, G. J.; Zangari, G. *Journal of Physical Chemistry B* **2005**, *109*, 7998.
(146) Kucernak, A. R.; Chowdhury, P. B.; Wilde, C. P.; Kelsall, G. H.; Zhu, Y. Y.; Williams, D. E. *Electrochimica Acta* **2000**, *45*, 4483.
(147) Banks, C. E.; Davies, T. J.; Wildgoose, G. G.; Compton, R. G. *Chemical Communications* **2005**, *7*, 829.
(148) Banks, C. E.; Moore, R. R.; Davies, T. J.; Compton, R. G. *Chemical Communications* **2004**, 1804.
(149) Kneten, K. R.; McCreery, R. L. *Analytical Chemistry* **1992**, *64*, 2518.
(150) Bowling, R. J.; Packard, R. T.; McCreery, R. L. *Journal of the American Chemical Society* **1989**, *111*, 1217.
(151) Heller, I.; Kong, J.; Heering, H. A.; Williams, K. A.; Lemay, S. G.; Dekker, C. *Nano Letters* **2005**, *5*, 137.
(152) Quinn, B. M.; Dekker, C.; Lemay, S. G. *Journal of the American Chemical Society* **2005**, *127*, 6146.
(153) Wilson, N. R.; Cobden, D. H.; Macpherson, J. V. *The Journal of Physical Chemistry B* **2002**, *106*, 13102.
(154) Gardner, C. E.; Macpherson, J. V. *Analytical Chemistry* **2002**, *74*, 576A.
(155) Wong, S. S.; Woolley, A. T.; Odom, T. W.; Huang, J. L.; Kim, P.; Vezenov, D. V.; Lieber, C. M. *Applied Physics Letters* **1998**, *73*, 3465.
(156) Wong, S. S.; Woolley, A. T.; Joselevich, E.; Cheung, C. L.; Lieber, C. M. *Journal of the American Chemical Society* **1998**, *120*, 8557.
(157) Wong, S. S.; Harper, J. D.; Lansbury, P. T.; Lieber, C. M. *Journal of the American Chemical Society* **1998**, *120*, 603.
(158) Hutchison, D. N.; Morrill, N. B.; Aten, Q.; Turner, B. W.; Jensen, B. D.; Howell, L. L.; Vanfleet, R. R.; Davis, R. C. *Journal of Microelectromechanical Systems*, *19*, 75.
(159) Ajayan, P. M.; Stephan, O.; Colliex, C.; Trauth, D. *Science* **1994**, *265*, 1212.
(160) Schadler, L. S.; Giannaris, S. C.; Ajayan, P. M. *Applied Physics Letters* **1998**, *73*, 3842.
(161) Lai, K. W. C.; Xi, N.; Fung, C. K. M.; Chen, H. Z.; Tarn, T. J. *Applied Physics Letters* **2009**, *95*.
(162) Dragoman, M.; Dragoman, D. *Progress in Quantum Electronics* **2009**, *33*, 165.
(163) Burghard, M.; Klauk, H.; Kern, K. *Advanced Materials* **2009**, *21*, 2586.
(164) Lu, W.; Lieber, C. M. *Nature Materials* **2007**, *6*, 841.
(165) Baughman, R. H.; Zakhidov, A. A.; de Heer, W. A. *Science* **2002**, *297*, 787.
(166) Dekker, C. *Physics Today* **1999**, *52*, 22.
(167) Saito, R.; Fujita, M.; Dresselhaus, G.; Dresselhaus, M. S. *Applied Physics Letters* **1992**, *60*, 2204.
(168) Rosenblatt, S.; Yaish, Y.; Park, J.; Gore, J.; Sazonova, V.; McEuen, P. L. *Nano Letters* **2002**, *2*, 869.
(169) Kukovecz, A.; Kramberger, C.; Georgakilas, V.; Prato, M.; Kuzmany, H. *European Physical Journal B* **2002**, *28*, 223.
(170) Jorio, A.; Saito, R.; Dresselhaus, G.; Dresselhaus, M. S. *Philosophical Transactions of the Royal Society a-Mathematical Physical and Engineering Sciences* **2004**, *362*, 2311.

(171) Dai, H. J. *Surface Science* **2002**, *500*, 218.
(172) Dumitrescu, I.; Unwin, P. R.; Macpherson, J. V. *Chemical Communications* **2009**, *45*, 6886.
(173) Chen, J.; Rao, A. M.; Lyuksyutov, S.; Itkis, M. E.; Hamon, M. A.; Hu, H.; Cohn, R. W.; Eklund, P. C.; Colbert, D. T.; Smalley, R. E.; Haddon, R. C. *Journal of Physical Chemistry B* **2001**, *105*, 2525.
(174) Liu, C. Y.; Bard, A. J.; Wudl, F.; Weitz, I.; Heath, J. R. *Electrochemical and Solid State Letters* **1999**, *2*, 577.
(175) Iijima, S. *Nature* **1991**, *354*, 56.
(176) Sun, X.; Bao, W. R.; Lv, Y. K.; Deng, J. Q.; Wang, X. Y. *Materials Letters* **2007**, *61*, 3956.
(177) Bethune, D. S.; Kiang, C. H.; Devries, M. S.; Gorman, G.; Savoy, R.; Vazquez, J.; Beyers, R. *Nature* **1993**, *363*, 605.
(178) Dai, H. *Acc. Chem. Res.* **2002**, *35*, 1035.
(179) Joseyacaman, M.; Mikiyoshida, M.; Rendon, L.; Santiesteban, J. G. *Applied Physics Letters* **1993**, *62*, 657.
(180) Endo, M.; Takeuchi, K.; Igarashi, S.; Kobori, K.; Shiraishi, M.; Kroto, H. W. *Journal of Physics and Chemistry of Solids* **1993**, *54*, 1841.
(181) Kingston, C. T.; Simard, B. *Analytical Letters* **2003**, *36*, 3119.
(182) Guo, T.; Nikolaev, P.; Rinzler, A. G.; Tomanek, D.; Colbert, D. T.; Smalley, R. E. *Journal of Physical Chemistry* **1995**, *99*, 10694.
(183) Hafner, J. H.; Bronikowski, M. J.; Azamian, B. R.; Nikolaev, P.; Rinzler, A. G.; Colbert, D. T.; Smith, K. A.; Smalley, R. E. *Chemical Physics Letters* **1998**, *296*, 195.
(184) Nikolaev, P.; Bronikowski, M. J.; Bradley, R. K.; Rohmund, F.; Colbert, D. T.; Smith, K. A.; Smalley, R. E. *Chemical Physics Letters* **1999**, *313*, 91.
(185) Kratschmer, W.; Lamb, L. D.; Fostiropoulos, K.; Huffman, D. R. *Nature* **1990**, *347*, 354.
(186) Seraphin, S.; Zhou, D. *Applied Physics Letters* **1994**, *64*, 2087.
(187) Zhou, D.; Seraphin, S.; Wang, S. *Applied Physics Letters* **1994**, *65*, 1593.
(188) Hiura, H.; Ebbesen, T. W.; Tanigaki, K. *Advanced Materials* **1995**, *7*, 275.
(189) Guo, T.; Nikolaev, P.; Thess, A.; Colbert, D. T.; Smalley, R. E. *Chemical Physics Letters* **1995**, *243*, 49.
(190) Chiang, I. W.; Brinson, B. E.; Huang, A. Y.; Willis, P. A.; Bronikowski, M. J.; Margrave, J. L.; Smalley, R. E.; Hauge, R. H. *Journal of Physical Chemistry B* **2001**, *105*, 8297.
(191) Britto, P. J.; Santhanam, K. S. V.; Ajayan, P. M. *Bioelectrochemistry and Bioenergetics* **1996**, *41*, 121.
(192) Nugent, J. M.; Santhanam, K. S. V.; Rubio, A.; Ajayan, P. M. *Nano Letters* **2001**, *1*, 87.
(193) Ivanov, V.; Nagy, J. B.; Lambin, P.; Lucas, A.; Zhang, X. B.; Zhang, X. F.; Bernaerts, D.; Vantendeloo, G.; Amelinckx, S.; Vanlanduyt, J. *Chemical Physics Letters* **1994**, *223*, 329.
(194) Dai, H. J.; Rinzler, A. G.; Nikolaev, P.; Thess, A.; Colbert, D. T.; Smalley, R. E. *Chemical Physics Letters* **1996**, *260*, 471.
(195) Day, T. M.; Unwin, P. R.; Wilson, N. R.; Macpherson, J. V. *Journal of the American Chemical Society* **2005**, *127*, 10639.
(196) Bertoncello, P.; Edgeworth, J. P.; Macpherson, J. V.; Unwin, P. R. *Journal of the American Chemical Society* **2007**, *129*, 10982.
(197) Edgeworth, J. P.; Wilson, N. R.; Macpherson, J. V. *Small* **2007**, *3*, 860.

(198) Dumitrescu, I.; Edgeworth, J. P.; Unwin, P. R.; Macpherson, J. V. *Advanced Materials* **2009**, *21*, 3105.
(199) Fan, Y. W.; Goldsmith, B. R.; Collins, P. G. *Nature Materials* **2005**, *4*, 906.
(200) Liu, J.; Rinzler, A. G.; Dai, H. J.; Hafner, J. H.; Bradley, R. K.; Boul, P. J.; Lu, A.; Iverson, T.; Shelimov, K.; Huffman, C. B.; Rodriguez-Macias, F.; Shon, Y. S.; Lee, T. R.; Colbert, D. T.; Smalley, R. E. *Science* **1998**, *280*, 1253.
(201) Dillon, A. C.; Gennett, T.; Jones, K. M.; Alleman, J. L.; Parilla, P. A.; Heben, M. J. *Advanced Materials* **1999**, *11*, 1354.
(202) Dujardin, E.; Ebbesen, T. W.; Krishnan, A.; Treacy, M. M. J. *Advanced Materials* **1998**, *10*, 611.
(203) Moon, J. M.; An, K. H.; Lee, Y. H.; Park, Y. S.; Bae, D. J.; Park, G. S. *Journal of Physical Chemistry B* **2001**, *105*, 5677.
(204) Pumera, M. *Langmuir* **2007**, *23*, 6453.
(205) Jurkschat, K.; Ji, X. B.; Crossley, A.; Compton, R. G.; Banks, C. E. *Analyst* **2007**, *132*, 21.
(206) Lawrence, N. S.; Deo, R. P.; Wang, J. *Electroanalysis* **2005**, *17*, 65.
(207) Dumitrescu, I.; Wilson, N. R.; Macpherson, J. V. *The Journal of Physical Chemistry C* **2007**, *111*, 12944.
(208) Kuznetsova, A.; Popova, I.; Yates, J. T.; Bronikowski, M. J.; Huffman, C. B.; Liu, J.; Smalley, R. E.; Hwu, H. H.; Chen, J. G. G. *Journal of the American Chemical Society* **2001**, *123*, 10699.
(209) Mawhinney, D. B.; Naumenko, V.; Kuznetsova, A.; Yates, J. T.; Liu, J.; Smalley, R. E. *Journal of the American Chemical Society* **2000**, *122*, 2383.
(210) Mawhinney, D. B.; Naumenko, V.; Kuznetsova, A.; Yates, J. T.; Liu, J.; Smalley, R. E. *Chemical Physics Letters* **2000**, *324*, 213.
(211) Zhao, J. J.; Park, H. K.; Han, J.; Lu, J. P. *Journal of Physical Chemistry B* **2004**, *108*, 4227.
(212) Choi, H. J.; Ihm, J.; Louie, S. G.; Cohen, M. L. *Physical Review Letters* **2000**, *84*, 2917.
(213) Lu, K. L.; Lago, R. M.; Chen, Y. K.; Green, M. L. H.; Harris, P. J. F.; Tsang, S. C. *Carbon* **1996**, *34*, 814.
(214) Duesberg, G. S.; Burghard, M.; Muster, J.; Philipp, G.; Roth, S. *Chemical Communications* **1998**, 435.
(215) Bandow, S.; Rao, A. M.; Williams, K. A.; Thess, A.; Smalley, R. E.; Eklund, P. C. *The Journal of Physical Chemistry B* **1997**, *101*, 8839.
(216) Arai, S.; Saito, T.; Endo, M. *Journal of the Electrochemical Society*, *157*, D147.
(217) Zhang, H. M.; Wang, X. B.; Wan, L. J.; Liu, Y. Q.; Bai, C. L. *Electrochimica Acta* **2004**, *49*, 715.
(218) Luo, H. X.; Shi, Z. J.; Li, N. Q.; Gu, Z. N.; Zhuang, Q. K. *Analytical Chemistry* **2001**, *73*, 915.
(219) Dai, Y. Q.; Shiu, K. K. *Electroanalysis* **2004**, *16*, 1697.
(220) Moore, R. R.; Banks, C. E.; Compton, R. G. *Analytical Chemistry* **2004**, *76*, 2677.
(221) Rubianes, M. D.; Rivas, G. A. *Electrochemistry Communications* **2003**, *5*, 689.
(222) Kang, S. J.; Kocabas, C.; Ozel, T.; Shim, M.; Pimparkar, N.; Alam, M. A.; Rotkin, S. V.; Rogers, J. A. *Nature Nanotechnology* **2007**, *2*, 230.
(223) Rutkowska, A.; Walker, D.; Gorfman, S.; Thomas, P. A.; Macpherson, J. V. *The Journal of Physical Chemistry C* **2009**, *113*, 17087.

(224) Dumitrescu, I.; Unwin, P. R.; Wilson, N. R.; Macpherson, J. V. *Analytical Chemistry* **2008**, *80*, 3598.
(225) Huebner, K. H.; Dewhirst, D. L.; Smith, D. E.; Byrom, T. G. *The Finite Element Method for Engineers*, 4 ed.; John Wiley & Sons, Inc.: New York, 2001.
(226) Zimmerman, W. B. J. *Process Modelling and Simulation with Finite Element Methods*; World Scientific: London, 2005.
(227) Bianchi, F.; Ferrigno, A.; Girault, H. H. *Analytical Chemistry* **2000**, *72*, 1987.
(228) Schnippering, M.; Unwin, P. R.; Hult, J.; Laurila, T.; Kaminski, C. F.; Langridge, J. M.; Jones, R. L.; Mazurenka, M.; Mackenzie, S. R. *Electrochemistry Communications* **2008**, *10*, 1827.
(229) Macpherson, J. V.; Unwin, P. R. *Journal of Physical Chemistry* **1995**, *99*, 14824.
(230) Macpherson, J. V.; Unwin, P. R. *Journal of Physical Chemistry* **1994**, *98*, 11764.
(231) Bard, A. J.; Mirkin, M. V.; Unwin, P. R.; Wipf, D. O. *Journal of Physical Chemistry* **1992**, *96*, 1861.
(232) Kwak, J.; Bard, A. J. *Analytical Chemistry* **1989**, *61*, 1221.
(233) Wipf, D. O.; Bard, A. J. *Journal of the Electrochemical Society* **1991**, *138*, 469.
(234) Holder, M. N.; Gardner, C. E.; Macpherson, J. V.; Unwin, P. R. *Journal of Electroanalytical Chemistry* **2005**, *585*, 8.
(235) Henley, I. E.; Fisher, A. C.; Compton, R. G.; Banks, C. E. *Journal of Physical Chemistry B* **2005**, *109*, 7843.
(236) Amatore, C.; Sella, C.; Thouin, L. *Journal of Physical Chemistry B* **2002**, *106*, 11565.
(237) Amatore, C.; Da Mota, N.; Lemmer, C.; Pebay, C.; Sella, C.; Thouin, L. *Analytical Chemistry* **2008**, *80*, 9483.
(238) Norton, J. D.; Benson, W. E.; White, H. S.; Pendley, B. D.; Abruna, H. D. *Analytical Chemistry* **1991**, *63*, 1909.
(239) Grime, J. M. A.; Edwards, M. A.; Rudd, N. C.; Unwin, P. R. *Proceedings of the National Academy of Sciences of the United States of America* **2008**, *105*, 14277.
(240) Qiu, F. L.; Fisher, A. C.; Henley, I. E.; Dryfe, R. A. W. *Electrochemistry Communications* **2003**, *5*, 169.
(241) Harvey, S. L. R.; Parker, K. H.; O'Hare, D. *Journal of Electroanalytical Chemistry* **2007**, *610*, 122.
(242) Bitziou, E.; Rudd, N. C.; Edwards, M. A.; Unwin, P. R. *Analytical Chemistry* **2006**, *78*, 1435.
(243) Mandin, P.; Pauporte, T.; Fanouillere, P.; Lincot, D. *Journal of Electroanalytical Chemistry* **2004**, *565*, 159.
(244) Remita, E.; Tribollet, B.; Sutter, E.; Vivier, V.; Ropital, F.; Kittel, J. *Corrosion Science* **2008**, *50*, 1433.

2. Experimental

This chapter describes the experimental techniques which are used throughout this thesis, including details of the synthesis and characterisation of 2D SWNT random networks used as a WE material and the MSL fabrication procedure. Additionally, a complete list of all materials employed throughout this thesis is summarised at the end of the chapter.

2.1. SWNT Electrode Fabrication

This section describes the synthesis of high density (HD) and very high density (VHD) 2D SWNT networks using cCVD. The HD SWNT networks used typically have a density of 3-4 μm SWNT length per μm^2 of substrate (<1 % SWNT surface coverage), the density of VHD samples used within this thesis is greater than 6 μm length of SWNT per μm^2 of substrate (~1 % SWNT surface coverage). For all studies the substrate used was insulating silicon oxide. Initially the silicon oxide substrate is cut to the required dimensions, cleaned, and then the catalyst is deposited. The synthesis of SWNT networks is performed using cCVD and the resulting substrate characterised by the techniques outlined in section 2.2. Figure 2.1 outlines the steps required to create an electrode from an as grown SWNT network, all steps will be explained in detail in the relevant sections.

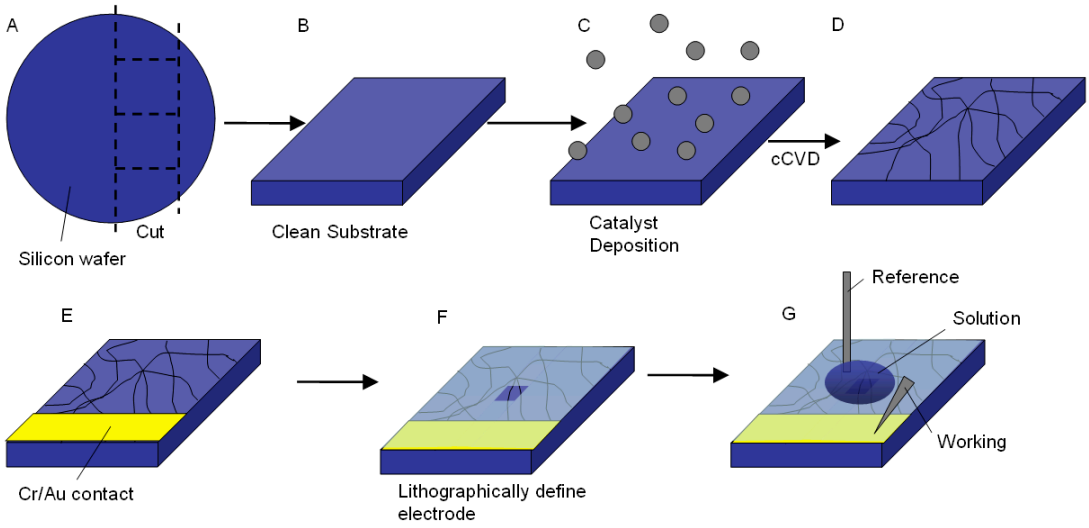

Figure 2.1 A schematic outlining the key steps in preparing an SWNT network as an electrode for electroanalysis, (a) cleaving samples from the wafer, (b) cleaning the sample, (c) catalyst deposition, (d) synthesis of SWNTs, (e) creating electrical contacts, (f) defining the electrode dimensions by photolithography, and (g) electrochemical set up employing the SWNT electrode.

2.1.1. Substrate Preparation

All SWNT networks used within this thesis were synthesised on a silicon wafer with a thermally oxidised layer of ~300 nm thick silicon oxide. Wafers were obtained as 4" diameter discs and cut to the required size. Substrate samples of ~1 cm x ~1 cm were cut by scratching the polished side of the wafer with a diamond tipped scribe followed by the application of a small force over the scratch on the non-polished side of the wafer. Samples were cleaned by rinsing thoroughly with acetone and isopropyl alcohol followed by being blown dry with nitrogen. The substrate preparation was identical for both HD and VHD samples.

2.1.2. Synthesis of high density networks

HD samples were synthesised using an iron catalyst with methane as the carbon feed source. The iron catalyst was delivered to the substrate surface using ferritin. Ferritin is a bio-molecule which consists of an outer protein shell of ~12 nm in diameter with a central core containing up to 4500 oxidised iron atoms, ~8 nm in diameter.[1] The ferritin was prepared by diluting 1 volume ferritin to 200 volumes of water, the total volume used was dependent upon the number of samples to be processed. The ferritin solution was sonicated for 5 minutes immediately before use. The silicon samples were submerged for 1 hour in the ferritin solution, before being gently rinsed with water and blown dry under a low flow rate of nitrogen. The samples were exposed to an oxygen plasma (Emitech, K1050X) at 100 W plasma power, 1 x 10^{-6} bar plasma pressure, for 1 minute to remove the ferritin protein shells.

Samples were placed within the centre of the cCVD furnace, which consisted of a split tube oven (Lindberg/Blue M, Thermo/Fisher Scientific), a quartz tube (25 mm outer diameter, 1.5 mm wall thickness, 50 cm length, fused quartz, Enterprise Q Ltd., U.K.) connected to a programmable heat controller. The furnace was connected to mass flow controllers (MFCs, model 1179A, MKS Instruments UK Ltd., U.K.), which were controlled using an appropriate analogue readout unit (Type 247, MKS Instruments UK Ltd., U.K.), as shown in figure 2.1.

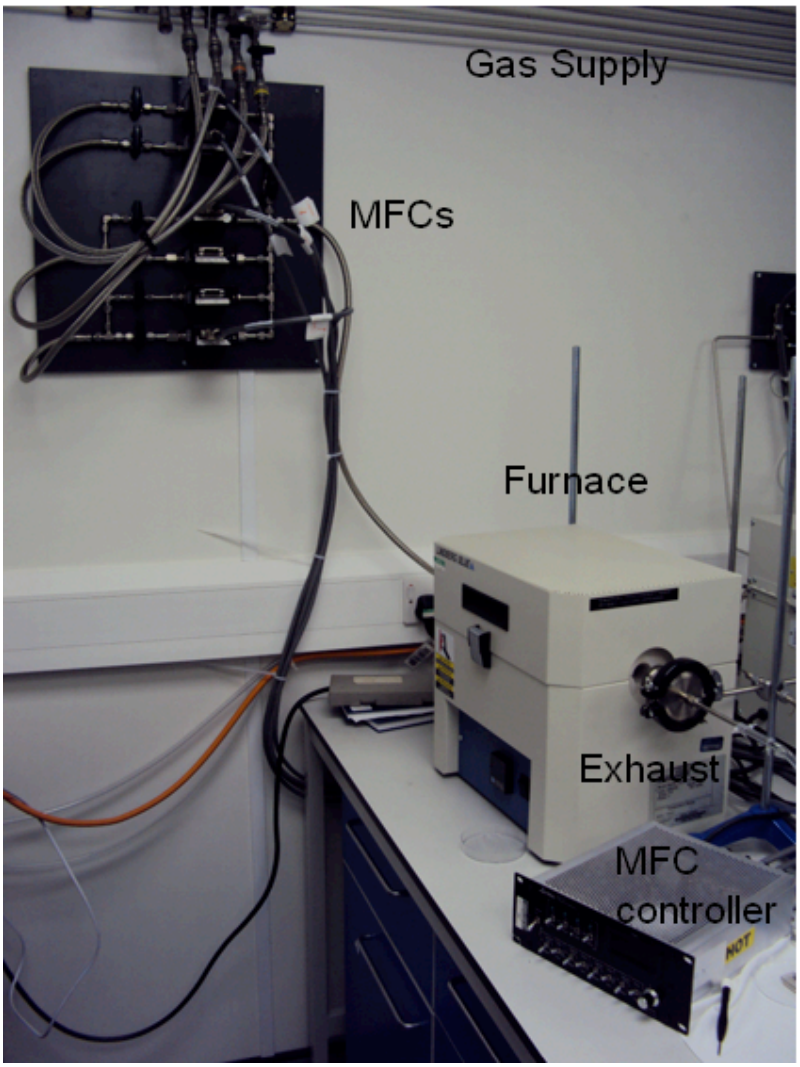

Figure 2.2 Photograph of the HD cCVD system

Samples were heated to 875 °C under a flow of 200 sccm H_2. Once the temperature had stabilised a methane flow of 1800 sccm was supplied for 5 minutes. After growth the samples were cooled under a flow of H_2, the lid was opened at 700 °C to speed cooling. Samples were removed from the oven once the temperature was below 200 °C.[2]

2.1.3. Synthesis of very high density networks

The VHD networks were synthesised using a cobalt catalyst with ethanol vaporised in argon as the carbon feedstock. The cobalt catalyst was sputtered onto the silicon oxide samples using a desktop sputter deposition system (SC7640 sputter coater, Quorum Technologies Ltd., U.K.) and a target made from high purity cobalt film (Neubauer Chemikalien, Agar Scientific Ltd., U.K.) adhered to an aluminium support. Prior to deposition the entire chamber was wiped clean with isopropyl alcohol and the chamber was repeatedly purged with argon. To remove any impurities from the cobalt target a burn in cycle was performed at 1.5 kV. Deposition of the cobalt catalyst particles was performed at 1 kV under an argon pressure of ~4 x 10^{-2} bar, adjusted to provide a constant current of 10 mA for 10 s.

The samples were placed in the centre of a cCVD furnace and heated to 850 °C under a constant flow of 150 sccm H_2. Once the temperature was stable argon, bubbled through an ethanol bath, held at 0 °C, was passed through the cCVD furnace for 10 minutes.[3] After the growth period the samples were cooled under H_2 before being removed when the temperature was less than 200 °C. As for the synthesis of HD networks the furnace lid was opened at 700 °C to speed the cooling of the samples. The VHD cCVD system is shown in figure 2.3.

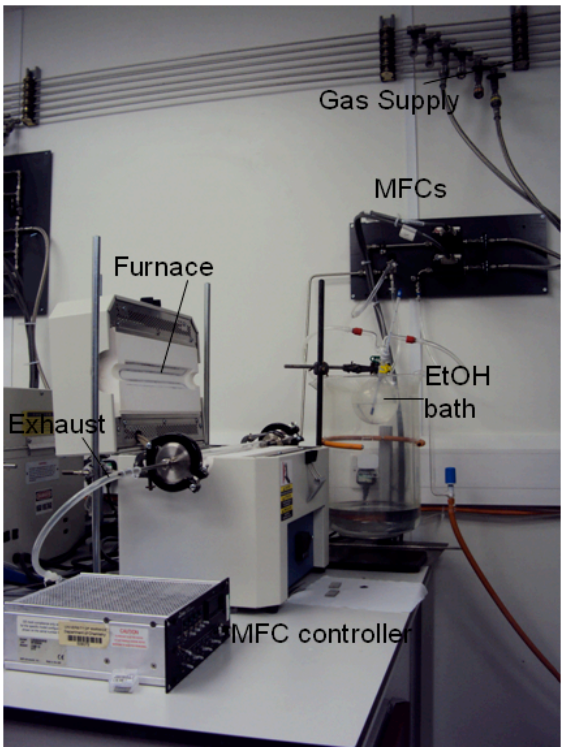

Figure 2.3 Photograph of the VHD cCVD system.

2.2. Characterisation of SWNT networks

To determine the suitability of growth conditions and quality of individual samples a range of surface analysis techniques were employed within this work.

2.2.1. Atomic Force Microscopy

AFM was employed extensively to investigate the diameter of SWNTs and the network density. This technique is non-invasive and provides information on the cleanliness of the sample, the size of residual catalyst particles and whether SWNT or MWNT are present. However it is important to realise that this technique is time consuming and is limited to small area scans, within this thesis typical scans are between 1 μm x 1 μm to 5 μm x 5 μm.

Images were taken using a Veeco MultiMode™ AFM, equipped with either a NanoScope™ IIIa controller or a NanoScope™ V controller. A 'J' series piezo scanner, allowed a maximum scan range of 150 μm × 150 μm in the lateral direction, and ± 2.5 μm in the vertical direction. A vibration isolation table (Micro-g, Technical Manufacturing Corporation, U.S.A.) with microscope stand (in house) was used to reduce noise and to allow lateral tip positioning. All images reported in this thesis were taken in TappingMode™ (TM) to minimise the lateral forces exerted upon the sample. TM involves the driven oscillation of the cantilever near the resonance frequency. The tip is lowered to the surface and an "amplitude set point" is specified by the user, this controls how hard the tip contacts the surface, and requires a balance to be achieved which accurately maps the surface topography without damaging a soft sample. The tip is raster scanned across the surface whilst varying the height of the cantilever to maintain the amplitude of the oscillation. The variations in the height of the cantilever are recorded with respect to the scan position to create a topographic map of the surface.

For all samples used in electrochemical experiments the CNT diameter, density and cleanliness of samples were obtained from a series of AFM images. The CNT diameters were taken from the height of the scan, as tip convolution distorts the lateral dimensions of the CNTs. A visual inspection of the scan was used to determine if there was an excess of catalyst particles or amorphous carbon present nearby and upon the CNTs. The density of the samples was calculated by measuring the length of CNTs present on the scan and dividing by the area of the scan, reported as $\mu m\ \mu m^{-2}$ (length of SWNT per area of substrate). AFM was used as the method of characterisation once a stable growth procedure had been established.

A typical AFM image of a HD SWNT sample is shown in figure 2.4 (a). The image shows a low density of unreacted Fe catalyst particles and the resulting SWNT network at a density of ~4 μm μm^{-2}. The SWNT height is between 0.8 nm to 3 nm and typically one Fe nanoparticles nucleates one SWNT, with the Fe nanoparticles likely to be coated in carbon to form iron carbide.[4] The presence of tubes of larger height is attributed to bundles of SWNT or small MWNTs. Figure 2.4 (b) shows a typical VHD SWNT network. Here a higher density of unreacted Co catalyst particles can be seen for the HD sample, however the density of grown SWNTs is much higher. CVs performed in only supporting electrolyte using UMEs of the VHD networks do not display Co stripping peaks[3]. Hence we believe that the reacted Co particles are encapsulated at the end of a SWNT, with the majority of unreacted Co nanoparticles not being electrically connected to the network. Those that are connected are either in a significantly low quantity not to contribute to the background current response or exist as cobalt carbide which does not undergo an electrochemical redox reaction within the solvent window.

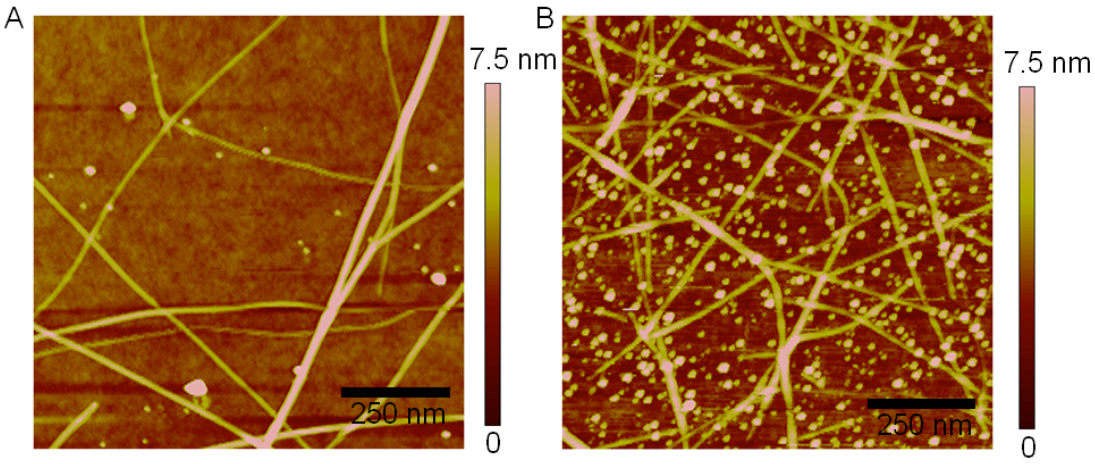

Figure 2.4 AFM images of a HD SWNT network (a) and a VHD SWNT network (b)

2.2.2. Field Emission Scanning Electron Microscopy

Field emission scanning electron microscopy (FE-SEM) was used to determine the density and how uniform the growth of a CNT network was over a sample. The contrast in the FE-SEM images shown is due to the potential difference caused by charging of the conducting network upon the insulating silicon oxide layer.[2] This causes CNTs connected to the network to have a higher contrast from the silicon oxide layer than isolated CNTs. FE-SEM allows for large areas of the sample to be assessed quickly for network density; however the data obtained is limited as it does not allow for the assessment of CNT diameters, or the presence of amorphous carbon and catalyst particles. As such FE-SEM images were used to ensure that the synthesis protocols described in section 2.1 produced uniform networks across the entire sample.

All FE-SEM images were obtained using an ultra-high resolution FE-SEM instrument (Zeiss Supra 55VP), under an acceleration voltage of 1 kV. Samples were fixed to a holder using 54 carbon adhesive pads (G3347N, Agar Scientific Ltd., U.K.).

2.2.3. Raman Spectroscopy

CNT samples were checked for the presence of amorphous carbon using Raman spectroscopy and importantly to confirm the presence of SWNTs. The Raman active modes of SWNTs of importance are the D and G peaks present at ~1300 cm^{-1} and ~1600 cm^{-1} respectively and the radial breathing modes which occur between 100 cm^{-1} to 300 cm^{-1}.[5] The D peak represents disorder within the graphitic lattice of the CNTs, relating to either defects or amorphous carbon in the sample, and the G peak signifies the sp^2 lattice.[5, 6] Only SWNT networks with a negligible D peak (less than

5% of the G peak height) were used for electrochemical experiments throughout this thesis. The radial breathing mode can be used to determine the diameter of a SWNT, however as the samples used consist of randomly grown SWNTs with many SWNTs exposed to the laser spot the SWNT dimensions were not derived from this information.

Micro-Raman spectra of SWNT networks were recorded using a Renishaw inVia Raman microscope with incorporated Leica microscope and CCD detector. SWNT peaks were calibrated against a Si peak at 521 cm^{-1}. An Ar laser with an excitation wavelength of 514.5 nm (2.41 eV), at 10 mW power was focused in a ~ 2.5 μm spot for all experiments. Figure 2.5 shows typical Raman spectra for both HD and VHD networks. Due to the lower density of CNTs in the HD sample, the peaks are weaker than for the VHD samples. Note that the size of the D peak relative to the G peak is small for both cases indicating high quality and clean SWNT networks.

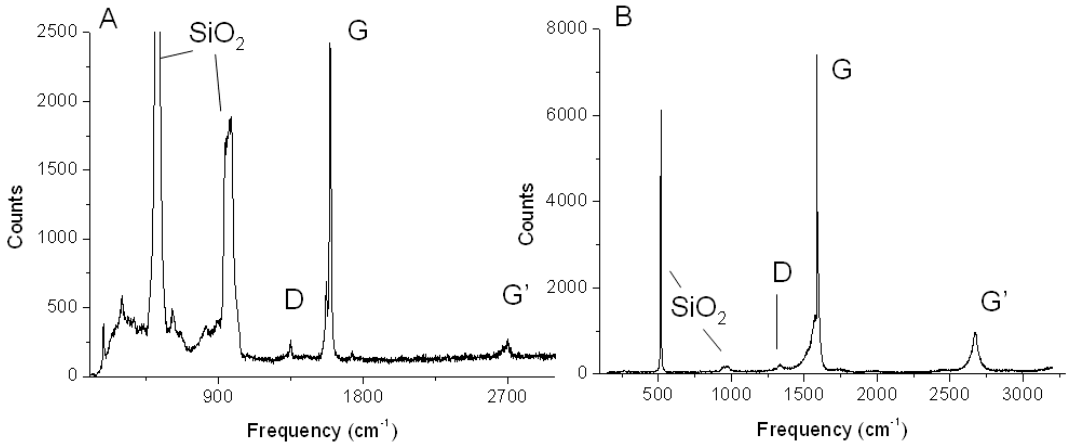

Figure 2.5 Raman spectra of a HD SWNT network (a) and a VHD network (b).

2.3. Working Electrode Fabrication

The methodologies employed to synthesise and define all planar metal electrodes used within the chapters 4 and 6 and SWNT network electrodes follow the same procedures described within this section.

2.3.1. Metal Deposition

Au working electrodes and ohmic electrical contacts to a SWNT network were made by thermal evaporation of a chromium adhesion layer followed by a thicker gold layer. Evaporation was performed using a custom made evaporation/sputter coater unit (Moorfield Associates, U.K.) where the required metal was heated by applying a current to the metal source. The chromium adhesion layer, ~10 nm thick, was deposited from a chromium bar by applying a current of ~90 A. The gold layer was evaporated off an aluminium boat at ~50 A. For the all metal electrodes a Au layer of 200-300 nm was used, for the SWNT networks a Au layer of ~100 nm was employed. Deposition was monitored via a quartz crystal microbalance located near the samples, and the area of deposition was defined by shadow mask.

2.3.2. Photolithography

Photolithography was used to define the dimensions of the WE by optically patterning a photoresist film on the sample. The geometry of the electrode area was dependant upon the application *e.g.* band electrode for channel flow, and the masks

employed are described in more detail in chapters 5 and 6. Samples were cleaned by gently passing nitrogen over the surface before spin coating a primer layer followed by a layer of S1818 positive photo resist. Spin coating was performed at 3000 rpm for 45 seconds (G3-8, Specialty Coating Systems Inc., U.S.A.). Samples were heated in air at 115 °C for 1 minute. The defined electrode dimensions were created by positioning the samples under a custom made photo resist mask (J.D. Photo Tools, UK), exposing to UV light (mask aligner), and developing the photo resist film in MF-319 solution.

2.4. Microstereo Lithography

MSL was used to construct both the channel flow units and the WJE units, the designs for both of these parts will be discussed in more detail in the relevant sections. The procedure is summarised in figure 2.6. Initially the device was designed using the 3D design package Solid Works (Dassault Systémes, France), before being sent to the MSL machine (Envisiontec PerFactory Mini Multi-Lens, Germany), which employed a dynamic masking system. The process involved forming an initial 25 μm thick polymer layer by lowering the build platform into a tray containing a 3 mm deep reservoir of photoactive resin (R11, Envisiontec). The resin consists of an acrylic oligomer, dipentaerythritol entaacrylate, propoxylated trimethylolpropane triacrylate, photoinitiator and stabilizers. Each X-Y slice of the CAD model was recreated in a masked output by the MSL machine projector, focussed onto the plane of the trapped resin layer. Once cured, the resin tray tilts, “peeling” the new layer from the tray and leaving it attached to the build platform. Subsequent layers (also 25 μm thick) were built up by repeating these steps, with layers after the initial slice being attached to the previously fabricated layer, rather than directly to the build platform.

Once complete, the product was removed from the base plate, cleaned with isopropyl alcohol, then acetone and finally rinsed thoroughly with distilled water. A final high intensity UV-light cure for approximately 30 minutes ensured completion of the polymerisation process.[7] The whole process took 6-8 hours to complete, with four units produced during one build. The height of each channel was measured independently using interferometery (WYKO NT-2000 Surface Profiler, WYKO Systems).

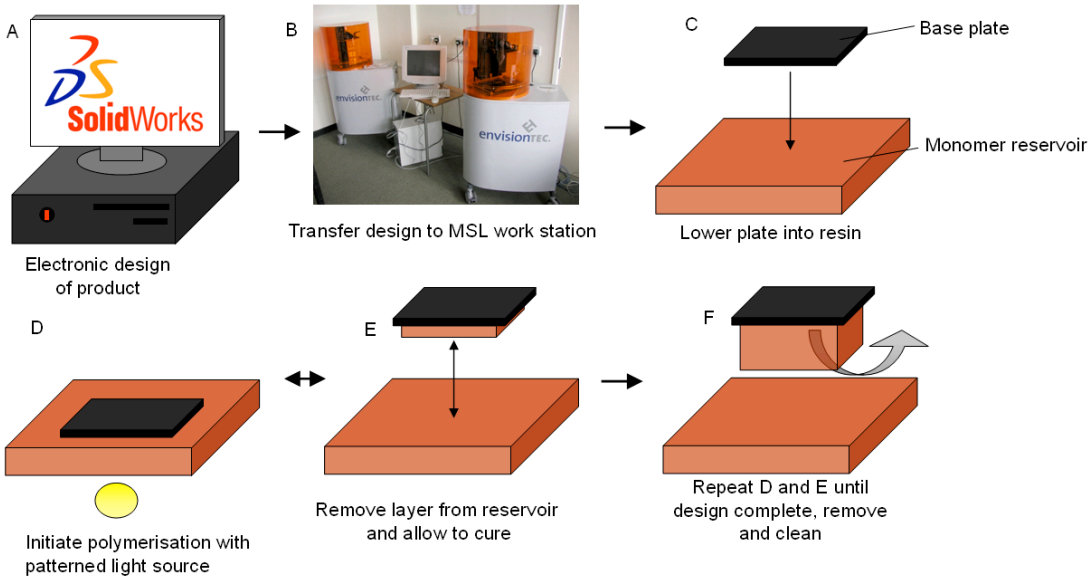

Figure 2.6 Schematic outlining the important steps in the MSL production of a device. (a) The product is designed using a computer modelling package, (b) the design is converted and sent to the MSL work station, (c) the base plate is lowered into the resin, (d) a patterned light source initiates the polymerisation, (e) the layer is removed from the resin and allowed to cure, (f) steps (d) and (e) are repeated to complete the product, followed by removal and final curing of the product.

2.5. Electrochemistry

This section covers common features of typical LSV, CV and CA measurements which are performed upon a variety of electrodes throughout this thesis. Specific details of each setup will be described in the relevant sections.

When working with low currents (~1 μA or lower) a two electrode setup was employed. This typically involved the use of a chlorinated silver wire quasi-reference electrode and WE within solution. When currents were greater than 1 μA, a three electrode setup was employed. This involved a reference electrode, counter electrode (platinum wire) and a WE. Two different reference electrodes were employed for the two and three electrode experiments, a chlorinated silver wire, and a fritted saturated calomel electrode. For both setups an electrical connection to the WE was created by touching the gold band (or exposed gold for an entirely gold electrode) with a needle tipped micropositioner (Qatar Research).

Experiments were carried out on either a CH Instruments 600B potentiostat, or 760C bipotentiostat. Several experiments within chapter 4 were performed using an Autolab electrochemical workstation (Eco Chemie).

2.6. Chemicals and Materials

The chemicals and materials used throughout this thesis are summarised in table 1.

Material	Supplier
SWNT synthesis	
Substrate	
Oxidised silicon wafer	4" diameter, 525 μm thick, <100>, 1 – 10 Ω cm resistivity, n-type, single-side polished, 300 nm thermally grown oxide, IDB Technologies Ltd., U.K.
Gases	
H_2	99.95%, high purity, BOC Gases, U.K.
Ar	99.9995%, BOC Gases, U.K.
CH_4	99.995%, BOC Gases, U.K.
Catalysts	
Ferritin, from horse spleen	50 – 150 mg mL^{-1} in 150 mM aqueous NaCl, Sigma-Aldrich Co., U.K.
Cobalt Foil	0.5 mm, 99.95%, Testbourne Ltd., U.K.
Metal Deposition	
Chromium bar	Cr coating on tungsten rod, 99.9%
Gold	99.99%, Goodfellow Cambridge Ltd., U.K.
Solvents	
Acetone	99%, Fisher Scientific Ltd., U.K.
Isopropyl Alcohol	99.99%, Fisher Scientific Ltd., U.K.
Ethanol	99.99%, Fisher Scientific Ltd., U.K.
Photo Resists and Developers	
Primer	Primer Rohm and Haas Ltd., U.K
S1818	MicroChem Corp., U.S.A.
MF-319	Shipley Europe Ltd., U.K.
Chemicals	
Ferrocenylmethyltrimethylammonium hexafluorophosphate, $FcTMA^+PF_6^-$	Prepared from $FcTMA^+I^-$ via metathesis with $Ag^+PF_6^-$
Sodium chloride, NaCl	99.999%, Sigma-Aldrich Co., U.K.
99% Potassium nitrate, KNO_3	Fisher Scientific Ltd., U.K.
99.999% Potassium nitrate, KNO_3	Fisher Scientific Ltd., U.K.
Dopamine hydrochloride	Sigma-Aldrich Co., U.K.
0.1 M Phosphate buffered saline solution (PBS)	81 mM Na_2HPO_4, 19 mM NaH_2PO_4
Na_2HPO_4	Sigma-Aldrich Co., U.K.
NaH_2PO_4	Sigma-Aldrich Co., U.K.
Water	≥18 MΩ resistivity, purified with a Milli-Q™ unit, Millipore Corp., U.S.A.

Table 1 List of all the materials used for the work described within this thesis

2.7. References

(1) Clegg, G. A.; Fitton, J. E.; Harrison, P. M.; Treffry, A. *Progress in Biophysics & Molecular Biology* **1980**, *36*, 53.

(2) Edgeworth, J. P.; Wilson, N. R.; Macpherson, J. V. *Small* **2007**, *3*, 860.

(3) Dumitrescu, I.; Edgeworth, J. P.; Unwin, P. R.; Macpherson, J. V. *Advanced Materials* **2009**, *21*, 3105.

(4) Colomer, J. F.; Stephan, C.; Lefrant, S.; Van Tendeloo, G.; Willems, I.; Konya, Z.; Fonseca, A.; Laurent, C.; Nagy, J. B. *Chemical Physics Letters* **2000**, *317*, 83.

(5) Jorio, A.; Saito, R.; Dresselhaus, G.; Dresselhaus, M. S. *Philosophical Transactions of the Royal Society a-Mathematical Physical and Engineering Sciences* **2004**, *362*, 2311.

(6) Matthews, M. J.; Pimenta, M. A.; Dresselhaus, G.; Dresselhaus, M. S.; Endo, M. *Physical Review B* **1999**, *59*, R6585.

(7) Stefany Jacesko; Jose K Abraham; Taeksoo Ji; Vijay K Varadan; Cole, M.; Gardner, J. W. *SMART MATERIALS AND STRUCTURES* **2005**, 1010–1016.

3. Electrochemical Activity of Single Walled Carbon Nanotubes

3.1. Aim

As discussed in section 3.2, two opposing views currently exist for the sites where electron transfer occurs at a CNT. We perform further studies in this area by combining both theoretical and experimental studies in order to elucidate the potential sites of electron transfer (ET) at a SWNT. The methodology employed by Edwards *et al.*[1] for slowing solution diffusion of a species using a Nafion™ film, is adapted for application to HD SWNT networks. This allows diffusion profiles, on short length scales (<50 nm), to be observed electrochemically, within the timescale of the electrochemical experiment. The experimentally observed data is compared to FEM simulations which have been formulated for the two theories for the sites of electron transfer at a SWNT.

3.2. Active sites on CNTs

The electrochemical activity of carbon electrode materials has been debated for several decades.[1-5] Due to the wide use of carbon electrodes in electrochemical analysis[6-9] fundamental understanding of the activity is of particular interest.[4, 10, 11] ET at CNTs has been investigated by a range of electrochemical studies with different claims attributing the electrochemical activity to the sidewall[12], defect sites,[3] or metallic catalyst particles used in synthesis.[13, 14] In general there appears to be two

opposing theories for where ET occurs on a CNT; (i) ET occurs only at discrete sites, or (ii) across the entire sidewall.

3.2.1. Discrete site activity

As discussed above it has been proposed that a CNT is an "electrochemically inert stick decorated with electrochemically active sites."[15] Initial reports drew an analogy between MWNTs and HOPG, considering the sidewall of the MWNT to be similar to the basal plane of HOPG with tube ends, or defects in the sidewall being compared to edge plane sites.[2, 16, 17] Figure 3.1 shows a schematic of HOPG highlighting the location of the basal plane and the edge plane sites.

Studies on HOPG have largely suggested, from CV analysis alone, that the electrochemical activity of HOPG is attributed primarily to the edge plane, with ET kinetics at the basal plane being significantly slower.[18, 19] Thus it was assumed the sidewall of the MWNT is largely inactive with only edge-like defects, which occur as a graphene layer terminates or at an open end, being responsible for ET.

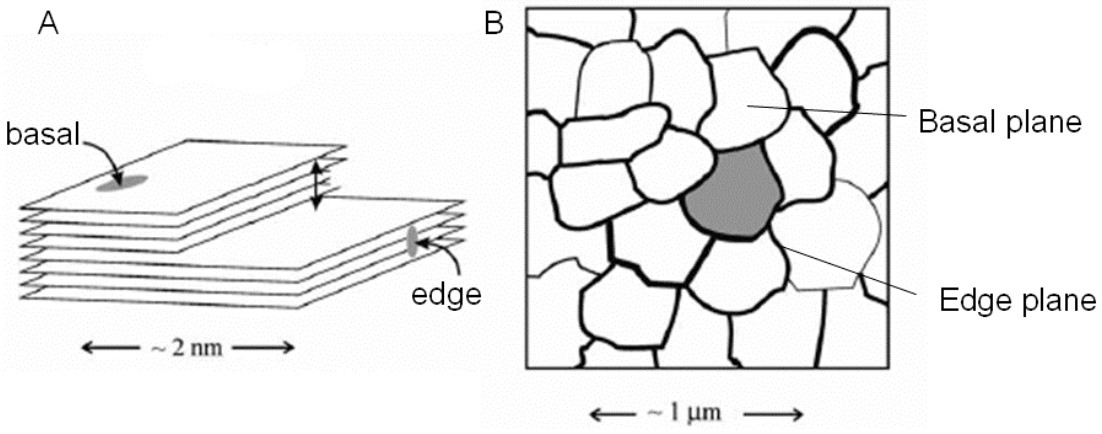

Figure 3.1 (a) Schematic of HOPG showing the basal and edge plane sites. (b) Activity of basal plane cleaved HOPG is confined to edge plane bands as proposed by Davies *et al.*[18]

Using voltammetric studies on HOPG, Banks *et al.*[17] demonstrated slower ET for the basal plane of HOPG, whilst reversible ET was seen for a surface consisting of predominantly edge plane graphite. When the basal plane HOPG was modified with MWNTs the electrochemical response observed was similar to that for edge plane graphite. Similar work by Moore *et al.*[20] further complicated the situation by reporting that a similar electrocatalytic effect to MWNTs could be achieved on basal plane HOPG by modification with graphite powder. A modified basal plane HOPG electrode was used to investigate the effect MWNT structure (*e.g.* herring bone or hollow tube) had on the observed CV response. The conclusion was drawn that MWNT structure had minimal effect on the CV response of the modified electrode, and again assumed that ET was observed at the edge plane like defects caused by open CNT ends and open side walls.[3]

Based upon the work drawing comparisons between HOPG and MWNTs, SWNTs were assumed to exhibit the same ET properties of MWNTs, *i.e.* sidewall relatively inactive to ET with defects of ends active.[15, 21] Liu *et al.*[22] observed that a 2D

horizontal array of SWNT had slower ET than a vertically grown SWNT array. From this they inferred that as there was probably a higher density of end sites in the vertically arranged SWNTs, that it was the end sites which were the major contributor to the increased ET.

From these findings a model for ET activity being due to discrete active sites is proposed based upon the experimental configuration. This model is described in detail in section 3.4.1

3.2.2. Electrochemical Activity of the Sidewall

Contrary to the reports highlighted in section 3.2.1 there is strong evidence to support the theory that ET occurs at the sidewall of a CNT. Work by Heller *et al.*[23] using an individual SWNT on an insulating support as the electrode (ends were not exposed to solution) showed that the electrochemical response increased with the increasing length of exposed SWNT. Gong *et al.*[24] showed that the electrochemical activity of the tips and sidewalls of CVD grown CNT forests varied depending upon the mediator being studied, for example the oxidation of H_2O_2 was observed on the CNT sidewall but not on the tips. The synthesis of a CNT network on an insulating support *e.g.* SiO_2, allows for the CNT network electrode to be studied without interference from a conducting support.[25, 26] By deliberately introducing defects by acid cleaning and oxygen plasma ashing, Dumitrescu *et al.*[27] demonstrated that the most noticeable effect was a decrease in network conductivity. Moreover, at suitably low currents to avoid Ohmic drop, for electrolysis of the outer sphere redox mediator $Ru(NH_3)_6^{3+}$ the quantity of defects did not affect the voltammetric response. In light

of these reports the opposing theory, that the entire SWNT side wall is active, is proposed. Further examples of the electrochemical activity of CNTs are available in the recent review by Dumitrescu *et al*.[13]

The model for the sidewall being electrochemically active is proposed from the evidence reported within this section, and will be discussed in more detail in section 3.4.2.

3.2.3. Defects on carbon nanotubes

The theory of discrete active sites proposes that defects within the SWNT sidewall are solely responsible for ET at a SWNT. In this report the term defect refers to any point where the regular graphitic lattice of the outer wall is disrupted. In the case of MWNTs, where the outer layer is broken edge plane like defects are observed, this is reported to occur either regularly in the case of "herring bone" and "bamboo" like MWNTs or irregularly for MWNTs with concentric tubular layers, as shown in figure 1.23.[2, 3] In addition to the step edge defects there are additional faults within the graphene lattice,[28-31] including non-hexagonal hybridization *e.g.* Stone-Wales,[32] vacancies,[33] and local impurities.[34] These defects are illustrated in figure 3.2.

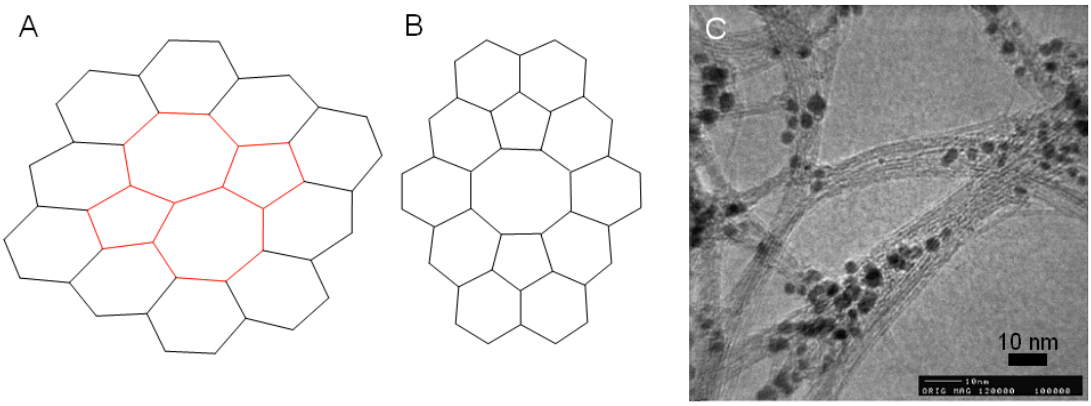

Figure 3.2 Schematic of several common lattice defects found on a CNT (a) Stone-Wales hybridization, and (b) a vacancy site. (c) Transmission electron microscopy showing impurities on the CNT surface.[35]

The SWNTs used within this chapter are all synthesised by CVD. As a result the SWNTs have a low density of defects, negligible amorphous material on the sample and also the SWNT ends are closed. The number of defects along the length of CVD synthesised SWNTs has been studied by various techniques, including scanned gate AFM to show points of varying resistance and defect driven metal nanoparticle deposition,[36, 37] although it must be noted that these techniques do not reveal all defects. Previous studies by Day *et al.*[37] and Fan *et al.*[36] have shown that metal electro-deposition at very low driving force occurs initially at discrete locations, which indicate sites of favourable surface energy for nucleation, thought to be defect sites. The smallest spacing between nucleated metal nanoparticles along an individual SWNT was found to be ~100 nm; however the average spacing of nanoparticles reported by Fan *et al.* was up to ~4 μm apart. For both studies as the nucleation driving force increased the number of nucleation sites also increased moving towards contiguous nano-wire formation.

3.3. Experimental Overview

This section presents the experimental concepts and techniques employed to experimentally distinguish between the two proposed cases for ET at a SWNT network electrode.

3.3.1. Reducing the Rate of Diffusion

The critical difference between the two theories is the quantity and geometry of the active parts of the SWNT, as this affects the resulting diffusion profile to the electrode on a short time scale. Work by Bertoncello *et al.*[25] utilising a droplet (10 μL, ~4 mm diameter) placed directly onto a SWNT network showed that on the typical time scales of aqueous electrochemical measurements (CVs at a scan rate of 100 mV s^{-1}) the diffusion profiles overlapped, giving a Faradaic current response identical to a macroelectrode of the same dimensions. To observe diffusion profiles associated with individual SWNTs, one approach is to significantly reduce the rate of diffusion of the electroactive species to the SWNT network. Previous work by Edwards *et al.*[1] utilising a HOPG electrode modified with a ~90 nm thick Nafion™ film showed that the apparent diffusion coefficient of a redox mediator (*e.g.* $[Ru(NH_3)_6]^{3+/2+}$) could be reduced by up to 5 orders of magnitude. This technique is applied here to HD SWNT networks in preference to the VHD films as there is a greater separation between the SWNTs in the HD arrangement thus providing a longer timescale before diffusion profiles overlap.

3.3.2. Experimental Techniques

Each HD SWNT sample was characterised by taking multiple AFM images. Only samples with a network density in the range of 3 μm μm^{-2} - 4 μm μm^{-2} were used for analysis. A Pt disc UME was prepared by sealing a 25 μm diameter Pt wire (Goodfellow, England) within a borosilicate capillary and polished flat using silicon carbide paper (SIC Paper #4000, Struers) and progressively finer grades of diamond impregnated polishing pads (Buehler, Germany).[38, 39] To facilitate the deposition of the drop cast film onto the UME the radius of the insulating sheath was ~2 mm.

Nafion™ (Aldrich) was drop cast onto a SWNT network or 25 μm Pt UME from stock solution (5% wt in aliphatic alcohol/H_2O) using a micropipette tip (Finn, Thermo Scientific) and allowed to dry under room conditions (figure 3.3 (a)). For the SWNT samples the droplet diameter was measured by an optical microscope (Olympus BH2). The average drop cast film diameter was approximately 1.1 mm with a thickness of ~100 μm. The Nafion™ was pre-concentrated with mediator by soaking in an aqueous solution of 2 mM $FcTMA^+$ in 0.1 M NaCl for at least 18 hours. After soaking the SWNT sample was attached to a glass microscope slide by gelpack and rinsed under double distilled H_2O and dried using a gentle flow of nitrogen. A borosilicate capillary (1.5 mm outer diameter 0.86 mm inner diameter, Clark Electromedical Instruments) containing 0.1 M NaCl and a chloridised silver wire, used as a reference electrode for SWNT experiments, was lowered onto the Nafion™ film using a micrometer equipped micropositioner (Newport). Electrical connection to the network was made by touching the gold band with a needle tipped micro-positioner (Quater Research) (figure 3.3 (b)).

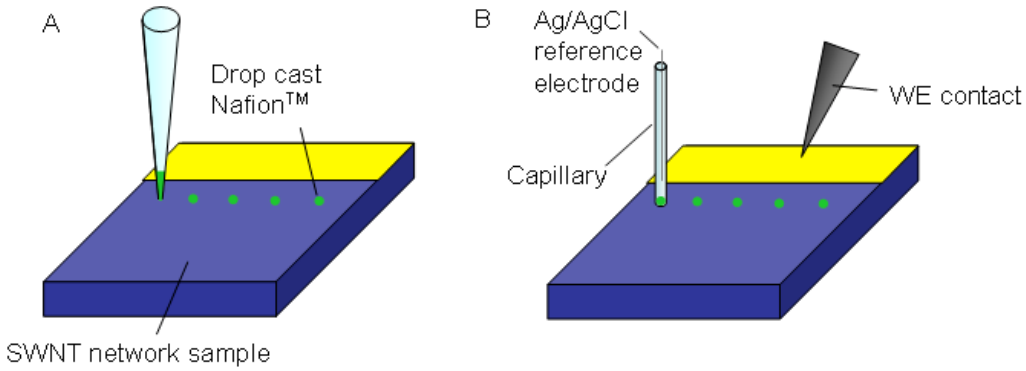

Figure 3.3 Schematics of the experimental techniques used for probing the electroactivity of the SWNT network. (a) Nafion™ is drop cast onto the sample prior to preconcentration. (b) A capilary containing only supporting electrolyte and a Ag/AgCl reference electrode is lowered over the drop cast Nafion™ film.

The Nafion™-Pt UME was used by directly placing the UME into a solution containing 0.1 M NaCl and a chloridised silver wire was used for the reference electrode. Electrochemical measurements were taken using a CHI 760C Bipotentiostat (CH Instruments). Repeat measurements were taken on samples after rinsing and soaking in the mediator solution for at least half an hour.

3.4. Finite Element Modelling

Two models are proposed for the competing theories for the sites of ET at a SWNT electrode. Here we use a 2D random network of SWNTs. The FEM approximations to the experimental setup are described and the assumptions of each model are discussed. Both models assume the electrochemically driven reaction at the surface of the SWNT is complete and instantaneous, with mass transport driven solely by diffusion.

3.4.1. FEM of the Discrete Active Site Theory

The discrete active site model considers the SWNT sidewall to be electrochemically inert, except for active "defect" sites which are spaced randomly along the length of the SWNT. Each active site is considered to be an equally sized disc, approximated to the SWNT diameter, in the plane of the sample.

A diffusional domain approach was used to calculate the current response as described by Davies *et al.*[40, 41] A Monte Carlo simulation was performed to generate the location of the active sites on the SWNT network. Initially the locations of SWNTs were generated under the assumption that the SWNTs were linear, of infinite length, and with a specified density (figure 3.4 (a)). Active sites were considered to be of equal size and positioned randomly on the SWNTs (figure 3.4 (b)). Following the method of Davies *et al.*[40, 41] a Voronoi mesh for the active sites was calculated (figure 3.4 (c)).

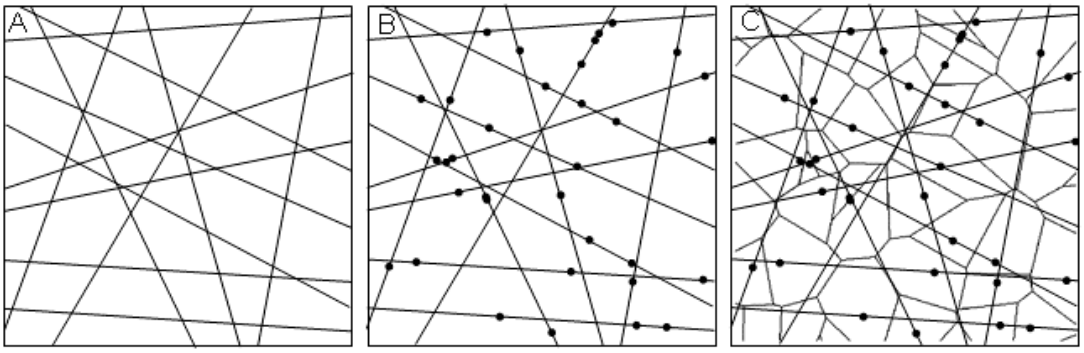

Figure 3.4 Schematic to show the calculation of Voronoi cells for the active site model. (a) Straight SWNTs are placed randomly to generate the network, (b) active sites are placed along the SWNTs, (c) the Voronoi cells for each active site is calculated.

The contribution of an individual active site was then approximated by a disc within an insulating cylinder of equal area to its Voronoi cell, (figure 3.5). Details of the model calculating the current to an individual defect are given below. Perimeter cells were discarded as neighbouring defects which were not necessarily included could bias results. The area of the simulated domain was sufficiently large so that increasing the area of domain did not affect the current density response.

For the discrete active site simulation the individual active sites were approximated as an electrochemically active disc, radius r_1, within a cylinder, radius r_2, with insulating walls of height, h, governed by the thickness of the Nafion^{TM} layer. Each site contributed to the overall current response of the network. The 2D axially symmetric geometry of a disc within an insulating cylinder is shown in figure 3.5 with z and r being the axial and radial coordinates respectively.

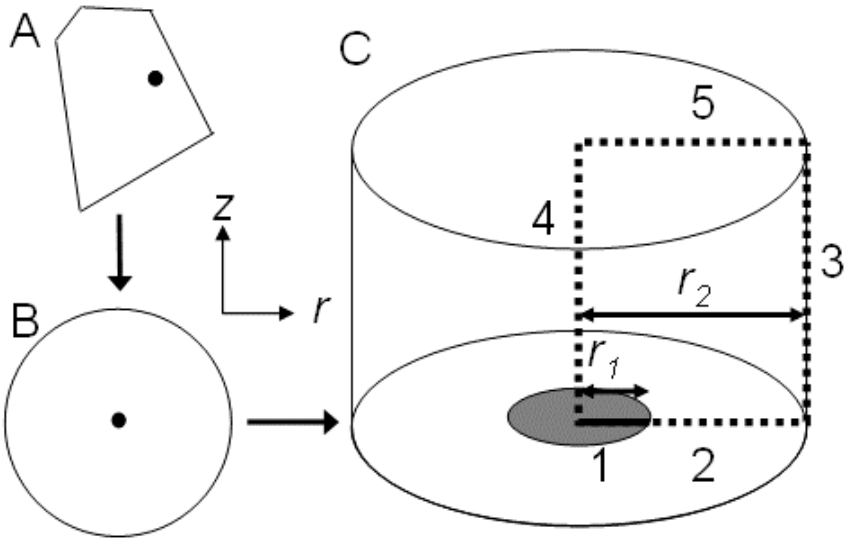

Figure 3.5 (a) Translation of a Voronoi cell to (b) an isolated active disc of radius r_1 within an insulating cylinder of radius r_2, where r_2 is controlled by the the area of the Voronoi cell. (c) The unit cell for the 2D axial symmetric domain (dashed line) is shown with boundary numbering conventions

Edge 1 represents the active site where the following reaction (equation 3.1) is considered:

$$R \rightarrow O + ne^- \quad \textbf{(3.1)}$$

A potential step from a value where R is not electrolysed to a potential where the complete oxidation of species R to species O occurs is applied to the electrode at a time, t = 0 s. The time-dependent diffusion equation (equation 3.2) was solved for species R within the interior of the domain shown in figure 3.5.[42, 43]

$$\frac{\partial c}{\partial t} = D_{app} \nabla^2 c \quad \textbf{(3.2)}$$

where D_{app} and c are the apparent diffusion coefficient and concentration of species R within the Nafion™ film, respectively. The reaction is considered to be complete and instantaneous at the active site, edge 1, which can be expressed by the boundary condition described in equation 3.3

$$c = 0 \quad \textbf{(3.3)}$$

Edge 2 represents the electrochemically inactive Si/SiO_2 substrate, of radius r_2 chosen for each diffusion domain as described previously, and was set to have no normal flux, as shown in equation 3.4.

$$\nabla c \cdot \underline{n} = 0 \quad \textbf{(3.4)}$$

where $\underline{n}$ is the inward pointing unit normal vector.

The diffusion domain approach dictates that there was no normal flux along the entirety of axis (3) and cylinder edge (4). Edge (5) represents the upper limit of the Nafion™ film, it was assumed that there was no net transfer of mediator out of or into the film, thus equation 4 sufficed as the boundary condition. The domain surrounded by edges 1-5 is initially set to be at the bulk concentration, c_b, of the saturated Nafion™ film as determined by experiments on the drop cast Nafion™ modified 25 μm diameter Pt UME in section 3.5.1. The current, i, generated by an individual active site can be calculated by integrating the flux to boundary 1 and multiplying by $2\pi r_1 F$, where F is Faraday's constant (96485 C mol^{-1}). The overall response is the sum of all active sites within the simulated area.

The two assumptions made by this model are that the defects are of uniform size and that the individual diffusion domains can be approximated to a cylinder. The defect size is assumed to be the same as the radius of a SWNT, which maximises the expected amount of active material for this model, in turn maximising the current response of this model. The assumption that the individual Voronoi cells can be approximated to a cylinder is valid as long as the defect spacing is sufficiently large so that diffusional overlap is not dominated by active sites along the same SWNT (minimum spacing of ~100 nm).

3.4.2. FEM model of sidewall activity

The situation where the entire sidewall of the CNT is electrochemically active was approximated by an array of parallel tubes upon an insulating surface (figure 3.6 (a)), with the average inter tube spacing, *w,* was chosen to match the sample density. The time-dependant diffusion equation (equation 3.2) was solved for the interior of the domain as shown in figure 3.6 (b), which represents the 2D repeating unit of the model. The initial concentration was set to the bulk concentration throughout the interior of the domain. As for the active site model the oxidation of species R is assumed to be complete and instantaneous at the electrode surface (edge 1) and is implemented by applying the boundary condition expressed in equation 3.3 to this edge. Edges 2 and 5 have no normal flux as explained previously in section 3.4.1, and edges 3 and 4 have no normal flux due to the 180° reflection symmetry of the unit cell, the boundary condition on these edges is described in equation 3.4. The current density, *j*, is calculated by integrating the flux at edge 1, multiplied by *F* divided by the domain width.

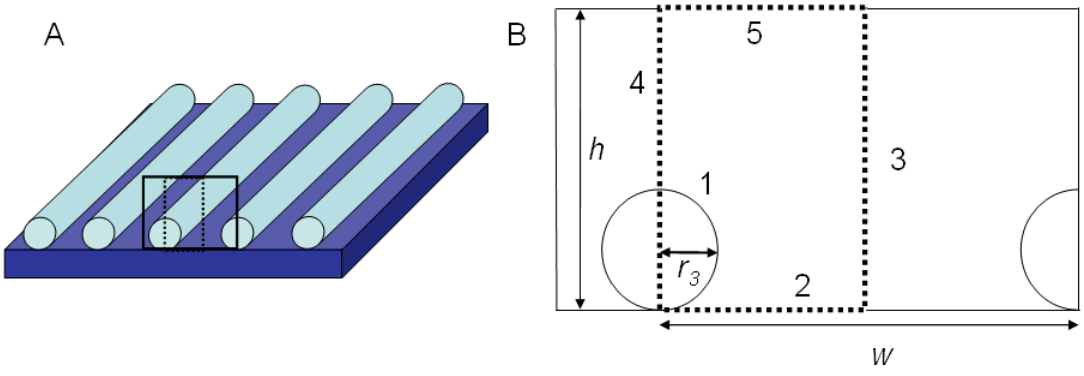

Figure 3.6 (a) Representation of the SWNT parallel array, the boxed area is shown in more detail in (b) where the 2D repeating unit (dashed line) and boundary labelling conventions are shown.

This model assumes that the randomly distributed SWNT network is a uniform array of SWNTs where the entire sidewall is active. The approximation allows the problem to be simplified to the 2D domain shown in figure 3.6 (b), greatly reducing the computational time required for each simulation compared to the 3D model required to explicitly simulate a random network. It should be noted that this provides an idealised diffusive response as sections where the experimental SWNTs are not at the average spacing will experience diffusional overlap at different times.

As the area of the electrode for the experimental measurements is large the average spacing is a reasonable approximation. However, the theoretical features of the current-time response are expected to be more defined due to the uniform nature of the simulation. The simulation should over-estimate the current response compared to that observed experimentally, as the SWNTs are assumed to be uniformly active. However, the SWNTs within the network electrode are a random mixture of semi conducting, metallic, or quasi-insulating (non-conducting due to no connection to the network or defects on the SWNT) and as such are likely to have different ET properties.[44]

3.4.3. Insights from Simulations

The two theoretical models show different sites for ET at a SWNT, and thus will result in differences in the developing diffusion profiles when the SWNT is operated as an electrode for the electrolysis of an electroactive species. This section uses D_{app} = 1 x 10^{-10} cm^2 s^{-1}, obtained experimentally in section 3.5.1 when Nafion^{TM} is used to slow down diffusion. It is important to note that a higher diffusion coefficient will make the transition from isolated diffusion profiles around an individual active site or

sidewall to linear diffusion, due to overlapping diffusion fields, occur on a shorter time scale.

Figure 3.7 presents the development of the diffusion profile for one active site within the discrete active site model. For the discrete active site model, at short times (~10^{-5} s) linear diffusion to the active site is evident (figure 3.7 (a)) (domain 1). At longer times ($t > 10^{-4}$ s) this profile begins to change into hemispherical diffusion (figure 3.7 (b)) (domain 2). After sufficient time (~ 2 s) the affect of neighbouring active sites is apparent as the concentration gradient now begins to reflect linear diffusion (figure 3.7 (c)) (domain 3). The example shown in figure 3.7 has an active site spacing of 100 nm.

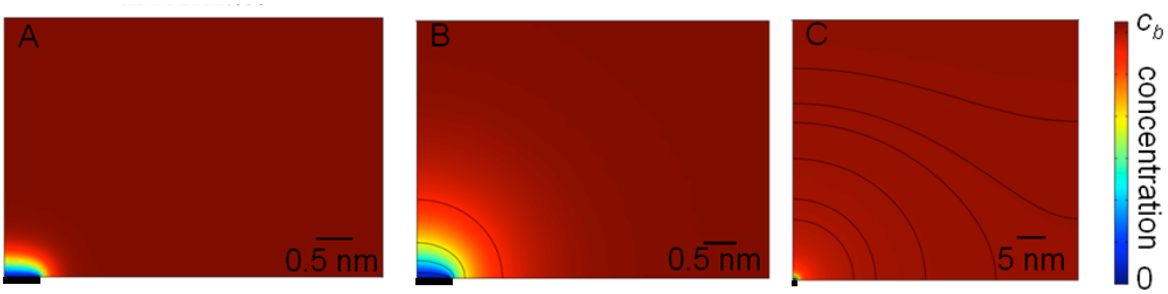

Figure 3.7 (a) The initial linear diffusion to an active site (t ~10^{-5} s) (domain 1), (b) the developed hemispherical diffusion ($t > 10^{-4}$ s) (domain 2) and (c) transition to the final linear response (domain 3) where diffusional overlap occurs with a neighbouring defect site 100 nm away (t ~ 2 s). Black box represents location of active site.

The time dependant diffusion profile to a SWNT for the sidewall active model can also be broken down into 3 domains. However, the development of the diffusion profiles is different to the discrete active site model within domains 1 and 2. At short timescales (t ~10^{-5} s) the cylindrical shape of the active sidewall results in a hemispherical diffusion profile being established quickly (figure 3.8 (a)) (domain 1). The expansion of the diffusion layer with time is cylindrical in domain 2, as shown in

(figure 3.8 (b)). Finally the diffusion profile overlaps with that of the neighbouring SWNT at ~1 s (figure 3.8 (c)) to provide linear diffusion (domain 3). The transition from isolated sites (domain 2) to when diffusional overlap between neighbouring sites (domain 3) occurs at ~1 s for the sidewall active model compared to ~2 s for the smallest defect spacing of 100 nm used in the discrete active site model.

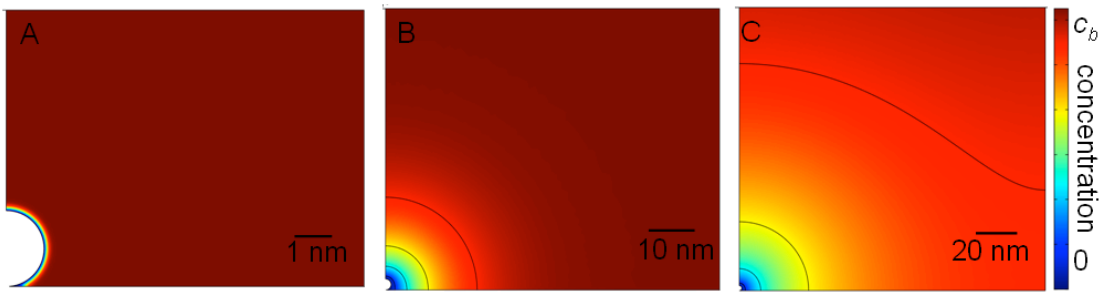

Figure 3.8 Diffusion domains for the sidewall active model with a network density of 3 μm μm^{-2}, (a) domain 1, rapid development of a hemispherical diffusion profile (t ~10^{-5} s), (b) domain 2, expansion of the hemispherical diffusion profile (t > 10^{-4} s), and (c) diffusional overlap with neighbouring SWNTs (t ~1 s) (domain 3).

As the flux is dependant upon the diffusion profile the two models produce different flux - time responses for domains 1 and 2. As described in sections 3.4.1 and 3.4.2 the flux is proportional to the current, hence the CA response of the systems will be different in domains 1 and 2. The log j – log t response for both models is shown in figure 3.9. The different time-dependent diffusion profiles, presented above, can be seen in the corresponding current-time decay responses. The key differences between both models is the development of a plateaux in the log j - log t response for the discrete active site model compared to a gradual decay observed for the sidewall active model. This occurs within domain 2 due the discrete active sites

being isolated nano-disc electrodes compared to the sidewall active model consisting of isolated nano-band electrodes. Thus, within domain 2, the active site model will provide a steady state current, whereas the sidewall active model does not reach a transport limited steady state response. The overlap of the diffusion profiles (domain 3) also occurs earlier for the sidewall active model (t ~1 s) than for the discrete active site model (t ~2 s). Hence it should be possible to discriminate between the two proposed models based upon the current density-time data obtained experimentally.

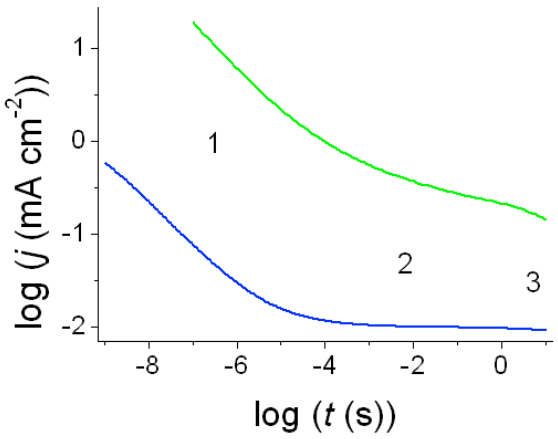

Figure 3.9 Comparison of the theoretical response for the discrete active site model for active site size of 0.5 nm and network density of 4 µm µm^{-2} (—) to the side wall active array model with radius 0.5 nm and network density of 3 µm µm^{-2} (—) for a drop cast NafionTM film with D_{app} = 1.00 x 10-10 cm^2 s^{-1} and c_b = 1.25 mol dm^{-3} for a tube. Numbers 1-3 represent diffusion profile domains 1-3 which are described above.

3.5. Results and Discussion

3.5.1. Characterising the Drop Cast Nafion^{TM} Film

The dropcast Nafion^{TM}/FcTMA^{+} film was electrochemically characterised on a 25 μm diameter Pt UME. The diffusion limited potential for the oxidation of FcTMA^{+} at the Pt-Nafion^{TM} modified UME was first determined by CV as shown in figure 3.10 (a). The transport properties for the redox mediator FcTMA^{+} within the drop cast Nafion^{TM} film were then extracted using CA by stepping from 0 V to the diffusion limited potential (0.5 V vs Ag/AgCl). The limiting current (i_{lim}) was extrapolated from the intercept of i vs $t^{-1/2}$ from the chronoamperometric data. The maximum and minimum experimentally observed values of i_{lim} = 0.80 ±0.20 nA (5 repeats) were considered, in order to give error bounds on D_{app}.[45, 46]

The *i-t* transients were analysed using the Shoup-Szabo equation[47] to extract D_{app} independently of knowledge of the bulk concentration (c_b) as shown in figure 3.10 (b). The currents were normalised with respect to i_{lim} against $t^{-1/2}$. The values for D_{app} and c_b at the extremes of the error range are considered to allow for any uncertainty in the measured properties of the film to be taken into account, at i_{lim} = 1 nA D_{app} = 3.02 x 10^{-10} cm^2 s^{-1} and c_b = 0.325 mol dm^{-3} and at i_{lim} = 0.6 nA, D_{app} = 1 x 10^{-10} cm^2 s^{-1} and c_b = 1.25 mol dm^{-3}. It is also worth noting that the Pt UME only fits the Shoup-Szabo equation for times greater than 0.3 s due to capacitive effects and other non-Faradaic processes contributing at shorter times.

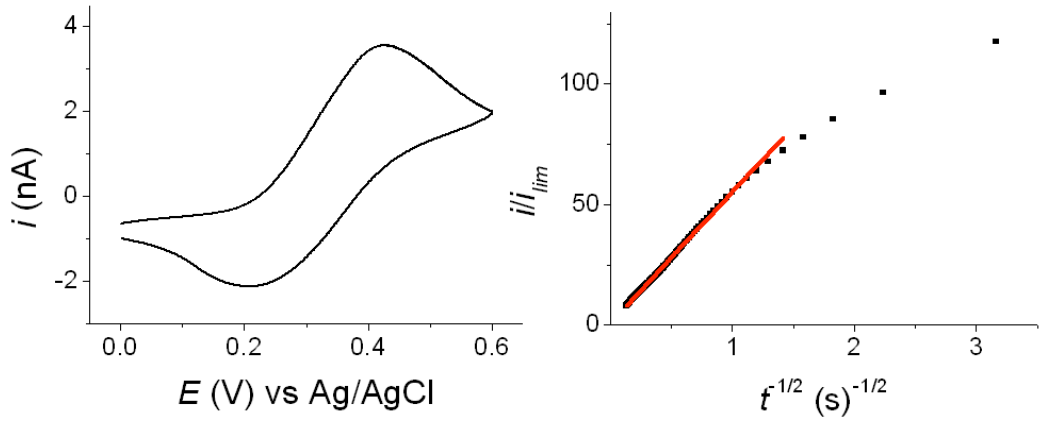

Figure 3.10 Experimental data for the drop cast NafionTM modified Pt UME used for the characterisation of the NafionTM film (a) CV at 100 mV s^{-1} used to determine the over potential and (b) Shoup-Szabo analysis of CA data.

As shown by the FEM simulations in section 3.4.3 a value of D_{app} of ~1 x 10^{-10} cm^2 s^{-1} should allow the differences in the developing diffusion profiles for the two proposed ET models to be distinguished on a typical experimental timescale. For the highest diffusion coefficient obtained (3 x 10^{-10} cm^2 s^{-1}) the maximum distance travelled (d) by diffusion only is predicted to be 50 nm when $t \approx 0.1$ s using equation 3.5. Given that the typical spacing between SWNTs is ~100 nm, the D_{app} values will provide a suitable time period to observe the development of the diffusion profiles.

$$\sqrt{d} = Dt \qquad \textbf{Equation 3.1}$$

The value for D_{app} determined in the drop cast Nafion^{TM} films is higher than the value reported for films formed by the Langmuir-Blodgett method by two orders of magnitude.[1, 48, 49] This could be due to the different deposition and drying methods resulting in the films with different general structure and order.[50-52]

3.5.2. Characterisation of SWNT Samples

Figure 3.11 (a) and (b) show an AFM image of a typical SWNT network, which has a network density of 3.3 μm μm^{-2}. To avoid contamination of the sample arising from FE-SEM, the density was characterised by recording several AFM images in different locations. An FE-SEM image, taken after experiments, of a typical SWNT network (figure 3.11 (c)) demonstrates the distribution of SWNTs is not quite uniform across the sample. To take into account density variations the values of 3 and 4 μm μm^{-2} were used in the theoretical calculations. The majority of SWNTs have a height between 0.8 nm and 2 nm, with the occasional bundle being up to 3.5 nm in height as seen in the inset of figure 3.11 (a) and (b). Taking into account the variation in SWNT height values of 1 nm and 3 nm were assumed for the theoretical calculations. It should be noted that an average height of 3 nm at a density of 4 μm μm^{-2} is the upper-limit for SWNT surface area and is greater than that observed experimentally; these values were chosen to provide a theoretical upper limit on the current density for both models.

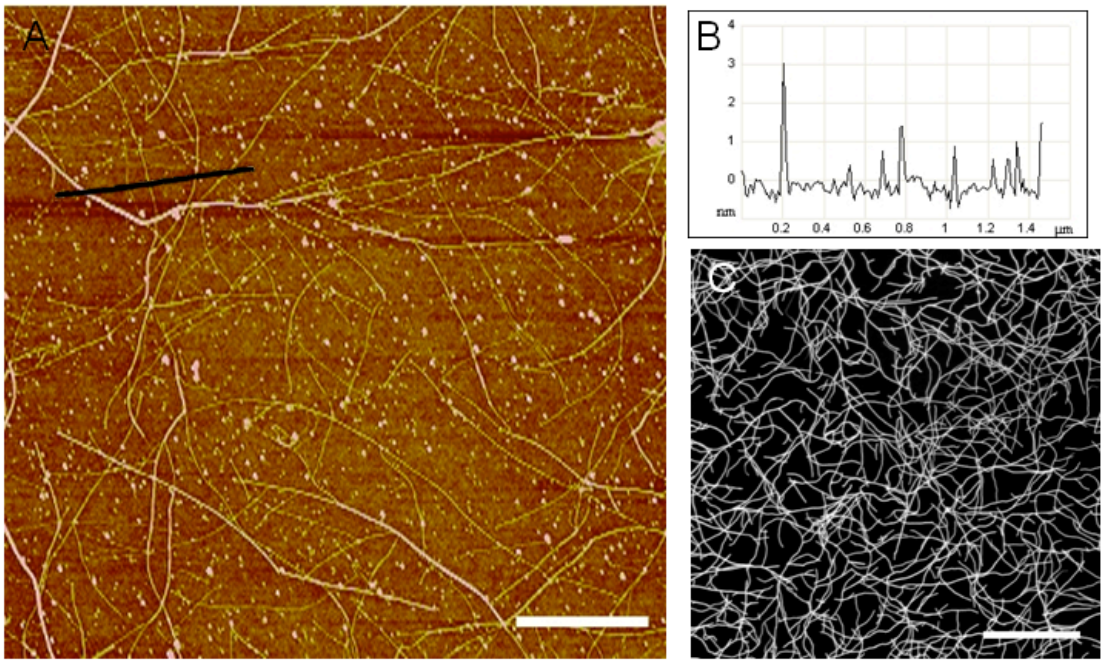

Figure 3.11 (a) Typical AFM image of a SWNT network of density 3.3 µm µm^{-2} used *x* and *y* scale bar is 1 µm, *z* scale bar 5 nm. (b) Shows a cross section of the sample, taken from the black line in (a), where the height of a bundle of SWNTs is 3 nm and the height of individual SWNTs are between 0.8 nm and 1.5 nm (c) SEM image showing the variation in density over the sample (scale bar 6 µm).

3.5.3. Drop Cast Nafion^{TM} Modified SWNT Networks

The driving potentials for chronoamperometric analysis were chosen based on the CV data recorded on the $FcTMA^+$ loaded Nafion^{TM} modified SWNT networks. Figure 3.12 (b) shows the results of CV at 100 mVs^{-1} for the oxidation of $FcTMA^+$. From this wave it is possible to calculate the diffusion limited, three quarter wave ($E_{3/4}$), half wave ($E_{1/2}$) and quarter wave ($E_{1/4}$) potentials of 0.5 V, 0.42 V, 0.38 V and 0.32 V respectively. Work by Bertoncello *et al.*[25] demonstrated that the CV response of the oxidation of $FcTMA^+$ on a bare SWNT network electrode produced a characteristic peak shaped macro-electrode response (figure 3.12 (a)), due to the

complete overlap of diffusion fields of neighbouring SWNTs on the timescale of the measurement.[52] In contrast, in the presence of Nafion™ it can be seen that a quasi steady-state regime is established for potentials equal to or greater than 0.5 V on the forward scan (figure 3.12 (b)). This indicates that diffusion to the network has been significantly reduced for $FcTMA^+$ so that the diffusion fields of neighbouring sites do not sufficiently overlap.

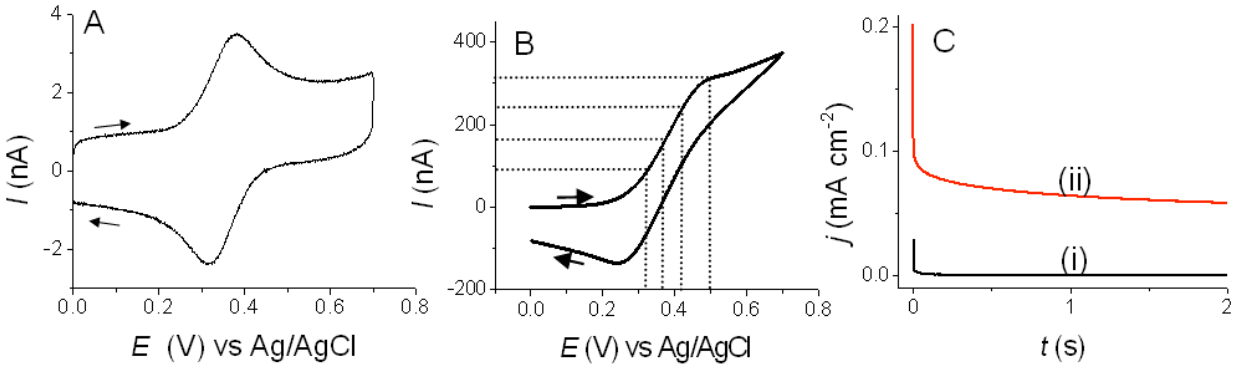

Figure 3.12 (a) CV of a droplet upon a bare SWNT network.[25] (b) CV on the drop cast Nafion™ modified HD SWNT network used to determine part potentials for the CA measurements (dashed lines). (c) Comparison of CA response of a drop cast Nafion™ film prior to (i) and after pre concentration with $FcTMA^+$ (ii) where the potential step is from 0 V to 0.5 V.

The CA response of the SWNT-Nafion™ sample prior to saturation (i) with $FcTMA^+$ is compared to that obtained with the $FcTMA^+$ saturated Nafion™ (ii) as shown in figure 3.12 (c). The former *i-t* response (i) indicates that any charging, resistive effects or other non-Faradaic processes within the film have a minimal impact upon the $FcTMA^+$ oxidation chronoamperometric response (ii). For both cases the potential is stepped from 0 V to 0.5 V.

Chronoamperometry at the $FcTMA^+$ loaded SWNT-Nafion^{TM} electrodes show a linear scaling of current density when stepping to different driving potentials *i.e.* $E_{1/4}$, $E_{1/2}$, $E_{3/4}$ and the diffusion limited potential (figure 3.13 (a)). By driving the oxidation of $FcTMA^+$ at different potentials it may be possible to provide information on whether the defects or sidewall are of uniform activity or have a potential dependant activity. This is of interest as the reduction of metal at the SWNT surface is observed to occur at discrete sites when the driving potential is low, however as the potential is increased a higher density of metal particles is observed before the entire SWNT has metal deposited upon the SWNT surface. As the current-time transients in figure 3.13 exhibit the same general shape when the driving potential is varied, it is thus unlikely that there is a potential dependant switch in the sites of ET at the SWNT electrode.

In general on the CA curves three distinct regions are visible as shown in figure 3.13 (b). For times less than 1 ms there is a linear relationship between log *i* and log *t*, for times between ~1 ms and 0.5 s the gradient becomes less negative, indicating a change in the diffusion profile to the surface, and a finally for times greater than 0.5 s the gradient starts to become more negative. For comparison to the theoretical models the current density is reported.

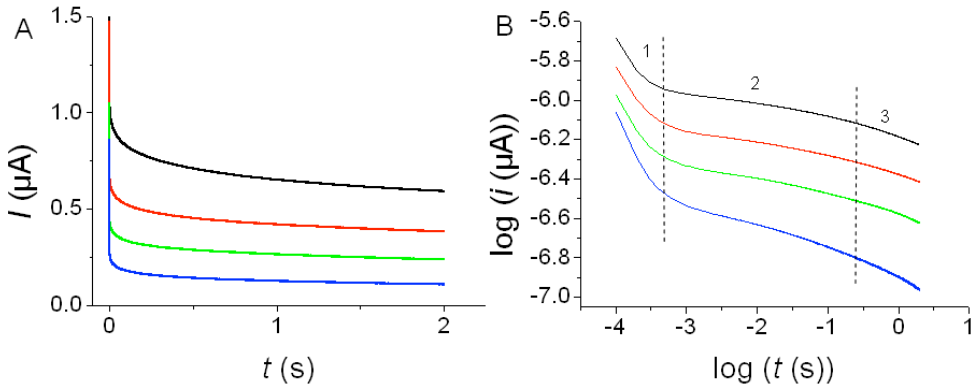

Figure 3.13 (a) Chronoamperometry of drop cast Nafion™ on SWNT network saturated with $FcTMA^+$ at the diffusion limited potential (—) $E_{3/4}$ (—) $E_{1/2}$ (—) and $E_{1/4}$ (—) showing linear scaling between the different driving potentials. (b) Comparison of the current – time decay by logarithms.

3.5.4. Comparison of Experimental Data to the Discrete Active Site Model

The effect of different SWNT network densities and the size of active sites is shown theoretically for the active site model in figure 3.14 for both the upper (a) and lower (b) limits of D_{app} and c_b in the Nafion™ film. It is important to note that the reported current densities are for an area of the insulating substrate, hence the difference in reported current densities relates to the variation in the quantity of active material present upon the surface. In figure 3.14 it can be seen that by increasing the radius of the active sites from 0.5 nm to 1.5 nm the predicted current density for the whole sample area increases due to the increasing area of active material upon the sample. Similarly as the network density increases from 3 μm μm^{-2} to 4 μm μm^{-2} the current density for the sample increases due to a higher density of active sites. The transients presented in figure 3.14 are all shown for the smallest expected average

spacing of active sites (100 nm) and as such represent upper bounds for the predicted current response.

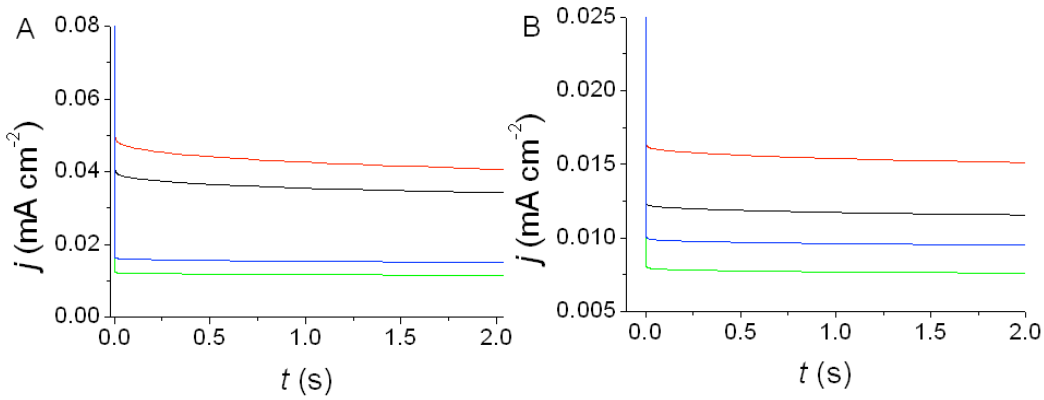

Figure 3.14 Theoretical response for the discrete active site model for a sample of (—) defect radius 1.5 nm, network density 4 µm µm^{-2}, (—) defect radius 1.5 nm, network density 3 µm µm^{-2}, (—) defect radius 0.5 nm, network density 4 µm µm^{-2}, (—) defect radius 0.5 nm, network density 3 µm µm^{-2} for (a) D = 3 x 10^{-10} cm^2 s^{-1} and c_b = 0.325 mol dm^{-3} (b) D_{app} = 1.00 x 10^{-10} cm^2 s^{-1} and c_b = 1.25 mol dm^{-3}.

A comparison of the experimental current density with the active sites model is shown in figure 3.15. The experimental current density is greater than that predicted by the simulations for all theoretical parameters considered. The largest theoretical current density (red line in figure 3.14 (a) and figure 3.15) is for the maximum SWNT density (4 µm µm^{-2}), D_{app} (3 x 10^{-10} cm^2 s^{-1}), largest defect size (3 nm diameter) and the smallest average defect spacing (100 nm).[37, 53, 54] Larger defect separations result in a decrease in the predicted current density for the sample area as there is a reduced active area, as shown by decreasing the network density in figure 3.14. Typical SWNT heights observed by AFM and SWNT network densities observed by AFM and FE-SEM data (figure 3.11) show that these values represent maximum values for both network density and active site diameter. Hence the value for the largest current

density represents a generous upper limit on the current density we could expect from ET occurring solely at isolated active sites.

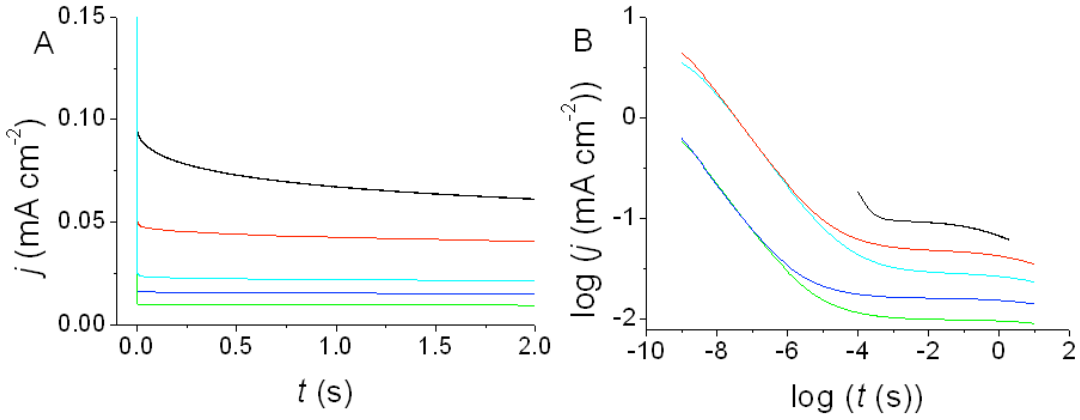

Figure 3.15 Comparison of (—) experimental data to the theoretical responses for the discrete active site model for networks of density 4 µm µm^{-2} with an active site spacing of 100 nm, D = 3 x 10^{-10} cm^2 s^{-1} and c_b = 0.325 mol dm^{-3} for sites of (—) 1.5 nm radius and (—) 0.5 nm radius, and for D_{app} = 1.00 x 10^{-10} cm^2 s^{-1} and c_b = 1.25 mol dm-for sites of (—) 1.5 nm radius and (—) 0.5 nm radius

As the predicted response for the active site only model is lower than the current density response observed experimentally, as shown in figure 3.15 (a), this suggests that the experimental response cannot be attributed solely to isolated active sites. It could be argued that SWNT open ends and catalytic metal nano-particles contribute to the measured *i-t* response. As the simulation does not explicitly take into account these additional sites for electron transfer the predicted response is an under-estimate of the experimental conditions. However, using CVD the grown SWNTs are highly likely to have closed ends.[55] Additionally, as the majority of the iron catalyst nanoparticles are not in contact with the SWNT network and sit isolated on the insulating SiO_2 support it is unlikely they have an electrical connection to the SWNT

network. Therefore the contribution of any active end sites and connected catalyst particles to the experimentally observed current density is negligible.

3.5.5. Comparison of Experimental Data to Parallel Tube Model

The situation where the entire SWNT sidewall is active was investigated using a range of parameters with D_{app} of 1 x 10^{-10} cm^2 s^{-1} and 3.02 x 10^{-10} cm^2 s^{-1} for values of c_b of 1.25 mol dm^{-3} and 0.325 mol dm^{-3} respectively, network density (3 µm $µm^{-2}$ and 4 µm $µm^{-2}$) and SWNT radius (0.5 nm and 1.5 nm). Figure 3.16 shows the theoretical current density-time response for these parameters compared to the experimental response. As for the discrete active site model the current density is largest for the higher density networks with the largest SWNT radius (figure 3.16).

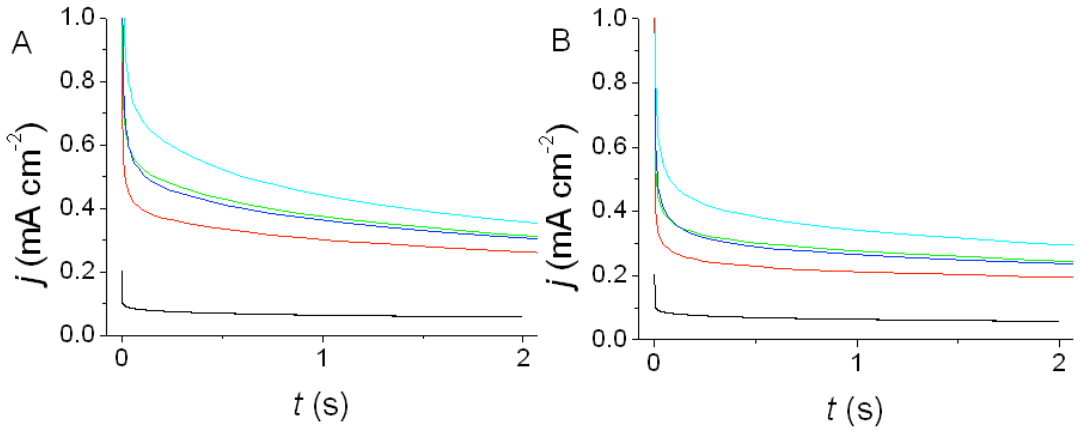

Figure 3.16 Comparison of experimental data (—) where the potential is stepped from 0 V to 0.5 V to the all active parallel tube model for a network with tube radius 0.5 nm density 3 µm $µm^{-2}$ (—), tube radius 0.5 nm density 4 µm $µm^{-2}$ (—), tube radius 1.5 nm density 3 µm $µm^{-2}$ (—), tube radius 1.5 nm density 4 µm $µm^{-2}$ (—) for (a) D_{app} = 1.00 x 10^{-10} cm^2 s^{-1} and c_b = 1.25 mol dm^{-3} and (b) D = 3 x 10^{-10} cm^2 s^{-1} and c_b = 0.325 mol dm^{-3}.

Figure 3.16 shows that the experimental data (-) is now lower than that simulated for an entirely active parallel array of SWNTs. This could be due to several factors. (1) Due to the random nature of the network the parallel SWNT model of equivalent density, may not accurately predict the current density. (2) The drop cast Nafion^{TM} film may not provide uniform diffusion over the whole droplet, especially at the perimeter of the drop where the film becomes thinner, in addition to the boundary caused by the circumference of the film (figure 3.17). As a result the active areas nearest to the boundary will have hindered diffusion reducing the flux to these perimeter sites. Most importantly (3) it is also possible that the SWNTs are not uniformly active resulting in a smaller active network density than that observed topographically by AFM imaging. The chiral properties of individual SWNTs could result in different SWNT sidewalls having a different rate of ET, creating areas where ET is kinetically hindered rather than diffusion-controlled as assumed in the theoretical models. Differences in SWNT electroactivity have been observed previously using metal deposition on CVD grown SWNTs. Crucially some SWNTs were found not to support metal deposition, and display quasi-insulator properties, believed to be due to poor conductivity through the individual SWNT.[36, 37, 44, 53, 54] Thus the density, if quasi-insulating SWNTs are present, of the electrochemically active SWNT networks will be lower than measured. Hence the theoretical *i-t* values will provide an over estimate.

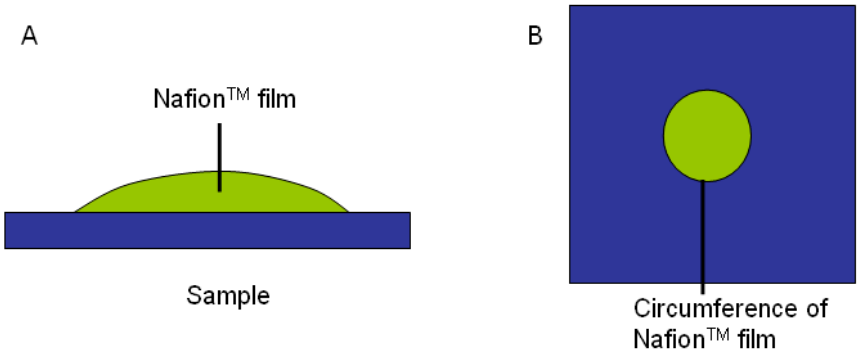

Figure 3.17 Schematic of the drop cast NafionTM film, (a) cross section through the film illustrating the film being thinner at the edges and (b) top down view highlighting the boundary at the circumference of the film.

3.5.6. Analysis of Diffusion Profiles

The results presented in sections 3.5.4 and 3.5.5 showed that the FEM simulations proposed do not fully agree with the experimentally obtained data when stepping from 0 V to the over potential (0.5 V). Figure 3.18 (a) shows that the experimental data has a current density which lies between both models for 0.1 ms $\leq t \leq$ 2 s. Importantly, the current density due to the discrete active site model underestimates the experimental response, even when using parameters that represent the maximum possible response. This indicates that there must be other contributions to the current such as the sidewall of the SWNTs. The predicted results for the entirety of the sidewall being active over estimates the current density but as noted above it is likely that not all the network is homogenously active.

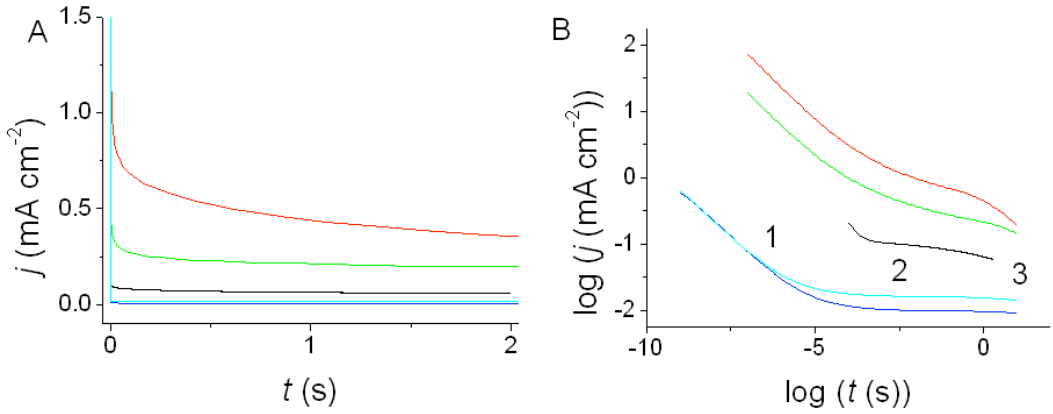

Figure 3.18 Comparison of experimental data to the extremes of both models, (—) experimental data, all active model for D = 3 x 10^{-10} cm^2 s^{-1} and c_b = 0.325 mol dm^{-3} for a tube radius 1.5 nm and network density of 4 µm $µm^{-2}$ (—),all active model for D_{app} = 1.00 x 10^{-10} cm^2 s^{-1} and c_b = 1.25 mol dm^{-3} for a tube radius 0.5 nm and network density of 3 µm $µm^{-2}$ (—), discrete active site model for D = 3 x 10^{-10} cm^2 s^{-1} and c_b = 0.325 mol dm^{-3} for defects of 0.5 nm and network density of 4 µm $µm^{-2}$ (—), and discrete active site model for D = 1 x 10^{-10} cm^2 s^{-1} and c_b = 1.25 mol dm^{-3} for defects of 0.5 nm and network density of 4 µm $µm^{-2}$ (—). In (b) 1 represents the initial linear diffusion region, 2 the developed diffusion profile and 3 the overall linear regime.

Figure 3.18 (b) shows the log j vs log t response for both theoretical models and the experimental data. The domains 1-3 refer to the developing diffusion profiles associated with the electrochemical response as presented in section 3.4.3. The changes in the gradient in the log j vs log t plot are considered for the experimental data and both theoretical models. The initial response of the SWNT experimental data (t < 1 ms) in figure 3.18 (b) shows a response similar to domain 1, where an initial linear regime is present. However the current density response is much greater than the discrete active site model, and the change in gradient occurs after a greater period of time than predicted by a 100 nm defect spacing on a neighbouring SWNT, and does not reach a plateaux. This indicates that there is a greater area of active

material present than predicted by the discrete active site model, even when a generous approximation to the size and number of defects within the network is used. After the change in gradient the current time decay is similar in profile to the parallel tube model, however the transition into domain 3 occurs earlier than predicted by the parallel SWNT model at ~0.5 s. This could be due to the experimental sample not being a uniform array, instead consisting of a random distribution of SWNTs, with some that are closer together than the average spacing and that cross each other (figure 3.11). The SWNTs that are closer together will have diffusional overlap occurring at lower values of *t* than predicted by the idealised array. However, as there are SWNTs which have a larger than average spacing on the experimental samples, the change in gradient is much more gradual as the diffusional overlap does not occur uniformly for across the network.

3.6. Conclusions

The use of drop cast Nafion^{TM} redox mediator films as a method for slowing down diffusion and thus observing electrochemistry at short diffusional length scales ($d \approx$ 10 nm) has been successfully demonstrated. The experimentally observed current upon stepping the potential from 0 to the over potential (0.5 V) is greater than predicted for isolated active sites only, even when using parameters which maximise the current response. Thus it is highly likely that the sidewalls of CNTs contribute to ET. The experimental results are lower than the *i* - *t* predictions for an all active parallel SWNT model. However, this could be due to the over simplification of the network to a uniformly spaced array of parallel tubes; heterogeneities within the drop

cast Nafion™ film and the interface between the drop cast Nafion™ and finally a heterogeneously active SWNT network due to differeing electronic properties of individual SWNTs which are not accounted for in the FEM models. These data indicate that it is highly likely that defect sites cannot be solely attributed to the electrochemical activity of SWNTs.

3.7. References

(1) Edwards, M. A.; Bertoncello, P.; Unwin, P. R. *The Journal of Physical Chemistry C* **2009**, *113*, 9218.
(2) Banks, C. E.; Compton, R. G. *Analyst* **2006**, *131*, 15.
(3) Banks, C. E.; Compton, R. G. *Analyst* **2005**, *130*, 1232.
(4) McCreery, R. L. *Chemical Reviews* **2008**, *108*, 2646.
(5) McDermott, C. A.; Kneten, K. R.; McCreery, R. L. *Journal of the Electrochemical Society* **1993**, *140*, 2593.
(6) Britto, P. J.; Santhanam, K. S. V.; Ajayan, P. M. *Bioelectrochemistry and Bioenergetics* **1996**, *41*, 121.
(7) Kim, S. N.; Rusling, J. F.; Papadimitrakopoulos, F. *Advanced Materials* **2007**, *19*, 3214.
(8) Uslu, B.; Ozkan, S. A. *Analytical Letters* **2007**, *40*, 817.
(9) Wang, J. *Electroanalysis* **2005**, *17*, 7.
(10) Svancara, I.; Vytras, K.; Kalcher, K.; Walcarius, A.; Wang, J. *Electroanalysis* **2009**, *21*, 7.
(11) Girishkumar, G.; Vinodgopal, K.; Kamat, P. V. *Journal of Physical Chemistry B* **2004**, *108*, 19960.
(12) Dumitrescu, I.; Unwin, P. R.; Wilson, N. R.; Macpherson, J. V. *Analytical Chemistry* **2008**, *80*, 3598.
(13) Dumitrescu, I.; Unwin, P. R.; Macpherson, J. V. *Chemical Communications* **2009**, *45*, 6886.
(14) Kruusma, J.; Mould, N.; Jurkschat, K.; Crossley, A.; Banks, C. E. *Electrochemistry Communications* **2007**, *9*, 2330.
(15) Gooding, J. J.; Chou, A.; Liu, J. Q.; Losic, D.; Shapter, J. G.; Hibbert, D. B. *Electrochemistry Communications* **2007**, *9*, 1677.
(16) Banks, C. E.; Davies, T. J.; Wildgoose, G. G.; Compton, R. G. *Chemical Communications* **2005**, *7*, 829.
(17) Banks, C. E.; Moore, R. R.; Davies, T. J.; Compton, R. G. *Chemical Communications* **2004**, 1804.
(18) Davies, T. J.; Moore, R. R.; Banks, C. E.; Compton, R. G. *Journal of Electroanalytical Chemistry* **2004**, *574*, 123.
(19) Kneten, K. R.; McCreery, R. L. *Analytical Chemistry* **1992**, *64*, 2518.
(20) Moore, R. R.; Banks, C. E.; Compton, R. G. *Analytical Chemistry* **2004**, *76*, 2677.

(21) Gooding, J. J.; Wibowo, R.; Liu, J. Q.; Yang, W. R.; Losic, D.; Orbons, S.; Mearns, F. J.; Shapter, J. G.; Hibbert, D. B. *Journal of the American Chemical Society* **2003**, *125*, 9006.
(22) Liu, J. Q.; Chou, A.; Rahmat, W.; Paddon-Row, M. N.; Gooding, J. J. *Electroanalysis* **2005**, *17*, 38.
(23) Heller, I.; Kong, J.; Heering, H. A.; Williams, K. A.; Lemay, S. G.; Dekker, C. *Nano Letters* **2005**, *5*, 137.
(24) Gong, K. P.; Chakrabarti, S.; Dai, L. M. *Angewandte Chemie-International Edition* **2008**, *47*, 5446.
(25) Bertoncello, P.; Edgeworth, J. P.; Macpherson, J. V.; Unwin, P. R. *Journal of the American Chemical Society* **2007**, *129*, 10982.
(26) Wilson, N. R.; Guille, M.; Dumitrescu, I.; Fernandez, V. R.; Rudd, N. C.; Williams, C. G.; Unwin, P. R.; Macpherson, J. V. *Analytical Chemistry* **2006**, *78*, 7006.
(27) Dumitrescu, I.; Wilson, N. R.; Macpherson, J. V. *The Journal of Physical Chemistry C* **2007**, *111*, 12944.
(28) Ebbesen, T. W.; Takada, T. *Carbon* **1995**, *33*, 973.
(29) Hiura, H.; Ebbesen, T. W.; Fujita, J.; Tanigaki, K.; Takada, T. *Nature* **1994**, *367*, 148.
(30) Hashimoto, A.; Suenaga, K.; Gloter, A.; Urita, K.; Iijima, S. *Nature* **2004**, *430*, 870.
(31) Collins, P. G. *Oxford Handbook of Nanoscience and Technology*; Oxford University Press: Oxford, 2009.
(32) Stone, A. J.; Wales, D. J. *Chemical Physics Letters* **1986**, *128*, 501.
(33) Ajayan, P. M.; Ravikumar, V.; Charlier, J. C. *Physical Review Letters* **1998**, *81*, 1437.
(34) Andzelm, J.; Govind, N.; Maiti, A. *Chemical Physics Letters* **2006**, *421*, 58.
(35) Bronikowski, M. J.; Willis, P. A.; Colbert, D. T.; Smith, K. A.; Smalley, R. E. *Journal of Vacuum Science & Technology a-Vacuum Surfaces and Films* **2001**, *19*, 1800.
(36) Fan, Y. W.; Goldsmith, B. R.; Collins, P. G. *Nature Materials* **2005**, *4*, 906.
(37) Day, T. M.; Unwin, P. R.; Wilson, N. R.; Macpherson, J. V. *Journal of the American Chemical Society* **2005**, *127*, 10639.
(38) Kwak, J.; Bard, A. J. *Analytical Chemistry* **1989**, *61*, 1221.
(39) Macpherson, J. V.; Unwin, P. R. *Journal of Physical Chemistry* **1994**, *98*, 11764.
(40) Davies, T. J.; Ward-Jones, S.; Banks, C. E.; del Campo, J.; Mas, R.; Munoz, F. X.; Compton, R. G. *Journal of Electroanalytical Chemistry* **2005**, *585*, 51.
(41) Davies, T. J.; Compton, R. G. *Journal of Electroanalytical Chemistry* **2005**, *585*, 63.
(42) Bard, A. J.; Faulkner, L. R. *Electrochemical Methods*, 2nd ed.; John Wiley and Sons: New York, 2001.
(43) Brett, C. M. A.; Brett, A. M. O. *Electrochemistry Principles*; Oxford Press: Oxford, 1993.
(44) Huang, S. M.; Qian, Y.; Chen, J. Y.; Cai, Q. R.; Wan, L.; Wang, S.; Hu, W. B. *Journal of the American Chemical Society* **2008**, *130*, 11860.
(45) Pyo, M.; Bard, A. J. *Electrochimica Acta* **1997**, *42*, 3077.
(46) Mirkin, M. V.; Fan, F. R. F.; Bard, A. J. *Science* **1992**, *257*, 364.
(47) Shoup, D.; Szabo, A. *Journal of Electroanalytical Chemistry* **1982**, *140*, 237.
(48) Bertoncello, P.; Ciani, I.; Li, F.; Unwin, P. R. *Langmuir* **2006**, *22*, 10380.

(49) Bertoncello, P.; Ciani, I.; Marenduzzo, D.; Unwin, P. R. *J. Phys. Chem. C* **2007**, *111*, 294.
(50) Mauritz, K. A.; Moore, R. B. *Chem. Rev.* **2004**, *104*, 4535.
(51) Ugo, P.; Moretto, L. M.; Bellomi, S.; Menon, V. P.; Martin, C. R. *Analytical Chemistry* **1996**, *68*, 4160.
(52) Ugo, P.; Moretto, L. M.; Vezza, F. *Chemphyschem* **2002**, *3*, 917.
(53) Wilson, N. R.; Cobden, D. H. *Nano Letters* **2008**, *8*, 2161.
(54) Chen, Y.-C.; Young, R. J.; Macpherson, J. V.; Wilson, N. R. *The Journal of Physical Chemistry C* **2007**, *111*, 16167.
(55) Porro, S.; Musso, S.; Vinante, M.; Vanzetti, L.; Anderle, M.; Trotta, F.; Tagliaferro, A. *Physica E: Low-dimensional Systems and Nanostructures* **2007**, *37*, 58.

4. Design and Verification of Channel Flow Electrodes by Microstereo Lithography

4.1. Introduction

The development of a channel flow cell using microstereo lithography (MSL) that provides well-defined hydrodynamics to an electrode surface is demonstrated within this chapter. The MSL-fabricated channel flow cell is simply mounted onto the electrode by binding with thread, removing the need for adhesives or high mechanical forces. Importantly the MSL produced channels are not distorted during assembly, unlike conventional channel flow cells, hence removing the need for electrochemical calibration, which has not been achieved before using conventional channel flow experiments. With this simple method of assembly flow rates up 64 mL min^{-1} can be obtained. The design is successfully applied to gold and polycrystalline boron doped diamond (pBDD) band electrodes, providing an electrochemical response in agreement with the Levich equation for band geometries under Laminar channel flow conditions. FEM is also used to accurately predict the limiting current response for the situation where the electrode dimensions are governed by the entire channel base.

4.2. Channel Flow Construction Methods

Most practical channel flow designs consist of either a two-part or three-part assembly.[1-14] In the latter case (which is common), the parts are: (i) an electrode either embedded in the bottom face of the channel or glued to it; (ii) a spacer, the

thickness of which defines the channel height (which typically distorts under pressure); and (iii) a top layer, which typically includes the flow inlet and outlet pipes, as illustrated in figure 4.1 (a). Figure 4.1 (b) shows an example of this type of cell which is held together by mechanically applied pressure (*e.g.* the use of nuts and bolts).[1-14]

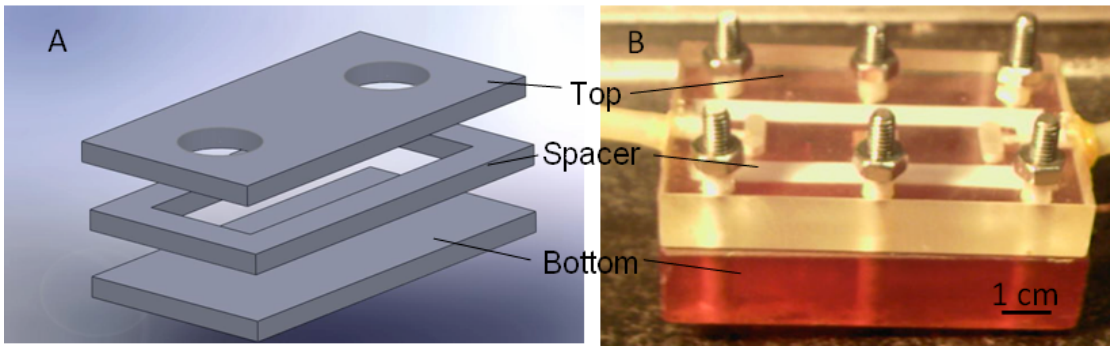

Figure 4.1 (a) Schematic of a three part flow cell design and (b) example of a 3 part flow cell held together by screws, where the red block houses the working electrode, the white section is the spacer and the clear upper block houses the inlet and outlet connections.

In the two-part cell, the channel unit contains the duct, consisting of the 4 side walls and roof, and this is assembled onto the substrate containing the electrode using a hard-setting wax,[15, 16] or a high external pressure (figure 4.2).[17, 18] With both arrangements the channel length is often 4 cm or more, the electrode length, x_e, is in the range 20 μm – 4 mm; the channel width, w_{ch}, ~ 6 mm - 10 mm and the total channel height, $2h$, ~ 0.4 mm - 1 mm. Typical volume flow rates, V_f, of 0.0001 – 0.1 $cm^3\ s^{-1}$ are usually applied.[1-14]

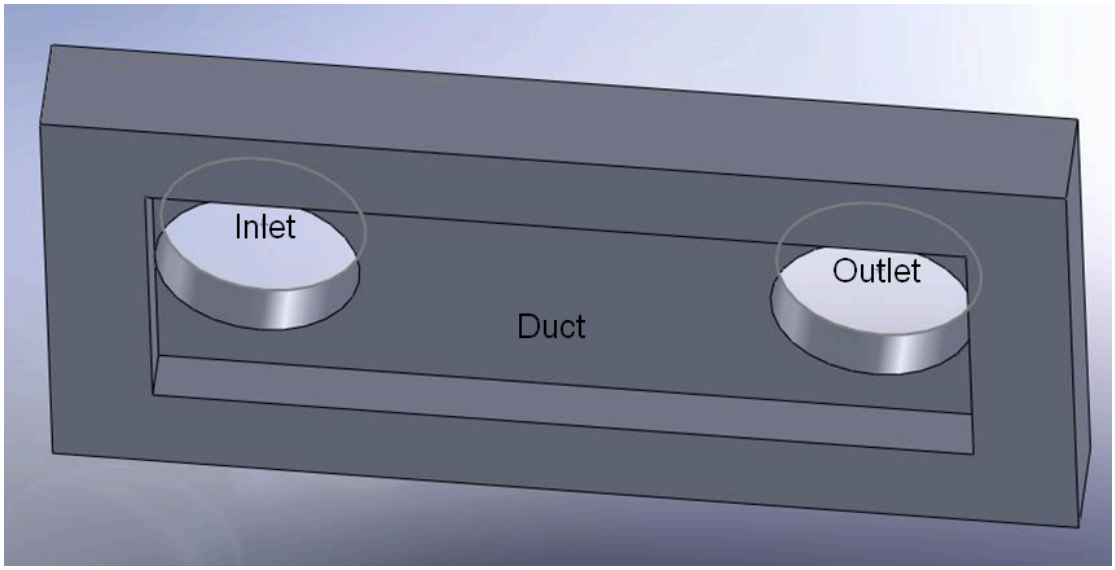

Figure 4.2 Schematic of the main body of a 2 part channel housing the inlet, outlet and duct which defines the channel dimensions. The two-part design is fixed to a planar substrate (not shwon).

The three-part cell is the most commonly adopted channel flow with electrochemical detection system, the two-part cell design tends to be adopted when using higher flow rates. For example, a fused-silica channel has been employed which is secured to a cover plate, incorporating the WE, by the use of significant external pressure.[17, 18] Though highly effective for analysis at high volume flow rates, the cell is made from silica, which is fragile, and assembly of the channel requires a high pressure chamber, which may limit possible electrode materials. Finally the cell is more expensive to set up and operate than conventional channel flow designs.

Presently, channel flow cells are made either by hand, which is time consuming and expensive, or from a mould, where one is limited to the dimensions of available moulds.[1-14] In addition, few channel flow cells can be used with high flow rates, unless the specialised set-up, discussed earlier, is employed.[17] Moreover, in all conventional cells, the application of mechanical pressure (screws) to close the cell results in compression of the channel spacer changing the height and width of the

channel. This makes quantitative electrochemical measurements possible only after a calibration experiment has been performed each time the cell is assembled, which is time-consuming.[1-14] Additionally, the use of an adhesive, such as wax, to secure the channel assembly, creates a brittle seal that may be prone to leaking and, again, creates uncertainties in the cell dimensions.[1-14]

This chapter describes a new methodology for the construction of a channel flow cell for electrochemical detection, which overcomes the issues highlighted and also significantly shrinks the dimensions of the cell, without impairing the inherently well-defined mass transport. Furthermore, the approach described allows the application of a wide range of flow rates and is versatile in terms of the material used for the substrate and the geometries of the electrodes employed.

4.3. Experimental

4.3.1. Channel Design

The design of the channel was based upon the two-part cell approach, where a flow cell consisting of the inlet, outlet and 5 walls of the channel, is assembled on top of the working electrode, mounted within a planar substrate. For the channel flow cell to provide well defined hydrodynamics, and for the current response to be predicted by theoretical calculations the internal dimensions of the channel must be known accurately. Of particular importance are the height ($2h$) and width of the channel (w_{ch}), and the electrode dimensions (x_E and w_E). To facilitate the use of the flow cell with a wide range of electrode materials the device has to be customisable, easy to assemble and not require electrochemical calibration of the height once assembled.

For these reasons MSL was employed for the construction of the channel flow cell units.

The design for the channel flow cell is shown in figure 4.3, where solution impinges from the inlet onto the planar substrate before flowing through a well defined channel of $2h$ = 200 μm and w_{ch} = 3 mm. The standard MSL construction process described in section 2.4 was used to produce the channel flow unit. In one MSL batch run, which takes ~8 hours, 4 channel flow units could be produced. After production the height of each channel was measured by white light interferometry and used for all calculations related to experiments within the channel.

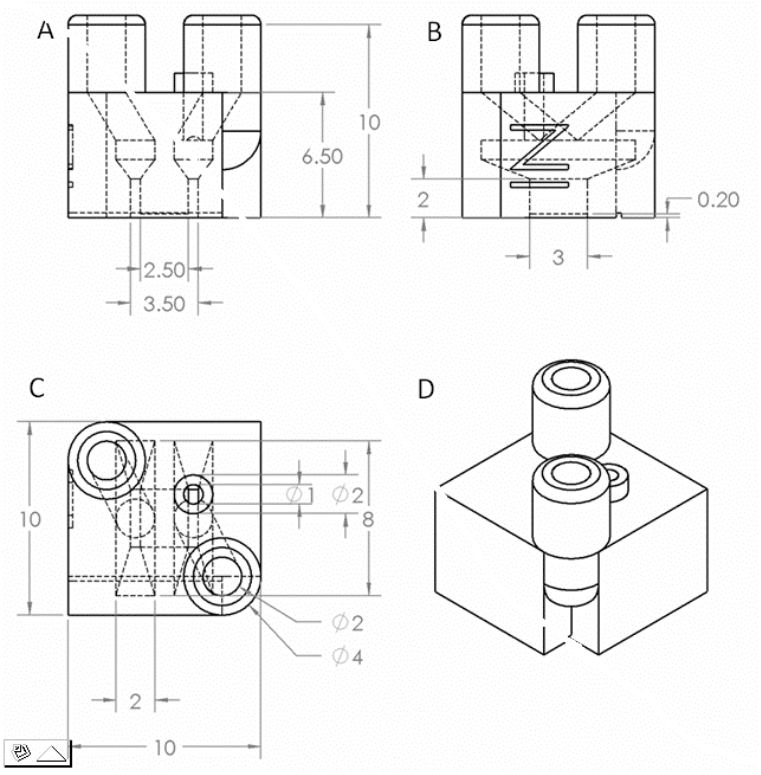

Figure 4.3 The design of channel flow cell where (a) is the view along the length of the channel, (b) the width of the channel, (c) view from above the channel, and (d) isometric view of the exterior of the channel. All measurements are in mm

4.3.2. Electrode Fabrication

Three different working electrodes were employed to characterise mass transport in this new type of flow cell: (a) a macroscopic gold (Au) substrate, where the resulting electrode area was governed by the dimensions of the entire bottom face of the channel, *i.e.* 3.5 mm x 3 mm; (b) a lithographically-defined Au band electrode, with w defined by the width of the channel (w = 3 mm) and x_e = 680 μm; and (c) a polycrystalline boron doped diamond (pBDD) band embedded within insulating epoxy resin and polished flat. For both (a) and (b), Au (120 nm thick) was thermally evaporated (with a 10 nm thick Cr adhesion layer) onto Si/SiO_2 wafers (IDB Technologies Ltd.) cut to ~1 cm x 1 cm. The Au band was created by shadow masking the Si/SiO_2 wafer during evaporation and the resulting dimensions were measured optically (Olympus BH2 microscope). The electrode surface was cleaned between experiments with ultra pure Milli-Q water (Millipore Corp.), and then blown dry with nitrogen.

For electrode (c), the pBDD band of the desired dimensions (x_e = 200 μm and $w \approx$ 2.0 mm) was cut using laser micromachining (Oxford Lasers), from a larger 500 μm thick pBDD sample, which had been polished on one side (electrode surface) to ~2 nm roughness (Element Six Ltd. Ascot, UK).[19] The boron dopant density of this material was ca. 5×10^{20} atoms cm^{-3}. The pBDD band was cleaned in boiling H_2SO_4 (98%) supersaturated with KNO_3[20] and electrically contacted by sputtering a gold contact with a titanium adhesion layer onto the back of the diamond (non-polished face). Tinned copper wire was attached to this surface using silver dag paint (Agar). The pBDD band was sealed in insulating epoxy resin (Delta Resins) using a cylindrically-shaped Teflon mould. After curing, the encapsulated electrode was

removed from the mould and polished flat to expose the pBDD surface, using silicon carbide polishing pads (Buehler) and 0.05 μm alumina paste (Buehler).

4.3.3. Flow System and Cell Assembly

The channel flow unit was assembled on the electrode surface of interest simply by binding the flow cell and electrode substrate together with a cotton thread. Figure 4.4 shows a typical channel flow cell and how the flow cell was assembled onto the electrode. Inlet and outlet tubing (PVC 1/8" inner diameter and 1/4" outer diameter) were connected directly to the cell by push-fitting, and connections to a flow pump made using Omni-fit adapters (Bio-Chem Fluidics). One of two different pumps was employed to control flow through the cell, either: (i) a syringe pump (KD Scientific), equipped with a 50 mL Hamilton syringe with a 32.57 mm bore (maximum volume flow rate (V_f) of 64 ml min^{-1}); or (ii) a single piston liquid chromatography pump (Gilson 305) fed through a manometric module (Gilson 806) to maintain a constant volume flow rate, maximum V_f = 25 ml min^{-1}.

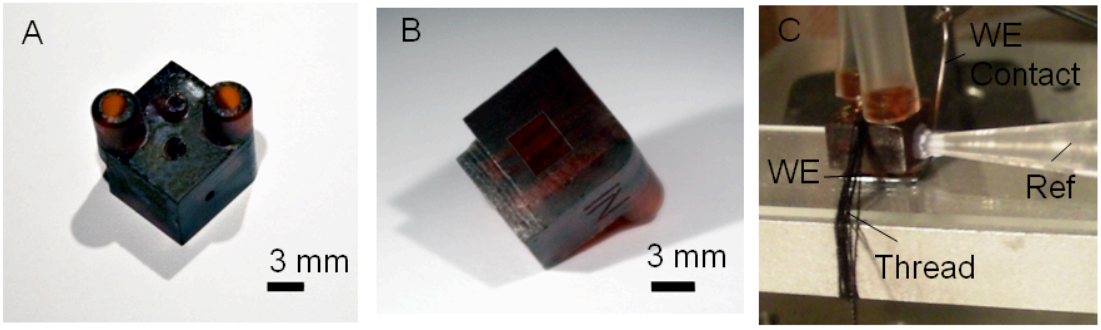

Figure 4.4 Photographs of a typical channel flow cell, (a) top view, (b) bottom view and (c) assembled onto the electrode

4.3.4. Electrochemical Measurements

All electrochemical measurements were carried out in the two-electrode mode with a WE and a quasi-reference electrode. The system could easily incorporate a three-electrode dynamic electrochemical set-up if required. The quasi-reference electrode was a silver wire coated in silver chloride. Note that as voltammetric measurements were made over a relatively wide potential range, a true limiting current could always be determined. Solutions containing 0.1 mM ferrocenylmethyl trimethylammonium ($FcTMA^+$) hexaflorophosphate (synthesised in house[21]) in 0.1 M KNO_3 supporting electrolyte (99% Fischer Scientific) were used for all experiments. Linear sweep voltammograms were recorded using either a CHI760C bipotentiostat (CH Instruments) or an Autolab electrochemical workstation (Eco Chemie), typically at a scan rate of 10 mV s^{-1}.

4.4. Theoretical Testing

The channel design shown in figure 4.3 was theoretically tested to ensure that the device would operate under laminar flow conditions and provide a response in agreement with the Levich equation.

To determine if the flow through the channel would be laminar, the Reynolds number was calculated for the highest experimental flow rate (64 mL min^{-1}) using the equation 1.21. The Reynolds number at this flow rate for the channel is 1350, hence flow is laminar, for all practically obtainable volume flow rates (*e.g.* up to 64 mL min^{-1}). This indicates that the channel will provide well defined hydrodynamics to the

electrode surface. The velocity profile within the channel and limiting current responses for each of the electrodes was determined by the use of FEM.

A desktop computer equipped with an Intel Pentium III Xeon quad core 2.5 GHz processor and 8 GB of RAM running Windows XP Professional 64 bit was used for all of the FEM simulations. These were performed using the commercial FEM package Comsol Multiphysics 3.5a (Comsol AB, Sweden), using the Matlab interface (Release 2009a) (MathWorks^{TM} Inc., Cambridge, UK). This approach has previously proven powerful for investigating complex hydrodynamic electrode systems.[22, 23] The channel was approximated to a 2D cross-section, along the direction of x_e, making the assumption that channel and electrode edge effects in the direction of w are negligible (figure 1.12(b)). Such an approach has been adopted in previous treatments of mass transport to channel electrodes.[15, 24-30]

4.4.1. FEM of Convection Within the Channel Flow Cell

Initially, the velocity profile within the 2D channel cross-section, figure 4.5, was determined by solving the incompressible Navier-Stokes equations for momentum balance (equation 4.1) and continuity (equation 4.2).

$$\rho \mathbf{V} \cdot \nabla \mathbf{V} = -\nabla (p + \eta (\nabla \mathbf{V} + (\nabla \mathbf{V})^T)) \quad \textbf{(4.1)}$$

$$\nabla \cdot \mathbf{V} = 0 \quad \textbf{(4.2)}$$

where ρ is the density of water (assumed reasonably to be 1.00 g cm^{-3}),[31] $\mathbf{V}$ is the velocity vector (with components u and v in the x and y directions, respectively), p is pressure, η is the dynamic viscosity of water, which is reasonably 1.00 mPa s for the

experimental conditions used herein, and T is the matrix transpose operator. Figure 4.5 shows the 2D cross section used in the FEM simulation and defines the boundary labelling conventions employed. The following boundary conditions were used for the finite element calculations (equation 4.3 – equation 4.5)

Boundaries 1, 3 to 8, and 10: $u = 0,\ v = 0$ **(4.3)**

Boundary 2: $u = 0,\ v = -\frac{V_f}{w_{ch} x_{ch}}$ **(4.4)**

Boundary 9: $p = p_0,\ \eta(\nabla \mathbf{V} + (\nabla \mathbf{V})^T)\mathbf{n} = 0$ **(4.5)**

where w_{ch} and x_{ch} are the channel width (in this case 3 mm in the w direction) and principal inlet dimensions (length of boundary 2, 0.5 mm), respectively, p_0 is the pressure of the system, and **n** is the vector normal to a particular boundary. Boundaries 1, 3 to 8, and 10 represent the walls of the flow cell, substrate and electrode, and consequently have a no slip boundary condition (equation 4.3). Flow is introduced to the channel normal to the inlet, boundary 2, as described in equation 4.4, with the outlet, boundary 9, being set to standard pressure with no shear stress exerted upon the fluid exiting the cell (equation 4.5). The inlet and outlet heights of 2 mm were chosen to ensure that Poiseuille flow had developed, in the inlet section to the main channel and to ensure that the outlet did not distort flow at the extreme downstream section of the main channel.

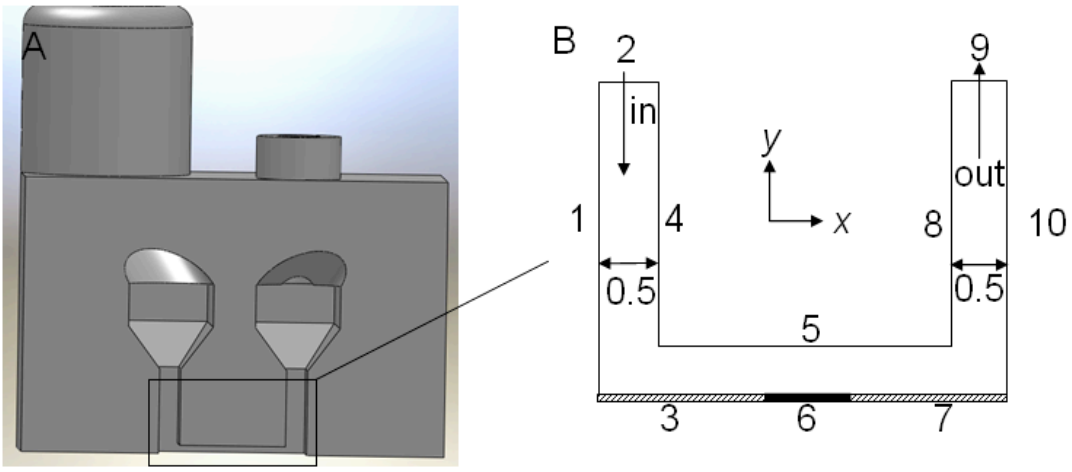

Figure 4.5 (a) View of the channel flow cell design highlighting the section taken for the FEM domain (b) 2D cross section showing the numbering convention for the FEM of the channel

4.4.2. FEM Convection and Diffusion Simulations

After determining the velocity distribution at a particular value of V_f, the local values of u and v were used in the solution of the steady-state convection-diffusion equation for transport-controlled electrolysis at the channel electrode to evaluate the mass-transport limited current response and predict the concentration distributions:

$$\nabla(-D\nabla c) = -\mathbf{V}\nabla c \qquad \textbf{Equation 4.1}$$

where D is the diffusion coefficient (6 x 10^{-6} mol dm^{-3} for $FcTMA^+$)[32] and c the concentration of $FcTMA^+$.

The boundary conditions for the convection and diffusion model are shown in Table 1. Boundaries 1, 3 to 5, 7, 8, and 10 for the band electrodes and boundaries 1, 4, 5, 8 and 10 for the case where the electrode is defined by the area of the channel,

are the insulating walls of the channel and substrate. Boundary 2 is the inlet where fresh solution enters at the bulk concentration, boundary 6 (or boundaries 3, 6 and 7 where the channel defines the entire electrode area) is the electrode surface where complete and instantaneous electrolysis of the analyte occurs and boundary 9 is the outlet where the flux normal to the boundary is solely due to convection. This is reasonable for the cell dimensions and flow velocities of interest.

Boundary	Navier-Stokes	Convection-Diffusion	
		Band electrode	Channel defined electrode
1	No slip	Insulation ($\mathbf{n} \cdot \mathbf{N} = 0$)	Insulation ($\mathbf{n} \cdot \mathbf{N} = 0$)
2	Inlet	Inlet ($c = c_b$)	Inlet ($c = c_b$)
3	No slip	Insulation ($\mathbf{n} \cdot \mathbf{N} = 0$)	Electrode ($c = 0$)
4	No slip	Insulation ($\mathbf{n} \cdot \mathbf{N} = 0$)	Insulation ($\mathbf{n} \cdot \mathbf{N} = 0$)
5	No slip	Insulation ($\mathbf{n} \cdot \mathbf{N} = 0$)	Insulation ($\mathbf{n} \cdot \mathbf{N} = 0$)
6	No slip	Electrode ($c = 0$)	Electrode ($c = 0$)
7	No slip	Insulation ($\mathbf{n} \cdot \mathbf{N} = 0$)	Electrode ($c = 0$)
8	No slip	Insulation ($\mathbf{n} \cdot \mathbf{N} = 0$)	Insulation ($\mathbf{n} \cdot \mathbf{N} = 0$)
9	Outlet	Outlet ($\mathbf{n}(-D\nabla c) = 0$)	Outlet ($\mathbf{n}(-D\nabla c) = 0$)
10	No slip	Insulation ($\mathbf{n} \cdot \mathbf{N} = 0$)	Insulation ($\mathbf{n} \cdot \mathbf{N} = 0$)

Table 1 Summary of the boundary conditions used in the simulation of the limiting current response for the channel electrode, where no slip refers to equation 4.3, inlet refers toequation 4.4, and outlet refers to equation 4.5 for the Navier-Stokes simulation, and where where N is the inward flux, and c_b is the bulk concentration of $FcTMA^+$ (0.1 mmol dm^{-3}) for the convection and diffusion calculations.

The limiting current (i_{lim} (A)) response was calculated by summing the flux at boundary 6 (or boundaries 3, 6 and 7 for the situation where the electrode is defined by the channel area) and multiplying by the electrode width (w_e), n, the number of electrons transferred per redox event, and F, Faraday's constant (96485 C mol^{-1}).

4.5. Results and Discussion

4.5.1. Insights from Simulation

All three electrode geometries were simulated to determine flow through the channel at rates between 0.1 - 64 mL min^{-1}. The most stringent test is the highest flow rate, giving the longest lead-in length for the development of Poiseuille flow.[33] Figure 4.6 (a) shows that for this case, after a very short lead in length, with respect to the top face of the channel, a steady Poiseuille velocity profile is achieved down the channel. This is a consequence of the channel design, where a rectangular section (faces 1 and 4) feeds solution into the main part of the channel cell.

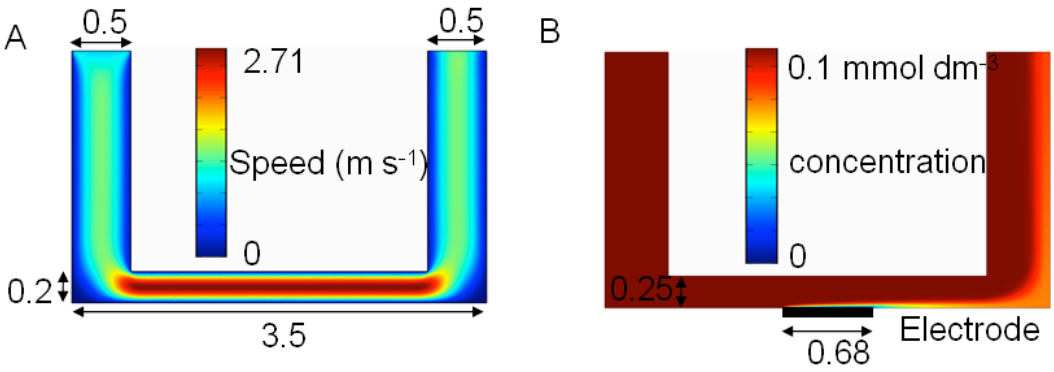

Figure 4.6 (a) Velocity profile in the channel cell for V_f = 64 mL min^{-1}, showing that flow within the channel is laminar. The concentration profiles resulting for transport-controlled electrolysis of a reactant at a band electrode (x_e = 680 µm, $2h$ = 250 µm, V_f = 64 mL min^{-1}) (b) (V_f = 0.1 mL min^{-1}). (All measurements in mm).

Figure 4.6 (b) shows the typical concentration profile for the situation where a band electrode is situated in the bottom face of the channel at the midpoint. It can be seen that the concentration boundary layer in the vicinity of the electrode is confined close to the wall, and consequently one would expect the Levich equation to hold. That this is the case can be seen by comparing the simulated steady-state current response (▲) and that predicted by the Levich equation (——) which are in excellent agreement, (figure 4.7 (a) and (b)), over the volume flow rate range, 0.1 to 64 ml min^{-1}. The electrode dimensions and flow cell heights used to produce figure 4.7 (a) and figure 4.7 (b) (x_e = 680 µm, w_{ch} = w_e = 3 mm, and $2h$ = 250 µm for the Au electrode, x_e = 200 µm, w = 2 mm, w_{ch} = 3 mm, and $2h$ = 192 µm for the pBDD electrode) are those that were used experimentally for the Au band and pBDD band flow cell electrochemical experiments (*vide infra*).

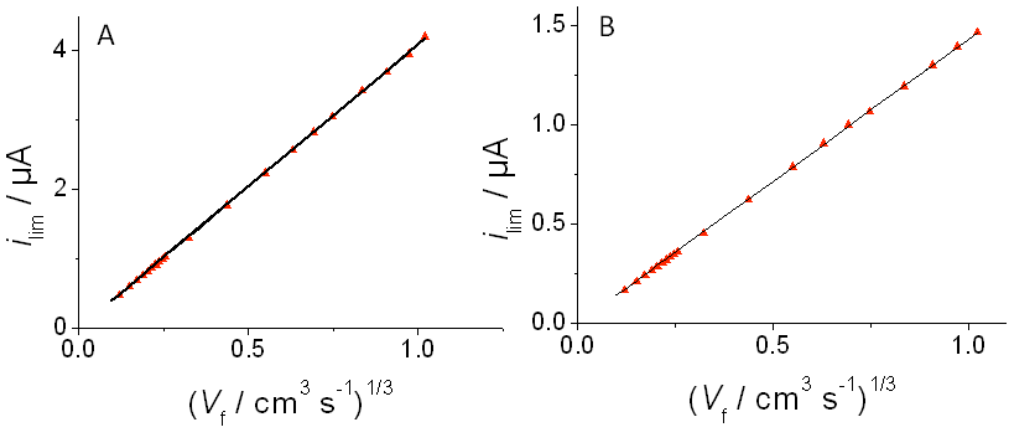

Figure 4.7 Comparison of the limiting steady-state current response predicted by the finite element model (▲) and the Levich equation (solid black line) for D = 6 x 10^{-6} cm^2 s^{-1}, c_b = 1 x 10^{-4} mol dm^{-3}; (a) a band with x_e = 680 μm w_e = 3 mm and 2h = 250 μm, over the V_f range 0.1 to 64 mL min^{-1}; (b) a band with x_e = 200, μm w_e = 2 mm and 2h = 192 μm, over the V_f range 0.1 to 64 mL min^{-1}.

For the case where the bottom face of the cell defines the entire electrode, the simulated response (▲; figure 4.8 (a)) has an approximate $V_f^{1/3}$ dependence, but the measured currents are slightly lower than predicted by the Levich equation (——; figure 4.8 (a)). This is because convective effects at the extreme upstream and downstream edges of the flow channel are diminished, giving rise to lower mass transport rates and thus a smaller transport-limited current density, than for an electrode positioned in the Poiseuille flow regime. Such effects are evident in the simulated concentration profiles, for example in figure 4.8 (b) where one can see an increased concentration boundary layer thickness at the upstream and downstream edges of the macroscopic electrode (reflecting a lower mass transport rate), compared to the characteristic concentration boundary layer which scales as $x^{-2/3}$ for an electrode in Poiseuille flow. [1-14] Nonetheless, the effect is actually rather small, and as shown later such electrodes can be treated in a highly quantitative fashion.

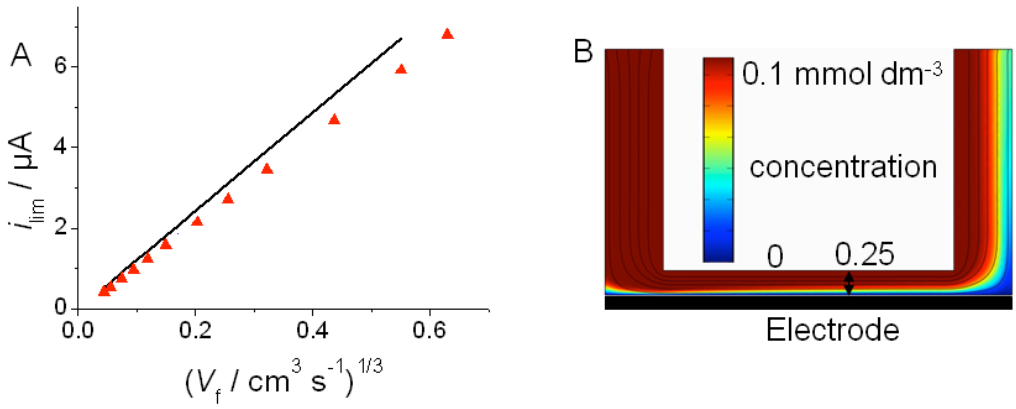

Figure 4.8 (a) Diffusion profile for the transport controlled electrolysis of a species where the entire base of the channel is active (V_f = 0.1 mL min^{-1}), (b) comparison of the FEM limiting current to the Levich predicted response for the entire base of the channel being active the entire channel floor as the electrode *i.e.* x_e = 3.5 mm, w = 3 mm and 2h = 250 μm, over the V_f range 0.1 to 25 mL min^{-1}.

4.5.2. Experimental Investigation of Channel Flow Cells

To verify mass transport to the channel flow electrode, measurements were first carried out with the Au and pBDD band electrodes defined earlier. These electrodes, were located sufficiently downstream of the channel entrance (electrode leading edge from wall 1, ~1.7 mm and ~2 mm for the Au and pBDD bands, respectively) to ensure that Poiseuille flow had been established. Figure 4.9 shows: (a) typical LSVs for the one-electron oxidation of 0.1 mM $FcTMA^+$ in 0.1 M KNO_3, at the Au band electrode, at a scan rate of 10 mV s^{-1}, over the V_f range 0.03 – 64 ml min^{-1}; and (b) a plot of experimental i_{lim} (•) versus that predicted by the Levich theory (solid black line) for x_e = 680 μm, w = 3 mm, 2h = 250 μm and D = 6.0 x 10^{-6} cm^2 s^{-1} for $FcTMA^+$.[32]

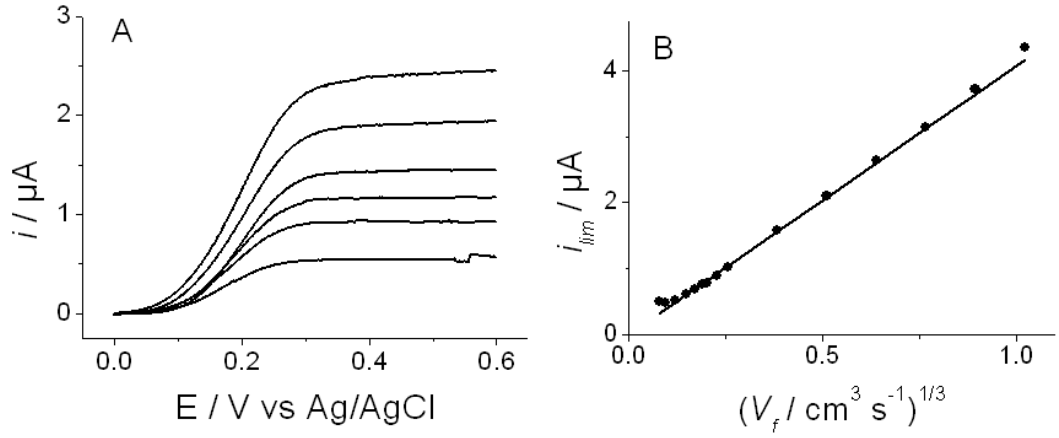

Figure 4.9 (a) Typical LSVs for the oxidation of 0.1 mM $FcTMA^+$ in 0.1 M KNO_3 at a Au band channel electrode (w = 3 mm, x_e = 680 μm, $2h$ = 250 μm) at 10 mV s^{-1} at V_f values of 0.03 (lowest current), 0.2, 0.5, 1.0, 3.4, 8.0 (highest current) ml min^{-1}. (b) Comparison of the experimentally obtained i_{lim} (●) to the Levich equation (solid black line).

As can be seen in figure 4.9 (b) there is an excellent correlation between the experimentally measured limiting current values and those predicted by the Levich equation, up to V_f values of 64 ml min^{-1} (also expected based on the finite element simulations above). It is important to note that, even under these high volume flow rate conditions the cell did not leak and could be assembled very easily in the simple way described. These experimental data fully support the theoretical simulations shown in figure 4.6 (a and b) and figure 4.7 (a). Note that the value of $2h$ (250 μm) used for the simulations indicates that the method adopted to bind the cell to the underlying substrate electrode does not distort the channel dimensions. This was found to be the case for all cells employed (*vide infra*, *e.g.* figure 4.10) and means that once h has been defined quickly by interferometry, the channel can be used further without the need for re-calibration of cell dimensions after cell assembly.

Figure 4.10 (a) shows typical LSVs for the one-electron oxidation of 0.1 mM $FcTMA^+$ in 0.1 M KNO_3, at a pBDD band electrode defined by w = 2 mm and x_e = 200 μm, over the V_f range 0.1 – 10 ml min^{-1} at a scan rate of 10 mV s^{-1} and (b) a plot of experimental i_{lim} (●) versus that predicted by the Levich theory (solid black line) for the electrode dimensions defined, $2h$ = 192 μm (measured by interferometry) and D = 6.0 x 10^{-6} cm^2 s^{-1}. The plot of i_{lim} vs $V_f^{1/3}$ is linear and again supports the hypothesis that mass transport in the channel is very well-defined and the limiting current can be quantified using the Levich equation. These results also show the ease at which the substrate electrode can be interchanged; enabling the easy use of a wide range of electrode materials with this flow cell configuration.

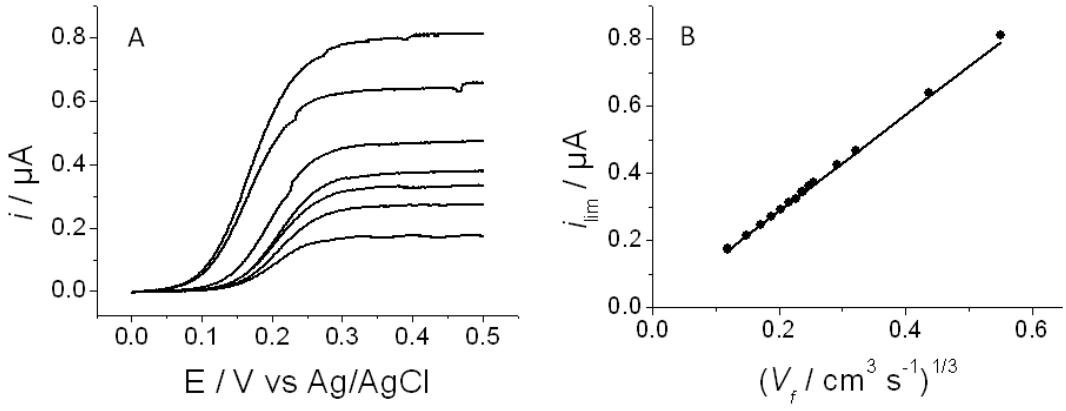

Figure 4.10 (a) Typical LSVs for the oxidation of 0.1 mM $FcTMA^+$ in 0.1 M KNO_3 at a pBDD channel band electrode (w = 2 mm, x_e = 200 μm and $2h$ = 192 μm) at 10 mV s^{-1} at V_f values of 0.1 (lowest current), 0.4, 0.7, 1.0, 2.0, 5.0, 10.0 (highest current) ml min^{-1}. (b) Comparison of the experimentally obtained i_{lim} (●) to the Levich equation (solid black line).

We finally consider experiments where the electrode area was defined by the area of the channel base in the flow cell *i.e.* w = 3 mm and x_e = 3.5 mm. Here, the solution moving through the inlet pipe effectively impinges directly onto the upstream

edge of the electrode surface and then flows down the channel, soon establishing a Poiseuille profile (figure 4.6 (a)). This case is important in connection with the present flow cell device as there may be electrode materials that cannot be readily encapsulated in a support and where one would simply wish to attach a flow cell in the simple and effective manner that we have developed herein.

Figure 4.11 (a) shows typical LSV responses for the oxidation of 0.1 mM $FcTMA^+$ in 0.1 M KNO_3 at 10 mV s^{-1} at the larger Au electrode, over the V_f range 0.005 mL min^{-1} - 10 mL min^{-1}, using the same flow cell as employed for the experiments in Figure 4 *i.e.* $2h$ = 250 μm. The steady-state limiting current at the electrode is in excellent agreement with the response predicted by the finite element simulations (figure 4.11 (b)). The response is lower than predicted by the Levich theory, for the reasons described above (figure 4.8 (a)), but critically, the response is quantitative and can be accurately modelled. These data provide further evidence that the channel flow cell is not distorted on assembly and provides well-defined, predictable mass transport to the substrate electrode.

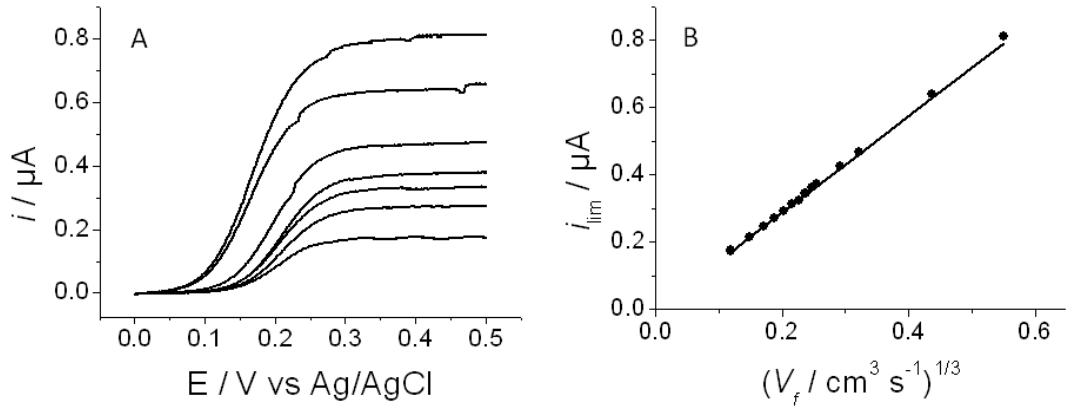

Figure 4.11 Typical LSVs for the oxidation of 0.1 mM $FcTMA^+$ in 0.1 M KNO_3 at a channel flow cell Au electrode (area defined by the bottom face of the channel, w = 3 mm, x_e = 3.5 mm and $2h$ = 250 μm) at 10 mV s^{-1} at V_f values of 0.005 (lowest current), 0.025, 0.2, 0.5, 1.0, 2.0, 10.0 (highest current) ml min^{-1} and (b) comparison of the experimentally obtained i_{lim} (●) to the predicted response by the finite element model (solid black line).

4.6. Conclusions

We have shown that MSL can be used very effectively to produce channel flow units that enable channel flow cells to be rapidly assembled for electrochemical detection under hydrodynamic control. A considerable practical attribute of these cells is that they do not require high mechanical forces *e.g.* screws or an adhesive seal. The flow cell sits atop a planar substrate, which contains the working electrode; the two are held together simply using a cotton thread that is sufficient even when working at volume flow rates as high as 64 ml min^{-1}. The flow cell can be rapidly assembled or dismantled, allowing working, counter and reference electrodes to be removed and replaced easily.

Four flow cells can typically be produced in a 6-8 hour run by MSL, and once the channel height has been independently verified, the flow cell is ready to use without further calibration. Crucially we have shown that the channel height remains unchanged after assembly *i.e.* the polymeric material does not distort, allowing the cell to be assembled/disassembled repeatedly and rapidly *e.g.* in order to clean the working electrode without fear of altering the channel dimensions between measurements. The production process also lends itself to the easy redesign of the cell for different applications. For example, current work involves the fabrication of channel cells with mixing chambers incorporated within the design. All of these attributes should lead to the greater use of channel flow electrodes in kinetic and analytical applications.

The channel flow electrode is characterised by well-defined mass transport; data for the diffusion-limited oxidation of $FcTMA^+$ demonstrated an excellent agreement with the Levich equation and finite element simulations for band electrodes. This was found to hold for a wide range of volume flow rates, up to 64 ml min^{-1} and was demonstrated herein using both Au and pBDD band electrodes. For electrodes where the active area is defined by the whole area of the channel *i.e.* 3 mm x 3.5 mm (for the flow cell designs employed here), the steady-state current response can be predicted accurately using FEM. This bodes well for further applications of the flow cell and variants thereof as demonstrated in the following chapters on low concentration detection and by application of MSL to create a wall jet electrode.

4.7. References

(1) Compton, R. G.; Unwin, P. R. *Journal of Electroanalytical Chemistry* **1986**, *205*, 1.
(2) Unwin, P. R.; Compton, R. G. In *Comprehensive Chemical Kinetics*; Compton, R. G., Hamnett, A., Eds.; Elsevier, 1989; Vol. 29, pp 173.
(3) Orton, R.; Unwin, P. R. *Journal of the Chemical Society-Faraday Transactions* **1993**, *89*, 3947.
(4) Rosset, E.; Datta, M.; Landolt, D. *Journal of Applied Electrochemistry* **1990**, *20*, 69.
(5) Compton, R. G.; Sanders, G. H. W. *Journal of Colloid and Interface Science* **1993**, *158*, 439.
(6) Unwin, P. R.; Barwise, A. J.; Compton, R. G. *Journal of Colloid and Interface Science* **1989**, *128*, 208.
(7) Thompson, M.; Wilkins, S. J.; Compton, R. G.; Viles, H. A. *Journal of Colloid and Interface Science* **2003**, *259*, 338.
(8) Compton, R. G.; Stearn, G. M.; Unwin, P. R.; Barwise, A. J. *Journal of Applied Electrochemistry* **1988**, *18*, 657.
(9) Barwise, A. J.; Compton, R. G.; Unwin, P. R. *Journal of the Chemical Society-Faraday Transactions* **1990**, *86*, 137.
(10) Tsuru, T. *Materials Science and Engineering a-Structural Materials Properties Microstructure and Processing* **1991**, *146*, 1.
(11) Compton, R. G.; Unwin, P. R. *Philosophical Transactions of the Royal Society of London Series a-Mathematical Physical and Engineering Sciences* **1990**, *330*, 1.
(12) Ahmed, S.; Fonseca, S. M.; Kemp, T. J.; Unwin, P. R. *Journal of Physical Chemistry B* **2003**, *107*, 5892.
(13) Ahmed, S.; Kemp, T. J.; Unwin, P. R. *Journal of Photochemistry and Photobiology a-Chemistry* **2001**, *141*, 69.
(14) Cooper, J. A.; Compton, R. G. *Electroanalysis* **1998**, *10*, 141.
(15) Henley, I. E.; Fisher, A. C. *Journal of Physical Chemistry B* **2003**, *107*, 6579.
(16) Yunus, K.; Fisher, A. C. *Electroanalysis* **2003**, *15*, 1782.
(17) Rees, N. V.; Dryfe, R. A. W.; Cooper, J. A.; Coles, B. A.; Compton, R. G.; Davies, S. G.; McCarthy, T. D. *Journal of Physical Chemistry* **1995**, *99*, 7096.
(18) Rees, N. V.; Alden, J. A.; Dryfe, R. A. W.; Coles, B. A.; Compton, R. G. *The Journal of Physical Chemistry* **1995**, *99*, 14813.
(19) Wilson, N. R.; Clewes, S. L.; Newton, M. E.; Unwin, P. R.; Macpherson, J. V. *The Journal of Physical Chemistry B* **2006**, *110*, 5639.
(20) Hutton, L.; Newton, M. E.; Unwin, P. R.; Macpherson, J. V. *Analytical Chemistry* **2009**, *81*, 1023.
(21) Bertoncello, P.; Ciani, I.; Marenduzzo, D.; Unwin, P. R. *J. Phys. Chem. C* **2007**, *111*, 294.
(22) Compton, R. G.; Fisher, A. C.; Latham, M. H.; Brett, C. M. A.; Brett, A. *Journal of Physical Chemistry* **1992**, *96*, 8363.
(23) Bitziou, E.; Rudd, N. C.; Unwin, P. R. *Journal of Electroanalytical Chemistry* **2007**, *602*, 263.

(24) Tam, K. Y.; Wang, R. L.; Lee, C. W.; Compton, R. G. *Electroanalysis* **1997**, *9*, 219.
(25) Bianchi, F.; Ferrigno, A.; Girault, H. H. *Analytical Chemistry* **2000**, *72*, 1987.
(26) Amatore, C.; Da Mota, N.; Lemmer, C.; Pebay, C.; Sella, C.; Thouin, L. *Analytical Chemistry* **2008**, *80*, 9483.
(27) Wain, A. J.; Compton, R. G.; Le Roux, R.; Matthews, S.; Fisher, A. C. *Analytical Chemistry* **2007**, *79*, 1865.
(28) Compton, R. G.; Pilkington, M. B. G.; Stearn, G. M.; Unwin, P. R. *Journal of Electroanalytical Chemistry* **1987**, *238*, 43.
(29) Anderson, J. L.; Moldoveanu, S. *Journal of Electroanalytical Chemistry* **1984**, *179*, 107.
(30) Matthews, S. M.; Du, G. Q.; Fisher, A. C. *Journal of Solid State Electrochemistry* **2006**, *10*, 817.
(31) Lide, D. R. *CRC Handbook of Chemistry and Physics*; CRC Press: USA, 2001.
(32) Bertoncello, P.; Ciani, I.; Li, F.; Unwin, P. R. *Langmuir* **2006**, *22*, 10380.
(33) Nakayama, Y. *Introduction to Fluid Mechanics*; Arnold, 1999.

5. Ultra-sensitive Voltammetry at SWNT Channel Electrodes

5.1. Aim

The deployment of SWNT network electrodes in channel flow for well-defined hydrodynamic voltammetry is reported. In essence, 2D VHD SWNT networks are combined with the MSL developed channel flow cell reported in chapter 4. The configuration provides well-defined hydrodynamics over a large range of flow rates (0.05 mL min^{-1} – 25 mL min^{-1}) providing a limiting current response of the SWNT electrode in agreement with the Levich equation (Equation 1.27). Furthermore, analysis with theoretical predicted values is demonstrated for $FcTMA^+$ over a wide concentration range of 13 nmol dm^{-3} to 21 μmol dm^{-3}. The hydrodynamic configuration is applied to the detection of dopamine where an estimated detection limit of 10 nmol dm^{-3} is reached.

5.2. Introduction

As discussed previously in chapters 1 and 4, hydrodynamic electrodes have been used for the continual monitoring of a solution[1-4]. The well-defined convection provided by tubular and channel flow cells is of particular interest for analytical studies, which can result in an increased signal for mass transport controlled reactions,[5-8] or facilitate the investigation of reaction kinetics.[9-13] By continually replacing the analyte solution at the electrode surface, soluble products that can foul or block an electrode can be removed as they are formed, enhancing the life time of an electrode.

Previously the channel flow and tubular electrode geometries have been used to increase the sensitivity of various electrodes.[14-16] Work utilising a platinum tube electrode, by Blaedel *et al.*,[8, 17] demonstrated the high sensitivity of convective systems by detecting 50 nmol dm^{-3} ferrocyanide via continual CA injection analysis. The technique was applied to channel flow electrodes where the combination of reticulated vitreous carbon discs with stop-flow techniques allowed for the detection limit of 1 nmol dm^{-3} ferrocyanide to be obtained from the difference between the two limiting current responses.[18] To allow a greater depth of analytical evidence to be obtained, the modulated flow technique was combined with CV measurements by Blaedel *et al.*[19] resulting in a detection limit of ~100 nmol dm^{-3}. However, the utilisation of modulated flow rates greatly limits the available scan rates for steady-state electrochemical measurements due to the relaxation time associated with the variation of the flow rate (figure 5.1). The scan rate and frequency of modulation of the flow rate can be increased, however the change in amplitude between the two flow rates is reduced (figure 5.1) and can no longer be easily predicted by the difference in the theoretical Levich responses. To allow fast scan CV and easily predictable data this chapter focuses on detection using a constant flow rate, this approach sacrifices the enhanced sensitivity provided by variable flow rate techniques but removes the associated scan rate limitations.

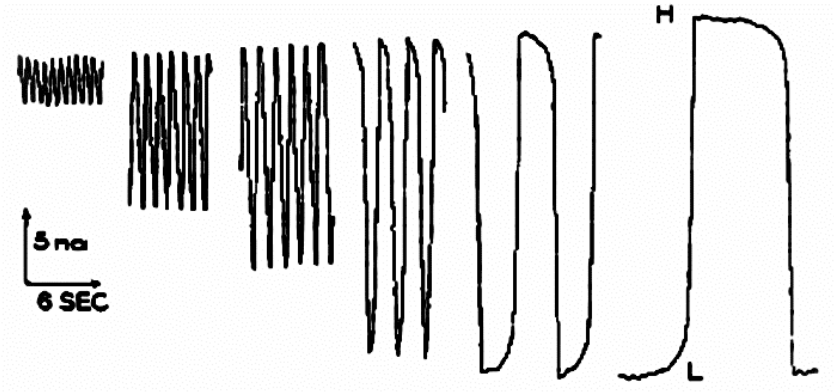

Figure 5.1 The effect of increasing the frequency of modulation of flow rates upon the CA response. The frequency of modulation decreases from left (highest) to right (lowest). The right hand image shows the measurement at steady state for flow rates H and L.[19] Results shown for a tubular electrode of with a tube of radius 0.2 mm and electrode length of 1 mm, flow rates are modulated from 3 mL min^{-1} – 6 mL min^{-1}.

As discussed in chapter 3, the diffusion profiles to the active areas of the SWNT network overlap to provide linear diffusion similar to that of a macro electrode on the observable timescales for a typical redox mediator in aqueous solutions. The diffusional overlap provides a transport limited current similar to an all active electrode material, however as the active area is reduced the non-Faradaic background signal is reduced. Bertoncello *et al.*[20] demonstrated a 100 fold decrease in the background current on a SWNT network compared to a GCE of the same size, this reduced current was attributed to only 1% of the surface being covered by SWNTs. A similar reduction in the non Faradaic-background was also observed for a SWNT network UME by Dumitrescu *et al.*[21]

The detection and accurate analysis of dopamine levels within solution is a medically relevant area, which provides insights into neurological processes.[22-24]

Dopamine is a neural transmitter and monitoring the levels of dopamine present within the brain could further the investigation, and potentially lead to the development of cures, for several neurological diseases *e.g.* attention deficit disorder[25] and Parkinson's disease[23]. One of the major problems with the detection of dopamine is the fouling or blocking of the electrode during oxidation. This effect has been observed upon GCEs and carbon fibre electrodes leading to reduced electron transfer rates.[26, 27] The blocking effect was noted to be significantly reduced upon a GCE modified with CNTs by Britto *et al.*[28], and similar results were observed with UMEs made of VHD SWNT networks by Dumitrescu *et al*.[29] This makes CNTs, particularly the VHD SWNT networks, an interesting electrode material for the electroanalysis of biomolecules.

The MSL channel designed in chapter 4 is applied to a VHD SWNT network and used to probe nano-molar concentrations of $FcTMA^+$ and dopamine. The reduced non-Faradaic background currents and fouling effects towards biomolecules allows the detection limit of constant flow rate measurements to match those previously provided by pulsed flow voltammetry. This greatly reduces the time for analysis without sacrificing the accuracy of measurements.

5.3. Experimental

This section highlights several methods which were used in creating a well defined and electrochemically sensitive macro electrode from a VHD SWNT network, and techniques employed to provide accurate low concentration analysis.

5.3.1. Electrode Preparation

The VHD SWNT network was grown by cobalt catalysed cCVD using ethanol as the carbon feedstock, as described in section 2.1. Only samples with a network density ≥ 4 μm_{SWNT} μm^{-2} were used within this chapter. Electrical contacts were made by evaporating a Cr/Au band (10 nm/120 nm) defined by shadow masking onto the sample. The electrode area was defined by a photolithography using a custom made mask producing 2 bands of w_e = 1.5 mm and x_E = 0.5 mm (figure 5.2).

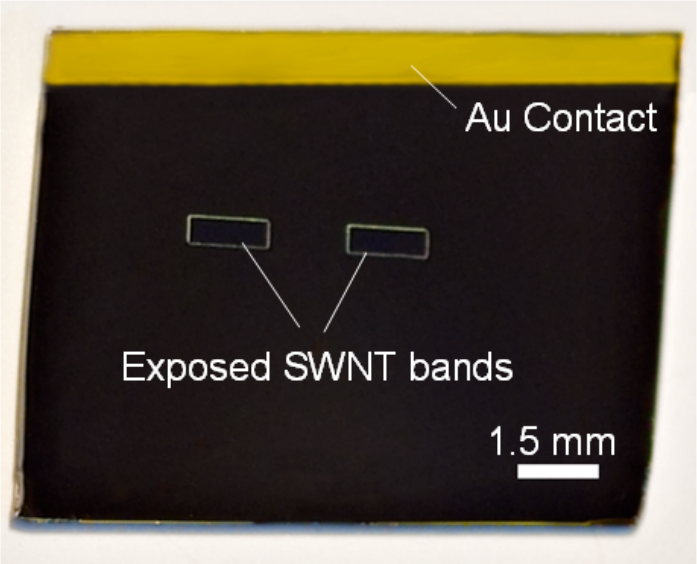

Figure 5.2 Photograph of a SWNT network sample with the 2 band electrodes defined by photolithography.

5.3.2. Analyte Preparation and Delivery

Solutions of $FcTMA^+$ (synthesised in house[30]) in 0.01 M KNO_3 (99.999% Sigma Aldrich), and dopamine hydrochloride (Sigma Aldrich) in 0.01 M phosphate buffered saline solution (PBS) were used for all experiments. The channel flow cell was

created in house by MSL, as reported in chapter 4. The channel height was measured by white light interferometry (Wyko NT-2000 Surface Profiler, WYKO Systems) and all channels used in this report had working dimensions of w = 3.0 mm and $2h$ = 192 μm. Analyte solutions were delivered via a Gilson 305 HPLC pump at a flow rate of 25 mL min^{-1}. To minimise the effect of analyte adsorption onto the walls of the delivery system all parts were soaked for 1 hour in a 25 μmol dm^{-3} analyte solution. The flow cell was rinsed with 0.01 M KNO_3 until the CV response was identical to the pre-soak background.

5.3.3. Electrochemical Measurement

CV and LSV measurements were performed in the 2-electrode mode using a CHI750C potentiostat at 10 mV s^{-1} scan rate with a SCE quasi-reference electrode. The SCE electrode was mounted inside a pipette tip (Finn, Thermo Scientific). A 5 mL pipette tip was cut across the circumference of the central body. A rubber O-ring was mounted onto the SCE and inserted into the pipette. Once assembled analyte solution was injected into the tip of the pipette until the entire pipette-SCE assembly was filled with analyte. The pipette tip was inserted into the reference hole designed in the flow cell, and secured with modelling putty. A schematic of the modified SCE used and a photograph of the SCE setup are shown in figure 5.3. The use of this reference method prevented contamination of the SWNT sample observed with the use of a chlorinated silver wire.

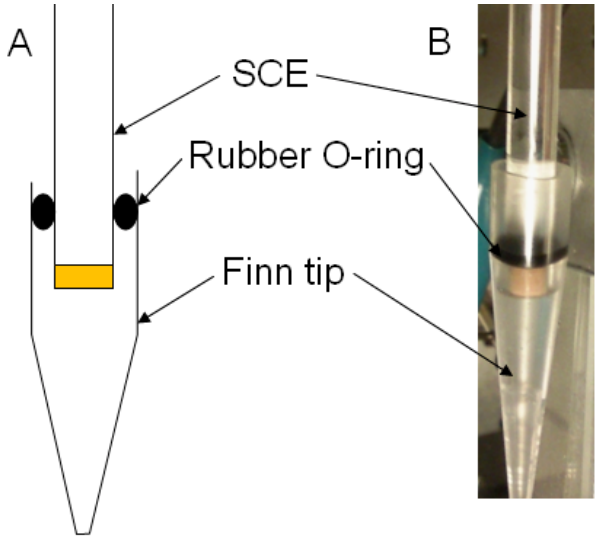

Figure 5.3 (a) Schematic of the SCE electrode assembly and (b) photograph of the assembled SCE with Finn tip.

5.4. Results and Discussion

5.4.1. VHD SWNT Network Characterisation

The samples to be used were for electroanalysis were characterised for network density by AFM. Only samples with a density ≥ 4 μm_{SWNT} μm^{-2} were used for the experiments within this chapter. A typical AFM image of a VHD SWNT network is shown in figure 5.4 (a). To ensure that the electrode preparation methods were suitable for electrochemical analysis, CVs were performed within a solution containing only supporting electrolyte (0.01 M KNO_3). Figure 5.4 (b) shows the potential window and the low non-Faradaic background currents for the VHD SWNT network.

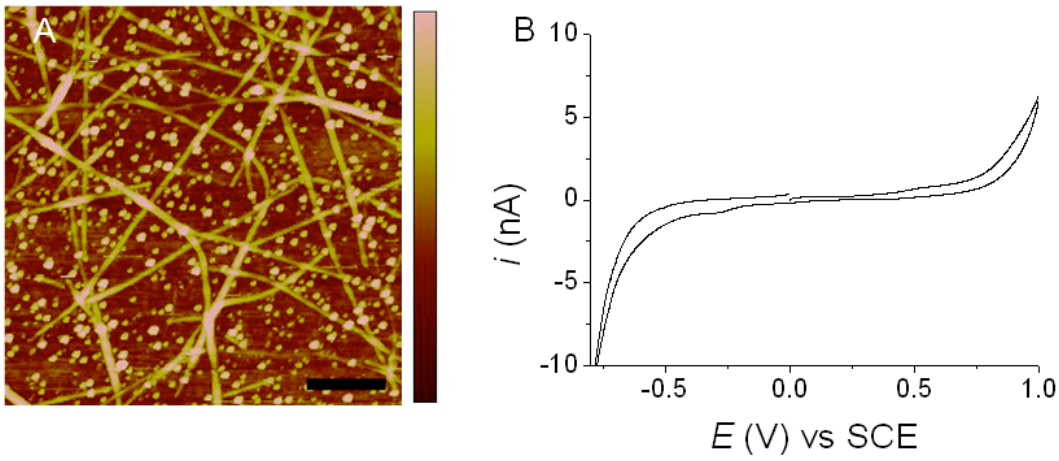

Figure 5.4 (a) A typical AFM image of a SWNT network of density ~8 μm μm^2, scale bar is 200 nm with a z scale bar of 7.5 nm., and (b) a typical background CV in 0.01 M KNO_3

CVs over a range of flow rates on the SWNT electrodes were performed using 21 μmol dm^{-3} $FcTMA^+$ in 0.01 mol dm^{-3} KNO_3 using a band electrode of x_e = 0.5 mm, w_e = 1.5 mm within a channel of width 3 mm and $2h$ = 192 μm. Figure 5.5 (a) shows the LSVs which were used to determine the limiting current response with respect to flow rate. The agreement between the experimental limiting current and the theoretical values, figure 5.5 (b), shows that the SWNT band electrode is well defined and does not affect the hydrodynamics of the channel as the limiting current responses are accurately predicted by the Levich equation (equation 1.27).

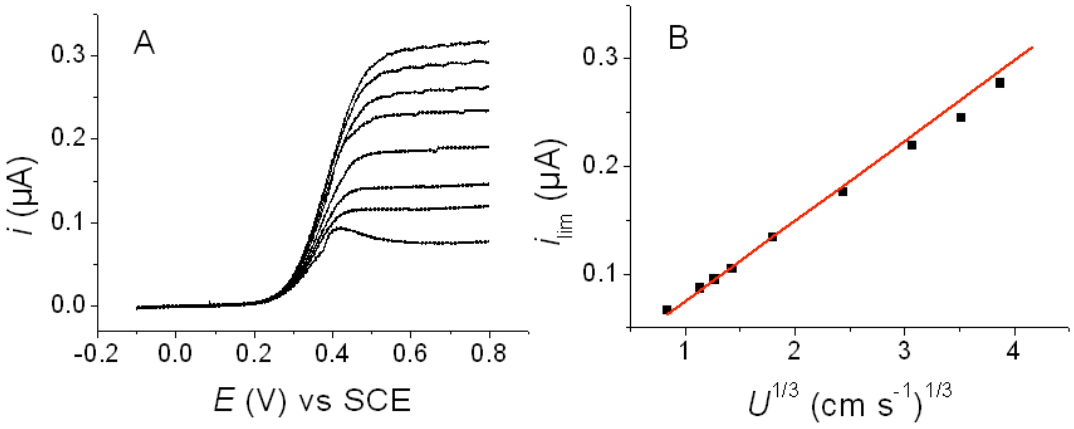

Figure 5.5 (a) LSVs taken at 10 mV s^{-1} in 21 μmol dm^{-3} $FcTMA^+$ and 0.01 mol dm^{-3} KNO_3 at flow rates of 0.2, 1.0, 2.0, 5.0, 10.0, 15.0, 20.0 and 25.0 mL min^{-1} and (b) linear fit of the limiting current response to the Levich equation, for a band electrode of x_e = 0.5 mm, w_e = 1.5 mm within a channel of width 3 mm and $2h$ = 192 μm.

To explore low concentration detection, measurements were made using $FcTMA^+$ in 0.01 M KNO_3, CVs for the detection of various concentrations of $FcTMA^+$ are shown in figure 5.6 (a), compared to the background scan in only 0.01 mol dm^{-3} KNO_3. The volume flow rate of 25 mL min^{-1} was chosen to provide the largest increase in the mass transport to the electrode surface. From the CVs it is possible to detect concentrations as low as 13 nmol dm^{-3} of $FcTMA^+$, with a linear relationship between the limiting current and the concentration observed over a range of 1 μmol dm^{-3} to 13 nmol dm^{-3} as shown in figure 5.6 (b).

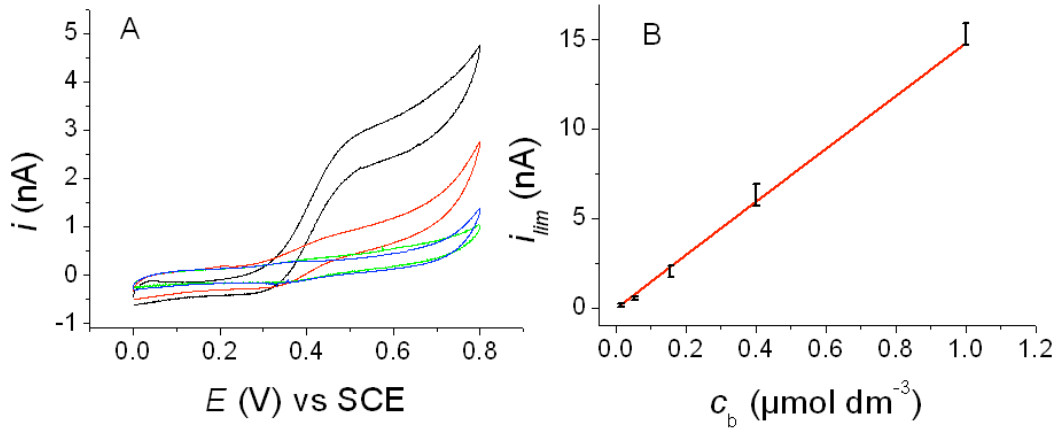

Figure 5.6 (a) CVs taken at 10 mV s^{-1} with a volume flow rate of 25 mL min^{-1} in (-) 156 nmol dm^{-3} (-) 52 nmol dm^{-3} (-)13 nmol dm^{-3} in 0.01 M KNO_3 and (-) only KNO_3, (b) shows the agreement with the Levich predicted response.

The concentration gradient follows a linear response with excellent agreement to the Levich predicted response for the experimental setup. The VHD SWNT network band electrode has a linear dependence upon the concentration and the response can be predicted simply from the Levich equation. The detection limit could be further improved by implementing the pulsed flow rate voltammetric techniques. The detection of 13 nmol dm^{-3} $FcTMA^+$ is shown in figure 5.7 compared to the background in supporting electrolyte. From the background scan and the linear concentration dependence on the limiting current response, a limit of detection of 10 nmol dm^{-3} $FcTMA^+$ is estimated, with a sensitivity of 14.8 mA dm^3 mol^{-1} (15 pA dm^3 $nmol^{-1}$) determined from the concentration gradient.

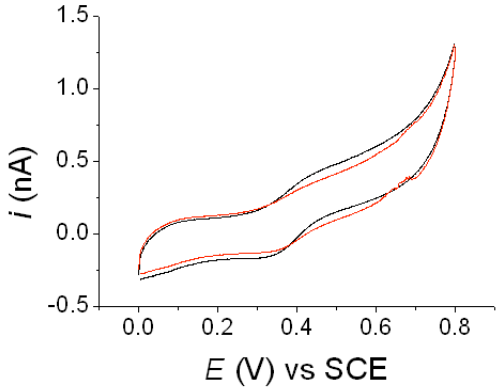

Figure 5.7 CV of 13 nmol dm^{-3} $FcTMA^+$ in 0.01 mol dm^{-3} KNO_3 (—) and in only 0.01 mol dm^{-3} KNO3 (—).

Figure 5.8 (a) shows CVs of 133 nmol dm^{-3}, 500 nmol dm^{-3} and 1.0 µmol dm^{-3} of dopamine at a scan rate of 10 mV s^{-1} using a flow rate of 25 mL min^{-1}. The CVs presented in figure 5.8 (a) are slightly more distorted than those obtained for $FcTMA^+$. This is to be expected as dopamine exhibits sluggish electron transfer kinetics at conventional carbon electrodes (such as GCE and carbon fiber electrodes) unless rigorous steps are taken to pre-treat the electrode surface.[26, 27]

The relationship between the bulk concentration and the limiting current is linear over the concentration range of 100 nM - 1 µM, as shown in figure 5.8 (b). However, the limiting current is 60% of that predicted by the Levich equation for the cell employed (assuming n = 2, D = 6 x 10^{-6} cm^2 s^{-1}).[28, 31] This could be due to blocking of the electrode surface.[32-34] The estimated limit of detection for Dopamine within the system employed within these studies is 10 nmol dm^{-3}, with a sensitivity of 16 mA dm^3 mol^{-1}.

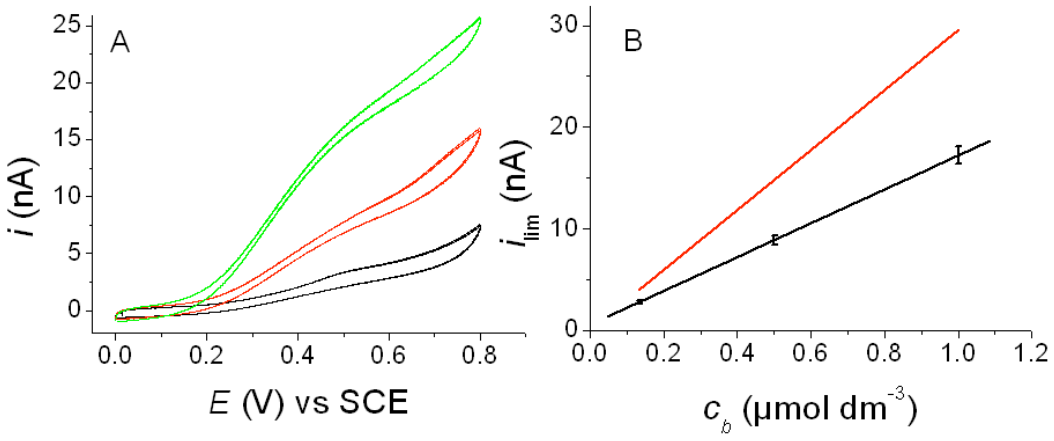

Figure 5.8 (a) CVs taken at 10 mV s^{-1} with a volume flow rate of 25 mL min^{-1} in (—) 1.0 μmol dm^{-3} (—) 500 nmol dm^{-3} (—) 133 nmol dm^{-3} in 0.01 M PBS, (b) shows the linear concentration gradient of dopamine (black data) against the Levich predicted response (—).

5.5. Conclusions

SWNT network band electrodes have been successfully combined within the channel flow cell for low concentration detection. The photo-resist mask provides a well defined band electrode of width = 1.5 mm and length = 0.5 mm, which has negligible effects on the hydrodynamics of the channel. This is demonstrated by the excellent agreement of experimental and theoretical limiting currents with the variation of flow rate. The limit of detection as determined by using $FcTMA^+$ is 10 nmol dm^{-3} at a flow rate of 25 mL min^{-1}. A linear response to the concentration is demonstrated from 10 nmol dm^{-3} – 21 μmol dm^{-3} for $FcTMA^+$. Importantly the detection limit using a constant volume flow rate is comparable to that obtained by pulsed voltammetric analysis. This removes the time restrictions associated with solution relaxation times allowing the use of fast scan LSV or CV measurements.

The limiting current response for dopamine is linear with respect to concentration over the range of 100 nmol dm^{-3} to 1.0 μmol dm^{-3}. The response is lower than predicted by the Levich equation, further investigation is required to determine if the effect is due to blocking of the electrode. Importantly this demonstrates that a SWNT electrode can be applied to channel flow electrochemistry, and that the flow cell design is amenable to a wide variety of novel electrode materials.

5.6. References

(1) Khoo, S. B.; Gunasingham, H.; Ang, K. P.; Tay, B. T. *Journal of Electroanalytical Chemistry* **1987**, *216*, 115.
(2) Cannan, S.; Unwin, P. R. *Electroanalysis* **2004**, *16*, 712.
(3) Swartzfager, D. G. *Analytical Chemistry* **1976**, *48*, 2189.
(4) Olsen, S.; Ruzicka, J.; Hansen, E. H. *Analytica Chimica Acta* **1982**, *136*, 101.
(5) Compton, R. G.; Unwin, P. R. *Journal of Electroanalytical Chemistry* **1986**, *206*, 57.
(6) Compton, R. G.; Unwin, P. R. *Journal of Electroanalytical Chemistry* **1986**, *205*, 1.
(7) Unwin, P. R.; Compton, R. G. In *Comprehensive Chemical Kinetics*; Compton, R. G., Hamnett, A., Eds.; Elsevier, 1989; Vol. 29, pp 173.
(8) Blaedel, W. J.; Olson, C. L.; Sharma, L. R. *Anal. Chem.* **1963**, *35*, 2100.
(9) Compton, R. G.; Daly, P. J.; Unwin, P. R.; Waller, A. M. *Journal of Electroanalytical Chemistry* **1985**, *191*, 15.
(10) Wakabayashi, N.; Takeichi, M.; Uchida, H.; Watanabe, M. *Journal of Physical Chemistry B* **2005**, *109*, 5836.
(11) Macpherson, J. V.; Simjee, N.; Unwin, P. R. *Electrochimica Acta* **2001**, *47*, 29.
(12) Rees, N. V.; Alden, J. A.; Dryfe, R. A. W.; Coles, B. A.; Compton, R. G. *The Journal of Physical Chemistry* **1995**, *99*, 14813.
(13) Wang, Z.; Zhao, M.; Scherson, D. A. *Analytical Chemistry* **1994**, *66*, 4560.
(14) Blaedel, W. J.; Wang, J. *Analytical Chemistry* **1979**, *51*, 1724.
(15) Economou, A.; Voulgaropoulos, A. *Talanta* **2007**, *71*, 758.
(16) van Staden, J. F.; Matoetoe, M. C. *Analytica Chimica Acta* **1998**, *376*, 325.
(17) Blaedel, W. J.; Boyer, S. L. *Analytical Chemistry* **1971**, *43*, 1538.
(18) Blaedel, W. J.; Wang, J. *Analytical Chemistry* **1979**, *51*, 799.
(19) Blaedel, W. J.; Yim, Z. *Analytical Chemistry* **1980**, *52*, 564.
(20) Bertoncello, P.; Edgeworth, J. P.; Macpherson, J. V.; Unwin, P. R. *Journal of the American Chemical Society* **2007**, *129*, 10982.
(21) Dumitrescu, I.; Unwin, P. R.; Wilson, N. R.; Macpherson, J. V. *Analytical Chemistry* **2008**, *80*, 3598.
(22) Venton, B. J.; Wightman, R. M. *Analytical Chemistry* **2003**, *75*, 414A.

(23) Gash, D. M.; Zhang, Z. M.; Ovadia, A.; Cass, W. A.; Yi, A.; Simmerman, L.; Russell, D.; Martin, D.; Lapchak, P. A.; Collins, F.; Hoffer, B. J.; Gerhardt, G. A. *Nature* **1996**, *380*, 252.
(24) Wightman, R. M. *Science* **2006**, *311*, 1570.
(25) Vickrey, T. L.; Condron, B.; Venton, B. J. *Analytical Chemistry* **2009**, *81*, 9306.
(26) DuVall, S. H.; McCreery, R. L. *Analytical Chemistry* **1999**, *71*, 4594.
(27) Allred, C. D.; McCreery, R. L. *Analytical Chemistry* **1992**, *64*, 444.
(28) Britto, P. J.; Santhanam, K. S. V.; Ajayan, P. M. *Bioelectrochemistry and Bioenergetics* **1996**, *41*, 121.
(29) Dumitrescu, I.; Edgeworth, J. P.; Unwin, P. R.; Macpherson, J. V. *Advanced Materials* **2009**, *21*, 3105.
(30) Bertoncello, P.; Ciani, I.; Marenduzzo, D.; Unwin, P. R. *J. Phys. Chem. C* **2007**, *111*, 294.
(31) DuVall, S. H.; McCreery, R. L. *Journal of the American Chemical Society* **2000**, *122*, 6759.
(32) Qureshi, A.; Kang, W. P.; Davidson, J. L.; Gurbuz, Y. *Diamond and Related Materials* **2009**, *18*, 1401.
(33) Orton, R.; Unwin, P. R. *Journal of the Chemical Society-Faraday Transactions* **1993**, *89*, 3947.
(34) Takmakov, P.; Zachek, M. K.; Keithley, R. B.; Walsh, P. L.; Donley, C.; McCarty, G. S.; Wightman, R. M. *Analytical Chemistry*, *82*, 2020.

6. Design and Testing of a MSL Radial Flow Cell

6.1. Aim

The advantages of MSL for the fabrication of channel flow cells has been demonstrated in chapters 4 and 5, allowing high precision features to be developed and maintained when assembled onto an electrode material. This methodology is applied to the fabrication of an impinging jet electrode (IJE) to create well defined radial flow. As for the channel flow cell, the radial flow cell can be rapidly assembled and can be applied to a variety of electrode materials. This is demonstrated by the application to Au and SWNT disc electrodes. 2D and 3D FEM simulations are performed to critically assess the hydrodynamics within several potential designs of the channel. The final design is tested by comparing experimental data to the current response predicted by 2D simulations of the device.

6.2. Introduction

Radial flow is an important component of the hydrodynamics of IJEs, widely used in the study of reaction mechanisms and kinetics.[1-4] For all IJE techniques, the height of the nozzle over a planar substrate and the position of the electrode with respect to the nozzle must be well known. There are two common variants for the assembly of an IJE. These involve either encapsulating an electrode within a planar substrate beneath the nozzle (figure 6.1(a))[2, 5-9] or combining the electrode with the nozzle[10, 11] (figure 6.1(b)).

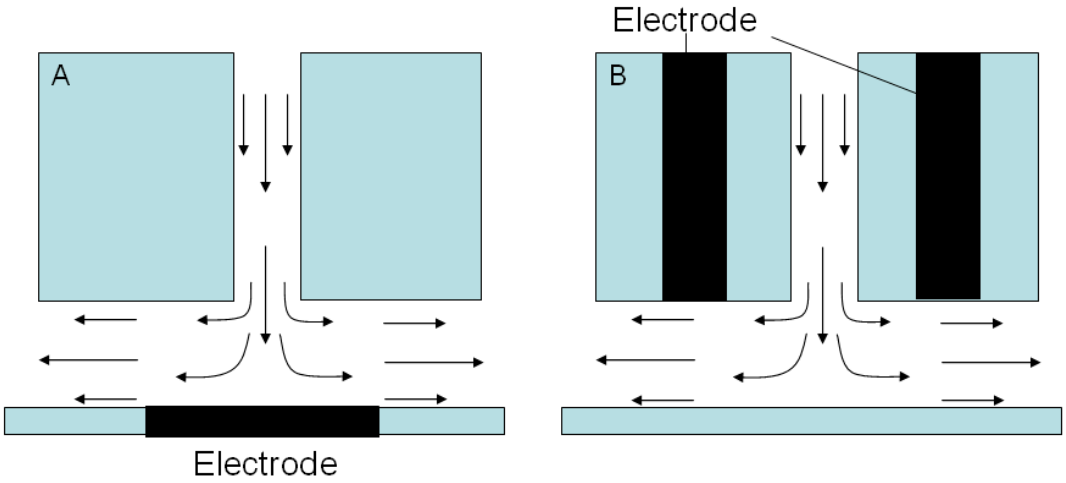

Figure 6.1 Cross-sectional schematics of electrode position in IJEs. (a) Disc electrode mounted within the substrate below the nozzle, and (b) ring electrode mounted in the nozzle.

The dimensions of the IJE setup have been greatly miniaturised over the past half century, from a few millimetres for the nozzle radius and electrode radius[8, 12, 13] down to micro-jet setups with the nozzle diameter being ~100 μm located over an UME.[14, 15] The miniaturisation of the electrode and nozzle sizes allows for greater mass transport rates to be achieved enabling fast kinetics of electrochemical processes to be studied.[1, 16]

The height of the nozzle above the substrate is typically determined by optical measurement using a camera,[15] by contact and *z*-axis manipulation,[8] or by electrochemical calibration.[17] Optical measurement is the least invasive technique as the nozzle and substrate do not make contact but limits the type of cells and solutions that can be used. The contact methodology provides an accurate measurement of the nozzle height but care must be taken not to damage the nozzle or the substrate surface. As discussed previously for the channel flow electrode, the use of electrochemical calibration experiments introduces the possibility of complications from fouling of the substrate-electrode surface.

The alignment of the electrode and the nozzle has a large impact on mass transport to the electrode surface. This is illustrated by the variation in limiting current for a WTE when the *x* and *y* position of the nozzle, with respect to the electrode, is varied (figure 6.2). The central stagnation domain of mass transport and the radial flow profile of an IJE can be observed by the concentric variation in the limiting current the further the electrode is positioned from the centre of the nozzle (figure 6.3 (a) and (b)).[2] It is important to note that the decrease in limiting current when the electrode and nozzle are aligned, due to the stagnation zone, is only observed when the electrode is sufficiently small that the entire electrode is within the stagnation zone. Hence, the method where the electrode is imbedded within the planar substrate requires accurate *x* and *y* alignment of the nozzle over the centre of the electrode.[1, 2, 5, 8, 18] This can be performed by piezo or micrometer manipulation; however accurate alignment maybe time-consuming.

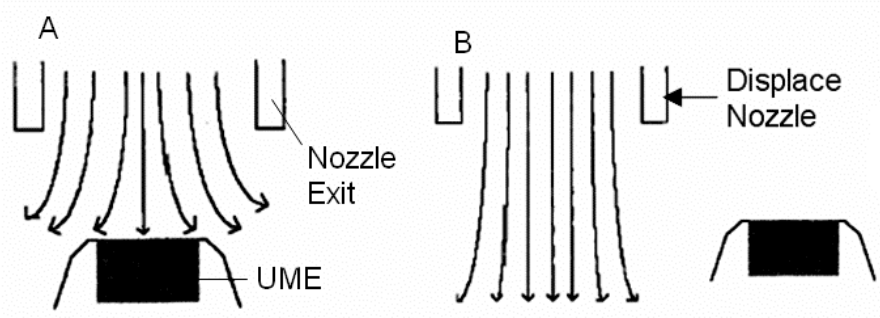

Figure 6.2 Illustration of the movement of the nozzle with respect to the electrode surface.[17] By measuring the i_{lim} response with respect to *x* and *y* displacement the plots in Figure 6.3 can be created. Not to scale.

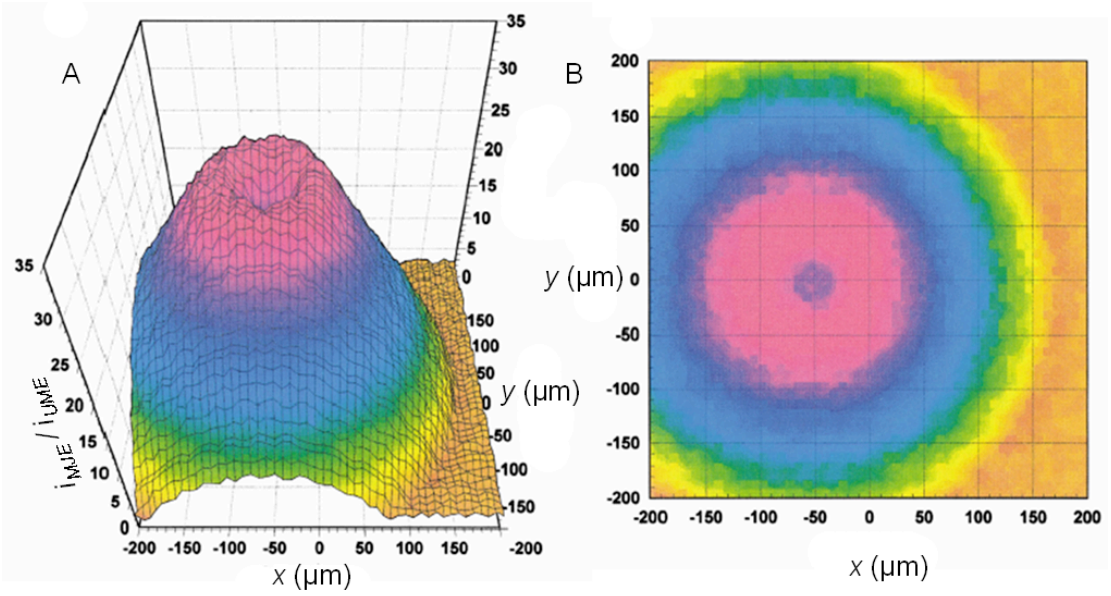

Figure 6.3 (a) Variation in the limiting current response with respect to *x*-*y* position of a 105 μm diameter nozzle 300 μm above the surface of a 25 μm diameter UME. (b) Plot (a) redrawn to emphasise the radial decrease of the limiting current response. Colours represent the same currents as shown in (a).[2]

By incorporating the electrode into the nozzle design the position of the electrode can be easily characterised prior to assembly of the IJE, as in the radial flow microring electrode. However, this technique restricts the electrode geometry to a ring and has so far only been applied to metallic electrode materials, though the fabrication technique employed by Macpherson *et al.*,[10] utilising a metal paint, is feasible for any electrode material used for the fabrication of screen printed electrodes (figure 6.4).

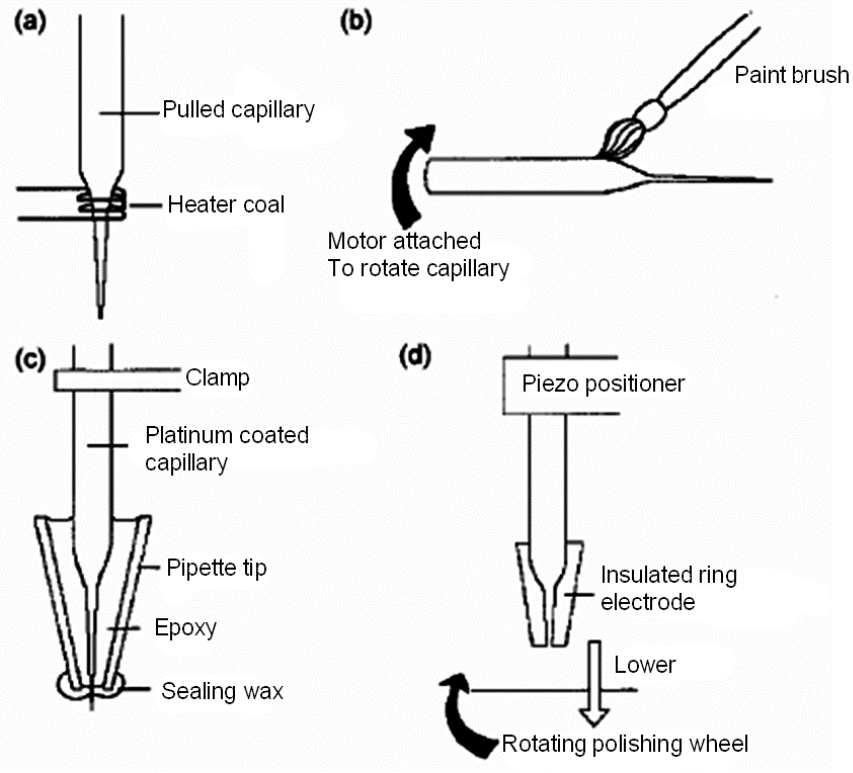

Figure 6.4 Schematic showing the stages of construction for a radial flow microring electrode. (a) The capillary is pulled before (b) being evenly coated with Pt paint. (c) The Pt paint is insulated in epoxy and (d) polished flat to expose a Pt ring.[10]

The MSL channel flow devices, demonstrated in the chapters 4 and 5, have shown that the height of the channel is well defined and is not distorted upon assembly. It is shown herein that this advantageous feature of the MSL designs can be applied to an impinging jet configuration. Additionally, the high precision and resolution of features in the *x* and *y* axis of the build allow for complex internal structures to be created, giving freedom in design to create novel structures which were previously not easily produced. As discussed in section 1.4.4 the size of the electrode governs whether the system is defined as a wall jet electrode (WJE) or wall tube electrode (WTE). As the design is a 2 part assembly, similar to the channel flow cell presented in chapter 4, the size and geometry of the electrode can be easily varied allowing the

device to be used in both the WJE and the WTE configurations. As such the device developed is generically referred to herein as a radial flow cell (RFC).

6.3. Hydrodynamic FEM Simulations

This section discusses the simulations which investigate the hydrodynamics within potential designs for a RFC. All numerical simulations within this chapter were performed on a desktop computer equipped with an Intel Pentium III Xeon quad core 2.5 GHz processor and 8 GB of RAM running Windows XP Professional 64 bit, using the commercial finite element modelling package Comsol Multiphysics 3.5a (Comsol AB, Sweden), with the Matlab interface (Release 2009a) (MathWorks™ Inc., Cambridge, UK).

FEM has previously provided valuable insights into the hydrodynamics of impinging jet electrodes,[7, 15, 19-25] and is used herein to theoretically verify the design, and later within the chapter to experimentally assess the MSL fabricated RFCs.

As discussed in section 1.4.4, there are two limiting cases for the hydrodynamics caused by an impinging jet. One where the nozzle is sufficiently far from the electrode surface so that the fluid flow is not restricted (figure 6.5(a)),[7, 26] and the other where the nozzle wall is close to the electrode surface, causing a radial channel flow profile (figure 6.5(b)).[6, 10] This section describes both cases with the use of FEM and discusses the design advantages that the latter case provides for a MSL fabricated RFC.

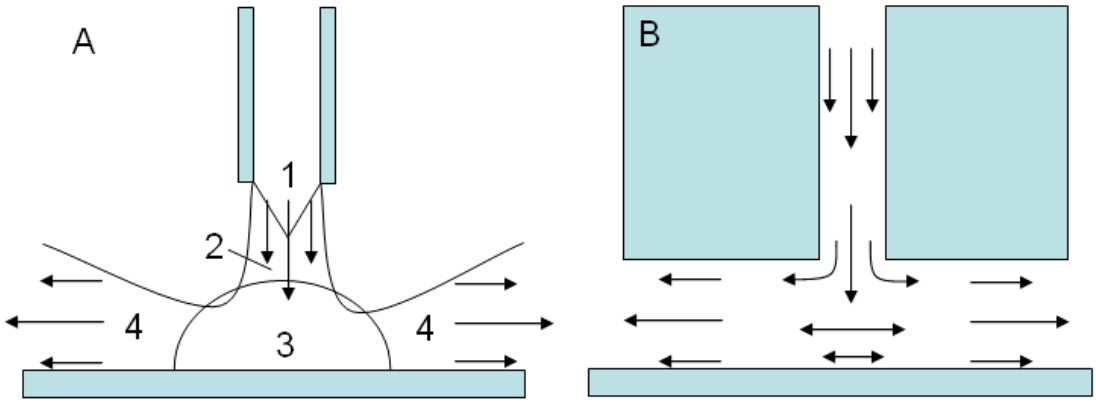

Figure 6.5 Schematics of the two limiting cases of impinging jets (a) where the nozzle is far from the surface, and (b) where the nozzle is close to the surface. Not to scale.

6.3.1. Hydrodynamics of an IJE where the Nozzle is far from the Surface

This situation has been used widely for investigations of the hydrodynamics caused by an impinging jet.[7, 15, 21, 27] The schematic shown in figure 6.5 (a) can be approximated to a 2D model with axial symmetry around the central axis of the nozzle. A schematic of the 2D domain with the boundary labelling conventions is shown in figure 6.6.

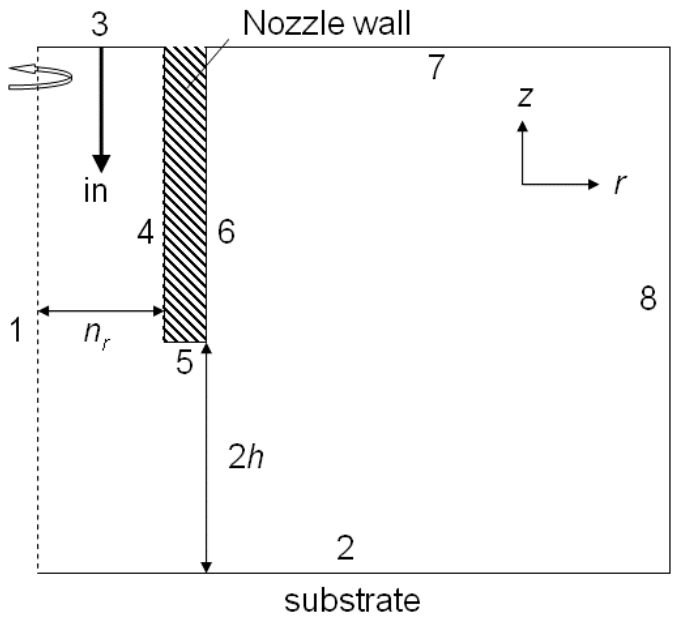

Figure 6.6 2D domain used for the simulation of the hydrodynamics of an impinging jet where the nozzle is far from the electrode surface. (Not to Scale)

Solving the incompressible Navier-Stokes equations for momentum balance (equation 6.1) and continuity (equation 6.2), allowed the calculation of the velocity profile for the impinging jet.

$$\rho \mathbf{V} \cdot \nabla \mathbf{V} = -\nabla (p + \eta (\nabla \mathbf{V} + (\nabla \mathbf{V})^T)) \quad \textbf{(6.1)}$$

$$\nabla \cdot \mathbf{V} = 0 \quad \textbf{(6.2)}$$

where ρ is the density of water (assumed reasonably to be 1.00 g cm^{-3}),[28] $\mathbf{V}$ is the velocity vector (with components u_r and w in the r and z directions, respectively, as defined in figure 6.6, p is pressure, η is the dynamic viscosity of water, which is 1.00 mPa s for the experimental conditions used herein, and T is the matrix transpose operator. The following boundary conditions were applied:

Boundary 1: $u_r = 0$ **(6.3)**

Boundaries 2, and 4-6: $u_r = 0,\ w = 0$ **(6.4)**

Boundary 3: $u_r = 0,\ w = -\frac{V_f}{\pi r_n^2}$ **(6.5)**

Boundary 7 and 8: $p = p_0,\ \eta(\nabla \mathbf{V} + (\nabla \mathbf{V})^T)\mathbf{n} = 0$ **(6.6)**

where u_r is the fluid velocity in the r direction. For the simulations within this section the nozzle radius (r_n) was 25 μm with a height ($2h$) of 500 μm above the planar surface.

Previous work by Bitziou *et al.*[7] has shown that there are essentially three distinct flow regimes which depend upon the flow rate of the solution out of the nozzle, the density and viscosity of the liquid, and the geometry of the impinging jet setup. The first situation occurs for low nozzle exit velocities, which is illustrated in figure 6.7 for the case of V_f = 1 μL min^{-1}. The potential core region of the flow does not extend far from the nozzle due to the solution viscosity causing resistance to motion, resulting in a broadening of the potential core.

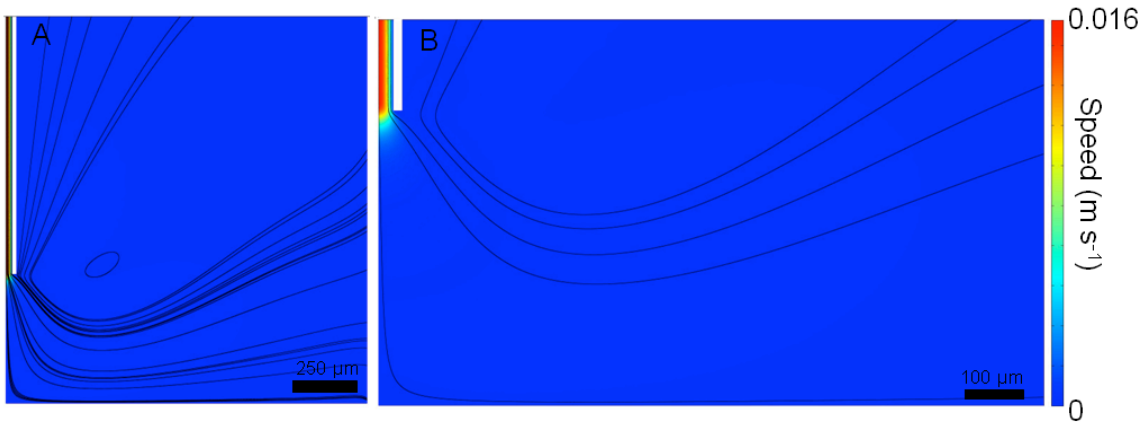

Figure 6.7 FEM of the velocity profile for the low nozzle exit velocity situation where V_f is 1 µL min^{-1}. (a) The entire simulated domain and (b) close up of the radial decay of the fluid velocity exiting the nozzle.

For the second situation, the solution is moving fast enough to develop a potential core that broadens just above the electrode (substrate) surface. After impinging upon the electrode surface the solution flows out radially. Due to the low velocity, a recirculation effect occurs due to the transfer of momentum from the potential core to the neighbouring solution. This creates an eddy, or vortex, which draws part of the solution that has passed over the electrode surface back towards the potential core, as shown in figure 6.8 for $V_f = 0.1$ mL min^{-1}.

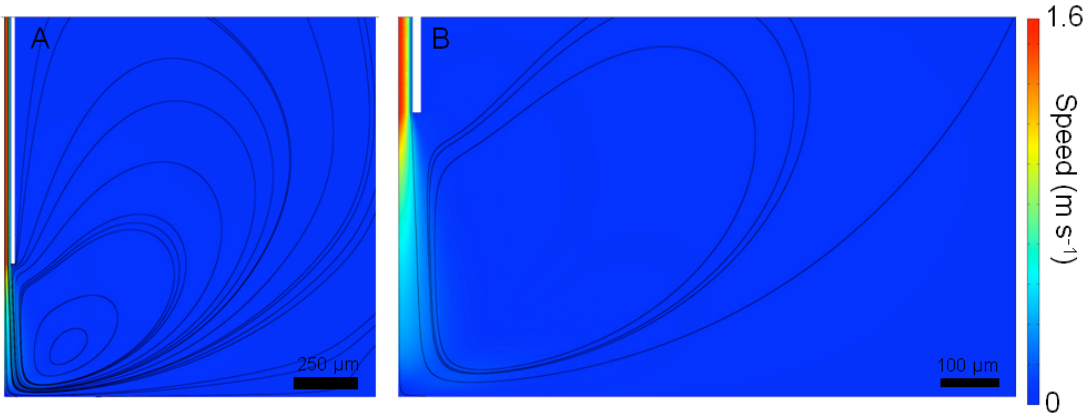

Figure 6.8 FEM of the velocity profile for the intermediate nozzle exit velocity situation at V_f = 0.1 mL min^{-1}. (a) The entire simulated domain and (b) close up of the decay of the fluid velocity exiting the nozzle.

The third regime occurs for fast moving solution, in this case a V_f of 0.3 mL min^{-1}, where the potential core impacts the surface resulting in the radial flow being sufficiently fast that the impinged solution flows out similar to a radial channel (figure 6.9). Due to the high speed of the potential core, the vortices observed in the second situation are much larger. The hydrodynamics of this situation are much harder to simulate than for the previous two situations, due to the high velocities involved, and the large change in velocities between the fluid in the vortices and within the potential core. Simulations for this geometry, with fluid speeds greater than those presented infigure 6.9, require a more complex approach for solutions using Comsol. For example, by gradually increasing the flow rate, or by decreasing the viscosity, within the simulation through the use of a sequential solver, it may be possible to increase the upper fluid velocity limit. The sequential solver initially performs a simulation that is known to converge, for example at a low volume flow rate. The initial result is used as a starting point for the next simulation where the volume flow rate is increased. This process is continued until the desired fluid velocity for the liquid is

reached. The details of sequential solvers are beyond the scope of this thesis and are the subject of further investigations.

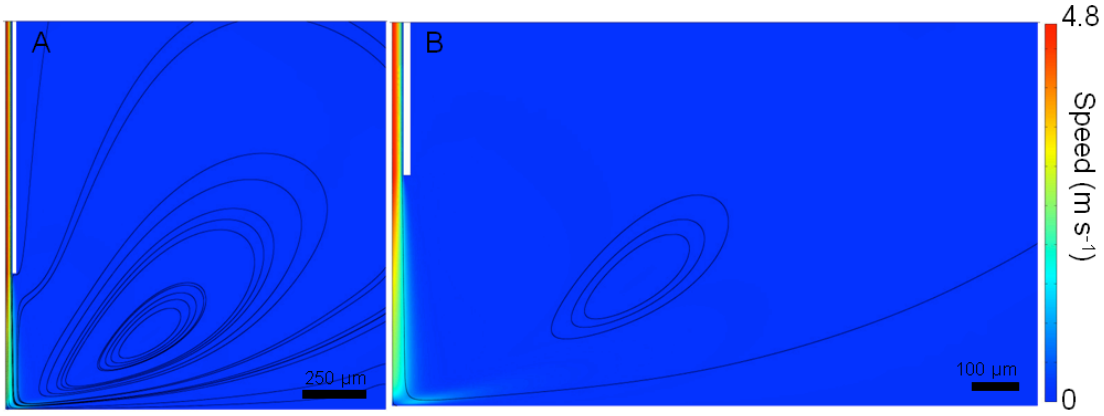

Figure 6.9 FEM of the velocity profile for the high nozzle exit velocity situation for a V_f of 0.3 mL min^{-1}. (a) The entire simulated domain and (b) close up of the fluid velocity exiting the nozzle.

The information provided by the FEM of this geometry shows the complexities of the hydrodynamics of this impinging jet geometry. The effects of recirculation and the variation of the fluid profile with inlet velocity complicate mass transport and hence the electrochemical response observed at an electrode directly beneath the nozzle. This geometry is practically assembled by lowering a pulled pipette tip over a surface.[6, 7, 15, 21] Typically, this requires an external support for the nozzle (usually attached to a micro manipulator) and the assessment of the height must be made for each setup (for example, an optical microscope).

6.3.2. Hydrodynamics for an Impinging Jet where the Nozzle is Close to the Surface

The 2D geometry, presented in figure 6.10, is also an axisymmetric cylindrical geometry. Convection within the entire simulation domain is solved for using the

incompressible Navier-Stokes and continuity equations, with the following boundary conditions:

Boundary 1: $u_r = 0$ **(6.7)**

Boundaries 2, 5-7, 9-11, and 13: $u_r = 0,\ w = 0$ **(6.8)**

Boundary 4: $u_r = 0,\ w = -\frac{V_f}{\pi r_n^{\,2}}$ **(6.9)**

Boundary 12: $p = p_0,\ \eta(\nabla \mathbf{V} + (\nabla \mathbf{V})^T)\mathbf{n} = 0$ **(6.10)**

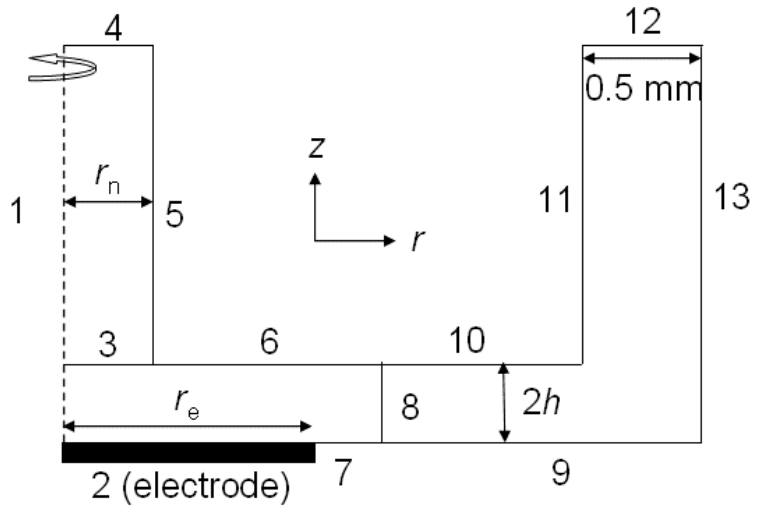

Figure 6.10 2D FEM domain used for the simulation of the electrochemical response of an electrode within the RFC

Boundary 1 is the centre point of the inlet nozzle and is the axis of rotational symmetry in the system. Boundaries 2, 5-7, 9-11, and 13 are the walls of the system and are set to have a no slip boundary condition. Boundary 4 represents the inlet, boundary 12 the outlet section of the wall jet, and boundaries 3 and 8 are not considered in the calculation of the velocity profile.

A typical flow profile is shown in figure 6.11, where solution from the nozzle in section 1 develops Poiseuille pipe flow by section 2. The solution impinges upon the electrode surface before flowing outwards through the confined channel. Section 3 shows the stagnation zone within the centre of the nozzle, with section 4 showing the increase in fluid velocity as the solution is confined at the start of the channel. The decrease in fluid velocity with increasing *r* is a result of the channel volume increasing with radial distance from the centre of the nozzle in section 5. An interesting difference between this situation and where the nozzle is far from the surface is that the velocity profile remains proportionally constant to the flow rate. This is due to the system effectively being closed, preventing the formation of vortices and recirculation.

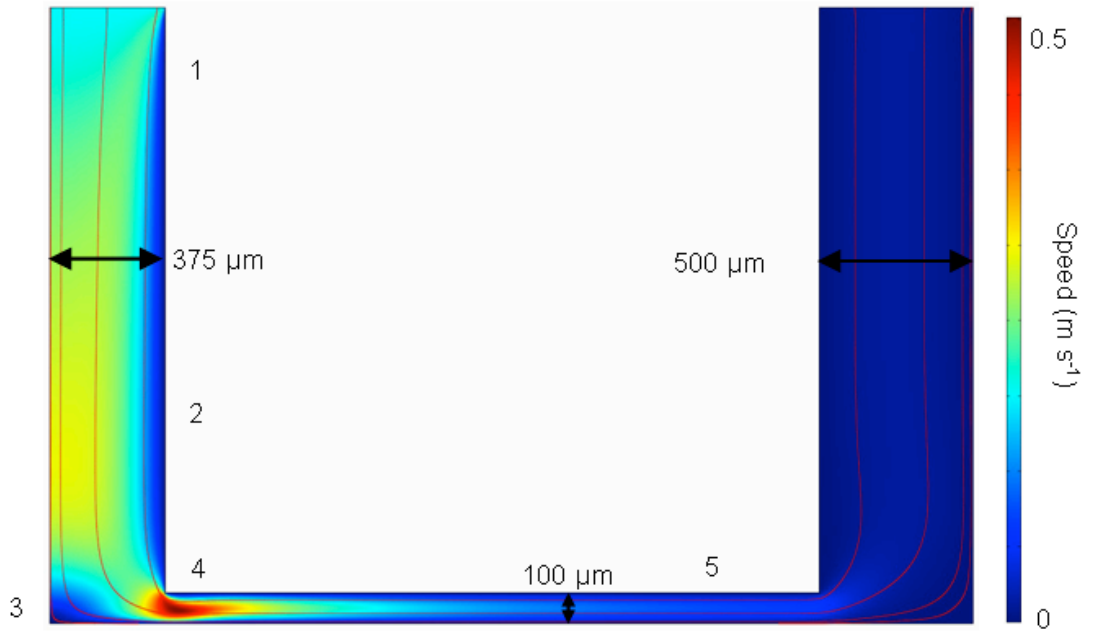

Figure 6.11 FEM predicted hydrodynamic profile for the situation where the nozzle confines the hydrodynamic flow. V_f = 5 mL min^{-1}.

The flow profile is consistent over the tested range of flow rates (0.05 mL min^{-1} – 25 mL min^{-1}). Additionally, the geometry is more amenable to MSL production than for when the nozzle is far from the surface. Hence, this system was considered for development into the RFC.

6.3.3. Critical Features for a Successful RFC

The critical feature for the MSL RFC setup is axially symmetric radial flow from the nozzle, which is both well-defined and predictable for a large range of volume flow rates. The device must deliver well-defined hydrodynamics for the observed electrochemical responses to be meaningful and predictable. Figure 6.12 (a) shows the 2D cross section upon which the RFC design was based; an idealised system where solution flows to waste along a planar substrate. So that the height of the nozzle above the electrode is accurately determined by securing the RFC to the substrate, a variation on the idealised IJE system is required. The resulting conceptual 2D RFC design, based upon the MSL channel flow cell (chapter 4), is shown in figure 6.12 (b). The conceptual design, defines the RFC height without the need for an external supporting arm, and houses the inlet and outlet. In order to replace the external support commonly employed by conventional microjet electrodes,[7, 15] an outer wall is required to support the bulk of the RFC (highlighted in red, figure 6.12 (b)) over the electrode. Hence, the conceptual design of a one piece RFC unit cannot have full 360° 2D rotational symmetry and support the bulk of the RFC at a known height. To overcome this design limitation, several outlet designs are investigated by FEM simulations. The information obtained is used to determine the effect of each of the outlet designs on the hydrodynamics. The insights provided by these simulations

are used to determine a viable outlet system which has minimal impact upon the ideal hydrodynamics.

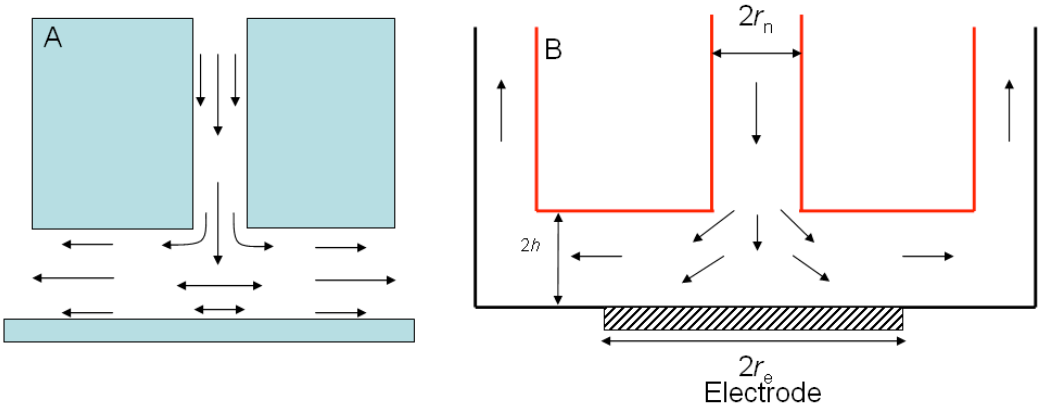

Figure 6.12 (a) 2D cross section of a radial flow wall jet system, and (b) a 2D concept sketch of the key sections of the RFC showing the unsupported internal section in red.

6.3.4. Determination of the Ideal Hydrodynamics within the RFC

To determine the hydrodynamics of the 2D conceptual system presented in figure 6.12 (b) an initial 3D model of the RFC was created. This model was initially used to determine the accuracy of the hydrodynamics within a 3D simulation compared to the 2D simulation, which will be discussed later in this section. This model acts as a bench mark for determining the effect the position of the outlet sections has on the hydrodynamics within the RFC. A wire frame view of the initial model is shown in figure 6.13.

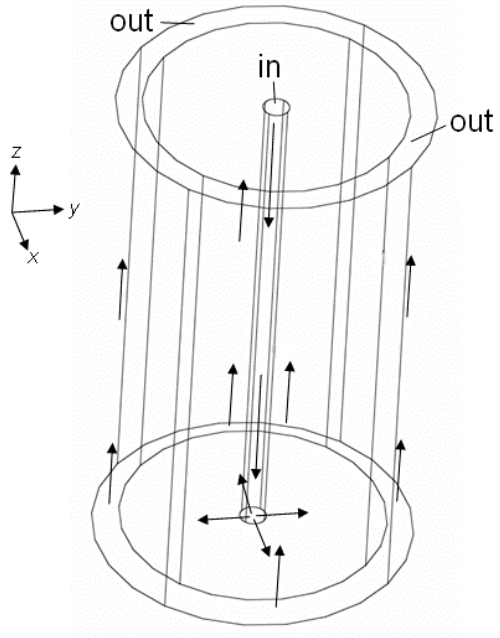

Figure 6.13 Wire Frame of the idealised radial flow cell with labelling conventions.

Solving the incompressible Navier-Stokes equations for momentum balance (equation 6.1) and continuity (equation 6.2) allowed the calculation of the velocity profile within the 3D simulation of the wall jet electrode. However for the 3D simulation, the velocity vector, **V**, used components *u, v* and *w* in the *x, y* and *z* directions, respectively, as shown in figure 6.13. The boundary conditions described by equation 6.11 – equation 6.13 were used for the finite element calculations:

Boundary "Wall": $u = 0,\ v = 0,\ z = 0$ **(6.11)**

Boundary "Inlet": $u = 0,\ v = 0,\ w = -\frac{V_{\mathrm{f}}}{\pi r_n^{\,2}}$ **(6.12)**

Boundary "Outlet": $p = p_0,\ \eta(\nabla \mathbf{V} + (\nabla \mathbf{V})^T)\mathbf{n} = 0$ **(6.13)**

where r_n is the nozzle radius (in this case 250 μm, a size that could initially be produced consistently by MSL), p and p_0 are the local pressure and the pressure of the

system, respectively, and **n** is the vector normal to a particular boundary. The "Inlet" boundary condition refers to the top of the central tube, where solution enters the system before impinging onto the base of the channel, the "Outlet" boundary condition applies to any boundary where solution leaves the system, and all other surfaces are defined by the boundary condition "Wall", illustrated in figure 6.13.

The flow profiles presented in figure 6.14 demonstrate well defined radial flow from the nozzle to the outlets. The fluid speed is initially low near the substrate at the centre of the nozzle, before increasing to a maximum as r increases. After the maximum speed the fluid speed decreases with the radial distance as the channel volume increases (due to the cylindrical geometry).

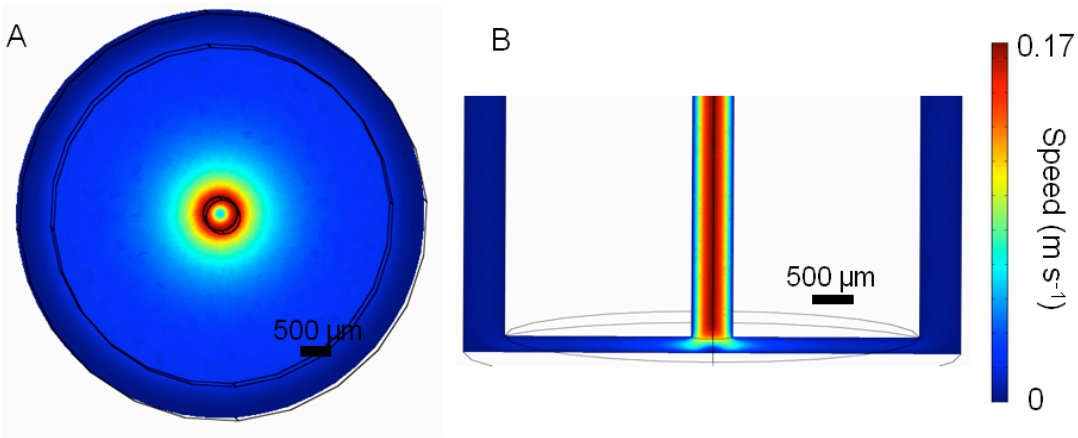

Figure 6.14 FEM of the Navier-Stokes convection within the idealised IJE configuration for r_n = 250 µm, $2h$ = 200 µm at V_f = 1 mL min^{-1} (a) top-down view, (b) cross section. Dark red represents a fluid speed of 0.13 m s^{-1}, dark blue represents a speed of 0 m s^{-1}.

The fluid velocity profiles for the 3D and 2D models of the idealised RFC geometry are shown in figure 6.15 (a) and (b). Both simulations use r_n = 250 µm, $2h$ = 200 µm at a V_f of 1 mL min^{-1}. As can be seen from figure 6.15, both models show the 5 hydrodynamic regions outlined in section 6.3.2.

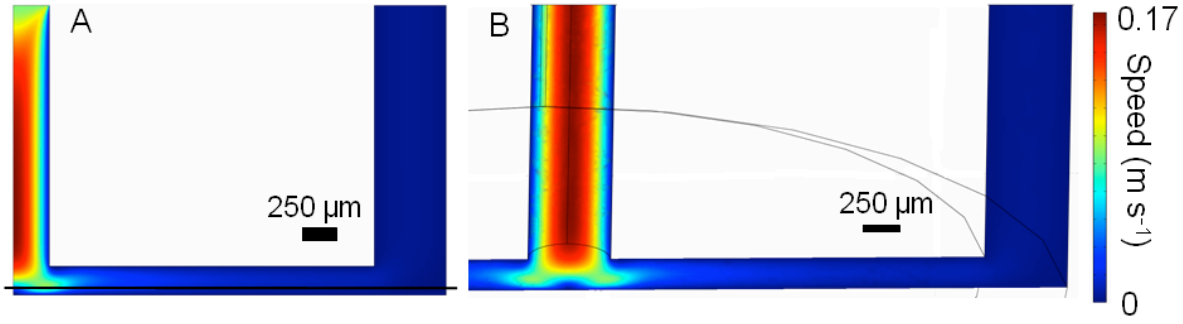

Figure 6.15 Comparison of the hydrodynamics within (a) the 2D simulation (black line represents cross section for the fluid velocity plot, figure 6.16) and (b) the idealised 3D simulation, where r_n = 250 µm, $2h$ = 200 µm at a V_f of 1 mL min^{-1}.

A plot of the fluid velocities, taken at a height of 50 µm, against radial distance from the centre of the nozzle is shown in figure 6.16. As expected, both models are in excellent agreement. This confirms that the methodology employed for the 3D simulation is an accurate method for the prediction of the hydrodynamics within the RFC.

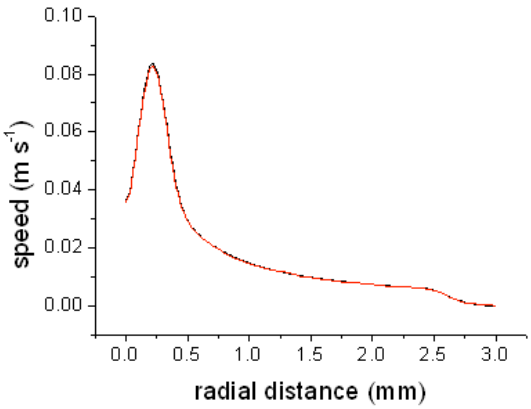

Figure 6.16 Comparison of the fluid velocity profile for the 2D simulation (black line) to the 3D idealised simulation (red line), where r_n = 250 µm, $2h$ = 200 µm at a V_f of 1 mL min^{-1}.

6.3.5. Hydrodynamics of a RFC with One Outlet

The first practical design tested was based upon a currently available commercial package (DropSens, Spain), where the device has one central inlet nozzle and a single outlet nozzle. figure 6.17 shows the wire frame of the model and illustrates where the boundary conditions used in section 6.3.4 are applied.

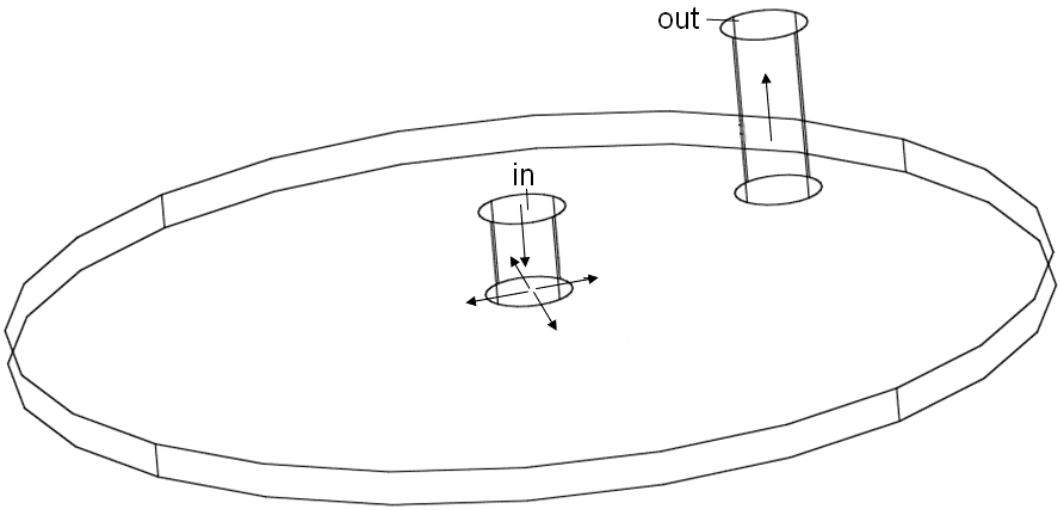

Figure 6.17 Wire frame schematic of the one outlet design with the inlet in the centre and an outlet recessed from the outer wall of the channel.

A major drawback of the device is the breaking of the cylindrical symmetry about the centre of the inlet nozzle. This results in the non-radial flow profile shown in figure 6.18. The solution velocity quickly becomes distorted upon exiting the nozzle, generating a higher solution speed at the leading inlet and outlet nozzle edges. This effect is more pronounced further from the centre of the inlet, with a stagnation effect evident at the furthest point from the outlet.

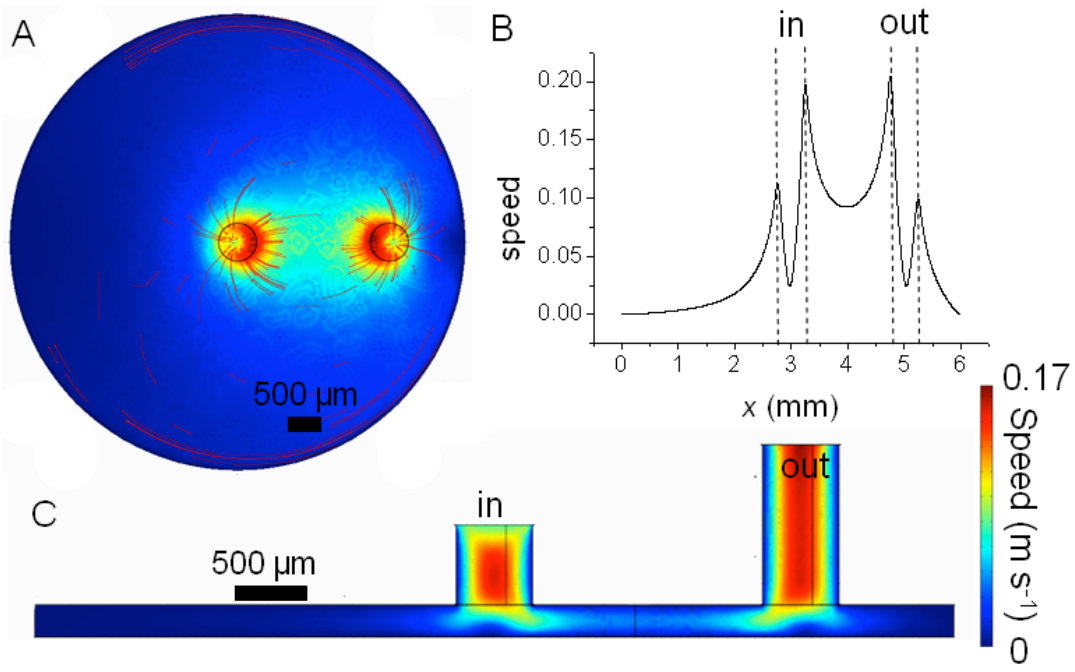

Figure 6.18 FEM of the Navier-Stokes convection within the one outlet configuration for r_n = 250 µm, $2h$ = 200 µm at 10 mL min^{-1} (a) top down view, (b) fluid velocity profile plot taken through the centre of the inlet and outlet at a height of 50 µm, and (c) graphical cross section of (b).

The hydrodynamics provided by this design are inadequate for true radial flow systems, however this kind of device could be easily produced using conventional manufacturing techniques, *e.g.* drilling.

6.3.6. Hydrodynamics of a 4 Outlet Design

Clearly, from the one-outlet design simulations, multiple exit points positioned around the peripheral of the cell would be required to produce a truer, more symmetric radial flow. The 4-outlet design shown in figure 6.19 (a) has a 4 fold rotational symmetry around the inlet nozzle. The solution speed profiles generated for this design are very close to those for the idealised geometry discussed in sections

6.3.2 and 6.3.4. The break down of symmetric radial flow occurs near the outlet sections. Importantly, the distortion of the radial flow does not extend to the substrate surface. As can be seen from the velocity plot close to the electrode surface (at h = 50 µm in a channel of $2h$ = 200 µm), this does not impact upon the convection to the substrate as shown in figure 6.19 (b-d). Figure 6.19 (d) shows that the outlet sections have minimal impact on the radial decay of the fluid velocity 50 µm above the substrate surface, as the fluid velocities reported for a cross section through the centre of an outlet and wall sections are similar. The uniform radial flow provided by this design makes it amenable to be developed into a finished RFC.

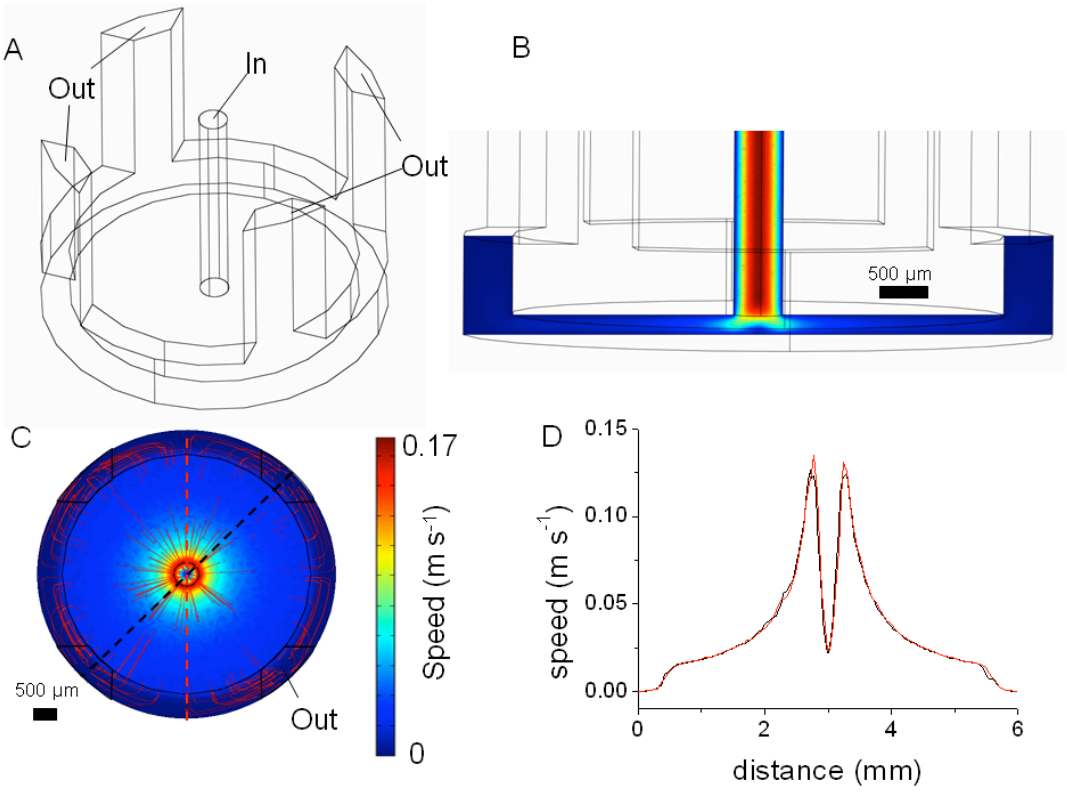

Figure 6.19 (a) Wire frame schematic for the 4 outlet design. FEM of the Navier-Stokes convection within the four outlet configuration for r_n = 250 µm, $2h$ = 200 µm at a V_f of 10 mL min^{-1} (b) cross section view, (c) top down view, (d) fluid velocity profile plot taken through the centre of an inlet (-) and an outlet compared to the cross section taken through the centre of a blocked section (-) at a height of 50 µm.

Figure 6.20 (a) and (b) show the hydrodynamics for the 2D simulation is similar to that for a cross section through the 3D simulation of the 4 outlet design. Additionally, the plot of fluid speed with radial distance for the 4 outlet model is in excellent agreement with the 2D simulation (figure 6.20 (c)). This information validates the design principle, and suggests that the 4 outlet design should provide well-defined mass transport to the electrode surface. Importantly, the mass transport can be predicted by approximating the RFC to the 2D domain presented in section 6.3.2.

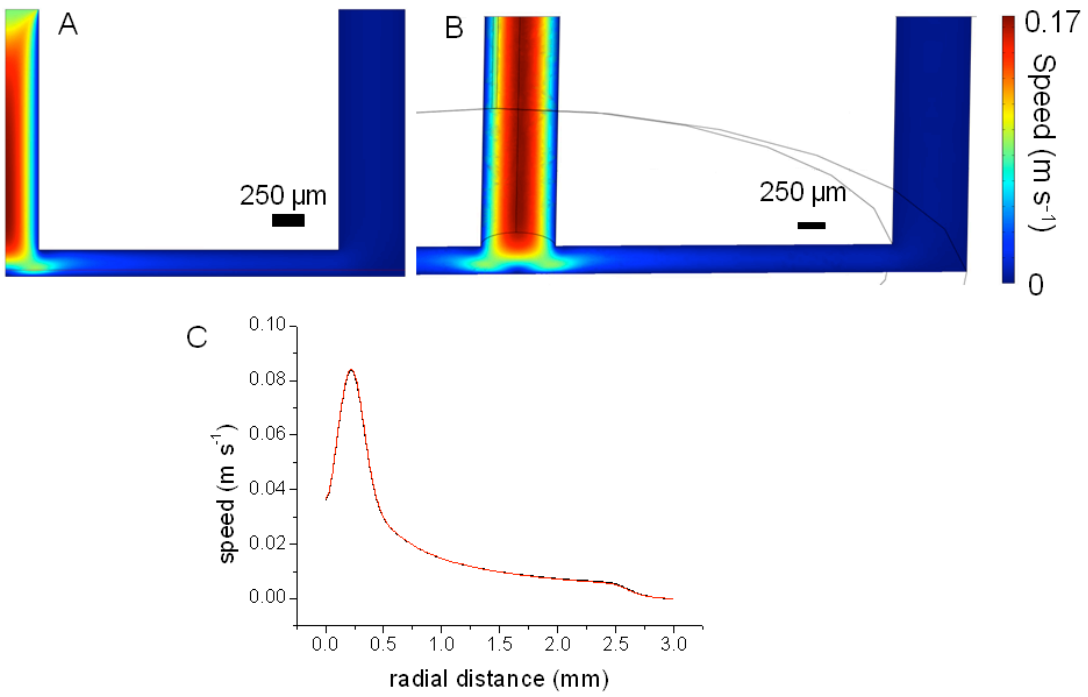

Figure 6.20 Comparison of the hydrodynamics for (a) the 2D simulation and (b) the 3D simulation of the 4 outlet system, where r_n = 250 µm, $2h$ = 200 µm at a V_f of 1 mL min^{-1}. (c) Comparison of the fluid speed with respect to the radial position for the 2D simulation (black line) to the 3D simulation of the 4 outlet design (red line).

6.3.7. Final Design

The FEM simulation of the four outlet design (section 6.3.6) demonstrated that the hydrodynamics near the substrate surface, and hence the electrode, are radial. The simulated domain was used as the basis for the RFC design. As the simulation assumes that the pressure on the four outlets is identical it was deemed necessary to join the 4 outlets within the RFC. This approach reduces the amount of user connections to the RFC, making setup easier for the end user, and provides equal back pressure to the 4 outlets. This was achieved by having the outlets converge directly over the centre of the channel (figure 6.21), hence maintaining the 4 fold axial symmetry of the outlets. Due to the outlet system the impinging jet was required to curve from an initial off centre delivery connection (figure 6.21 (b)), towards the centre of the cell. Note the final section of the nozzle has sufficient straight length to achieve fully developed Poiseuille flow before impinging upon the surface (as for the simulations).

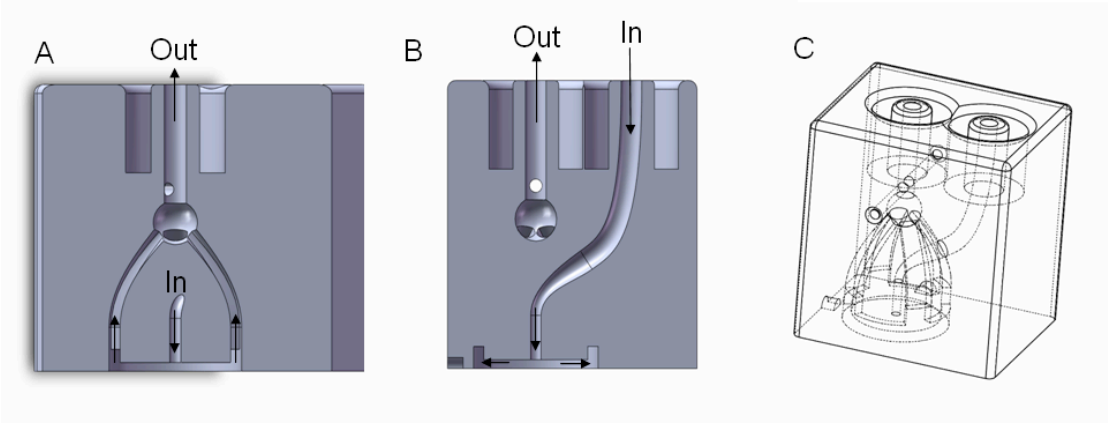

Figure 6.21 Cross section of the MSL RFC design through (a) the centre of 2 outlets and (b) the inlet. (c) Wire frame view of the MSL RFC design.

6.3.8. FEM Simulation of Convection-Diffusion Mass Transport within the RFC

The 3D FEM model presented in sections 6.3.4 and 6.3.6 demonstrated that the RFC design provides well-defined hydrodynamics similar to the idealised system with 360° rotational symmetry. With this evidence, the RFC can be approximated to a 2D model with axial symmetry around the centre of the inlet nozzle. This section describes the FEM performed to predict the limiting current response for an electrode aligned centrally beneath the nozzle within the RFC.

The local values of u_r and w were determined for a particular value of V_f within the RFC, as for section 6.3.2. The values of u_r and w were used to solve the convection-diffusion equation to determine the transport-controlled steady-state current response for the complete oxidation of a solution analyte at the electrode surface (equation 6.14). The FEM simulation was only performed within a domain close to the electrode surface to improve the speed and accuracy of the calculations. The domain, enclosed by boundaries 1-3, and 6-8, was sufficiently large to prevent distortion due to boundary edge effects on the results. The domain was treated by solving the following equation:

$$\nabla(-D\nabla c) = -\mathbf{V}\nabla c \qquad \textbf{(6.14)}$$

where D is the diffusion coefficient (assumed to be 6 x 10^{-6} cm^2 s^{-1}, as for $FcTMA^+$)[29] and c the concentration of $FcTMA^+$.

The following boundary conditions were applied for the convection and diffusion calculations:

Boundaries 1, 6 and 7: $\mathbf{n} \cdot \mathbf{N} = 0$ **(6.15)**

Boundary 2: $c = 0$ **(6.16)**

Boundary 3: $c = c_b$ **(6.17)**

Boundary 8: $\mathbf{n}(-D\nabla c) = 0$ **(6.18)**

where **N** is the inward flux, and c_b is the bulk concentration of $FcTMA^+$.

Boundaries 1, 6 and 7 have no net flux normal to the boundary due to boundary 1 being the axis of symmetry, and boundaries 6 and 7 being inert walls of the wall jet set-up. Boundary 2 represents the electrode, a disc of radius r_e, where the complete and instantaneous oxidation of $FcTMA^+$ occurs. Boundary 3 is positioned sufficiently far from the electrode so that the assumption of bulk concentration at the boundary is reasonable, and boundary 8, the end of the convection-diffusion domain, is placed sufficiently far from the downstream electrode edge so that the boundary condition of only convective flux does not affect mass transport at the electrode surface.

The transport limited current (i_{lim} (A)) response was calculated from the total flux at boundary 2, multiplying by $nF\pi r_e$, where n is the number of electrons transferred per redox event, and F is the Faraday constant (96485 C mol^{-1}).

The approximations of the convection-diffusion only domain are validated in figure 6.22 where the concentration profile within the entire RFC has a difference of less than 0.1% to the response within the convection-diffusion only domain for a RFC of dimensions, r_n = 150 μm $2h$ = 100 μm r_e = 1 mm V_f = 0.1 mL min^{-1} c_b = 10 μmol dm^{-3} and D = 6 x 10^{-6} cm^2 s^{-1}, both approaches predict a limiting current response of 313 nA.

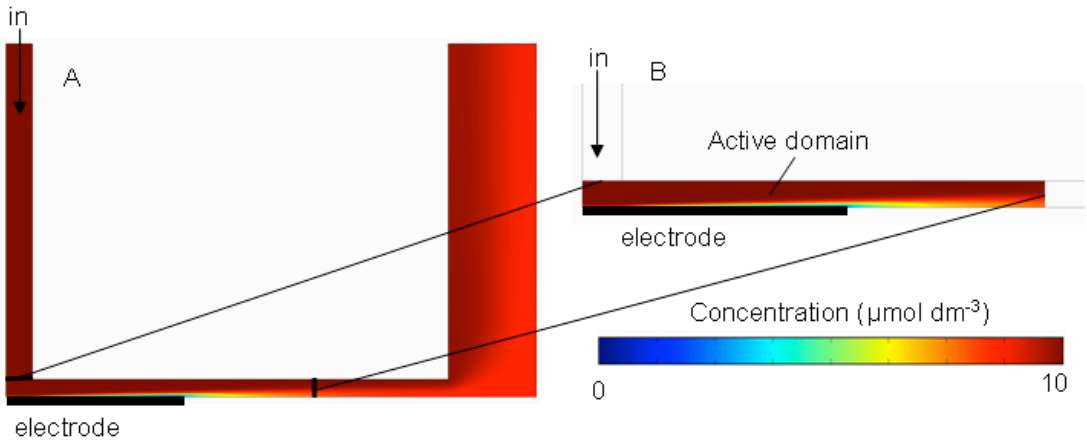

Figure 6.22 Validation of the convection-diffusion only domain for the RFC theoretical calculations. (a) The concentration profile predicted by simulation for convection and diffusion within the entire geometry and (b) the concentration profile calculated only within the domain close to the electrode

6.3.9. Simulated Current Response

As discussed in section 1.4.4, the geometry of the impinging jet and substrate affect the mass transport to the electrode. Equations 1.28 and 1.29 show that the relationship of the limiting current response to V_f, r_n, $2h$ and r_e depend on whether the impinging jet electrode is in the WJE or WTE configuration.[1, 5, 16, 27] Additionally, the position of the nozzle, and the nozzle wall, affect the mass transport to the electrode surface. A series of simulations were performed to determine the dependence of the i_{lim} response upon V_f, r_n, $2h$ and r_e. It should be noted that for all geometries the reported c_b and D dependencies are the same, with a linear dependence to c_b and a $D^{2/3}$ dependence.[1, 5, 16, 27] For all simulations reported in this section c_b = 20 µmol dm^{-3} and D = 6 x 10^{-6} cm^2 s^{-1}.

Figure 6.23 shows the dependence of i_{lim} on V_f for a RFC of r_n = 375 µm, $2h$ = 100 µm and r_e = 500 µm. The gradient of the log i_{lim} – log V_f plot, figure 6.23 (b), is 0.33 suggesting that i_{lim} increases proportionally to $V_f^{1/3}$, which is similar to the flow rate

dependence experienced at a channel flow electrode.[30, 31] It is important to note that at sufficiently low flow rates (~0.05 mL min^{-1} for this system) diffusion dominates mass transport to the electrode and the $V_f^{1/3}$ dependence is no longer valid.

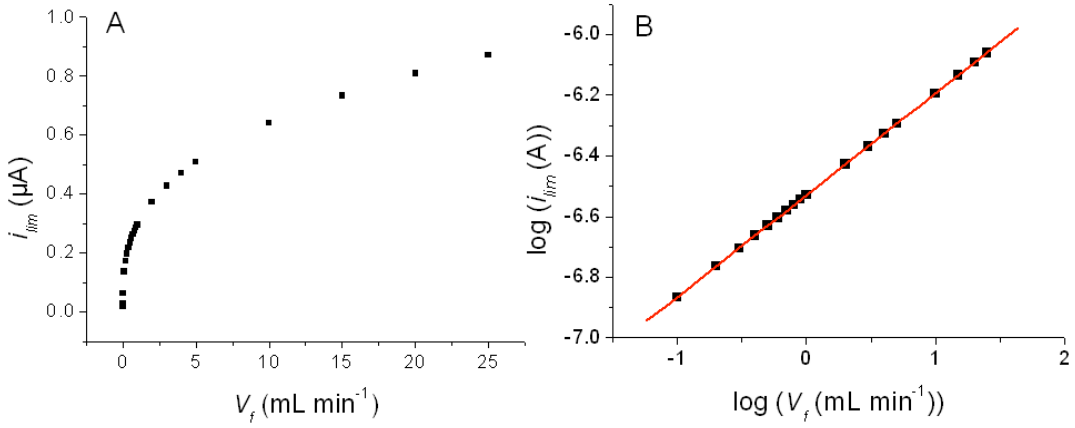

Figure 6.23 (a) Effect of varying the V_f on the i_{lim} response, (b) log V_f - log i_{lim} plot where the gradient is 0.33.

The effect of varying r_n can be seen in figure 6.24, where r_n is varied from 100 μm to 375 μm in a cell of $2h$ = 100 μm and r_e = 500 μm. As r_n decreases the mean fluid velocity from the impinging jet increases, resulting in a higher rate of mass transport to the electrode surface. Within the RFC, the roof of the channel influences the hydrodynamic profile. Thus, varying the radius of the nozzle affects the hydrodynamics within the stagnation zone and the area of developing radial flow. As the log i_{lim} – log r_n plot (figure 6.24 (b)) is not linear, the effect of varying nozzle dimensions on the i_{lim} response requires analysis by FEM.

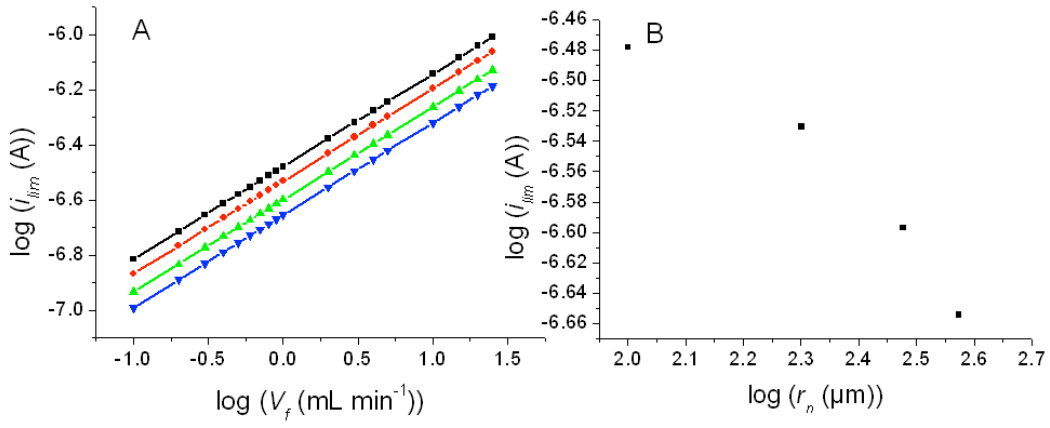

Figure 6.24 (a) Effect of varying the r_n on the i_{lim} response for r_n = 100 µm (black line), 200 µm (red line), 300 µm (green line), and 375 µm (blue line), (b) log r_n - log i_{lim} plot at V_f = 1 mL min^{-1}, for a RFC of dimensions $2h$ = 200 µm, r_e = 0.5 mm.

The i_{lim} dependence on the cell height is shown in figure 6.25, where $2h$ is varied from 50 µm to 200 µm in a cell of r_n = 375 µm and r_e = 500 µm at a V_f of 1 mL min^{-1}. Figure 6.25 (a) shows that as the height decreases the i_{lim} response increases, and that the V_f value where diffusion dominates the mass transport increases. This effect is due to depletion of the analyte within the channel occurring faster, hence at higher V_f values, when $2h$ is decreased. Figure 6.25 (b) has a gradient of -0.4, suggesting i_{lim} is proportional to $2h^{-2/5}$, here the RFC deviates from the channel electrode behaviour which has a $h^{-2/3}$ dependence.[30, 31]

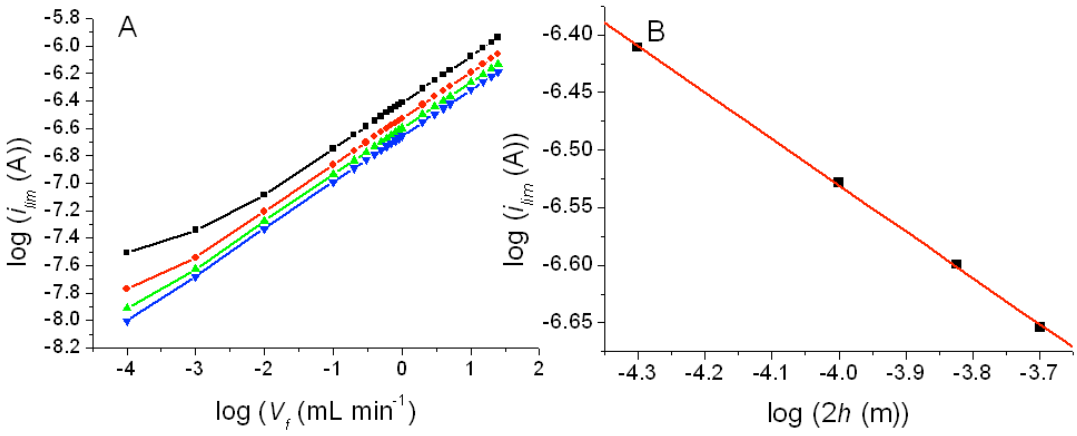

Figure 6.25 (a) Effect of varying h on the i_{lim} response, where $2h$ = 50 µm (black line), 100 µm (red line), 150 µm (green line), and 200 µm (blue line), (b) log $2h$ - log i_{lim} plot where the gradient is -0.4.

As the electrode radius increases the i_{lim} response increases, as shown in figure 6.26. The log i_{lim} – log r_e plot is approximately linear over the r_e range of 0.38 mm – 2 mm, with a gradient of 1.7 for a RFC with dimensions r_n = 375 µm and $2h$ = 100 µm at a V_f of 1 mL min^{-1}. The deviation from linear dependence of the limiting current to the electrode to $r_e^{1.7}$ is negligible over the simulated range. It should be noted that the range of electrode sizes ensures that the bulk of the electrode is within the area of developed radial flow. Electrodes entirely within the stagnation zone or with a circumference near the outlet sections will deviate from the approximate limiting current – electrode radius dependence.

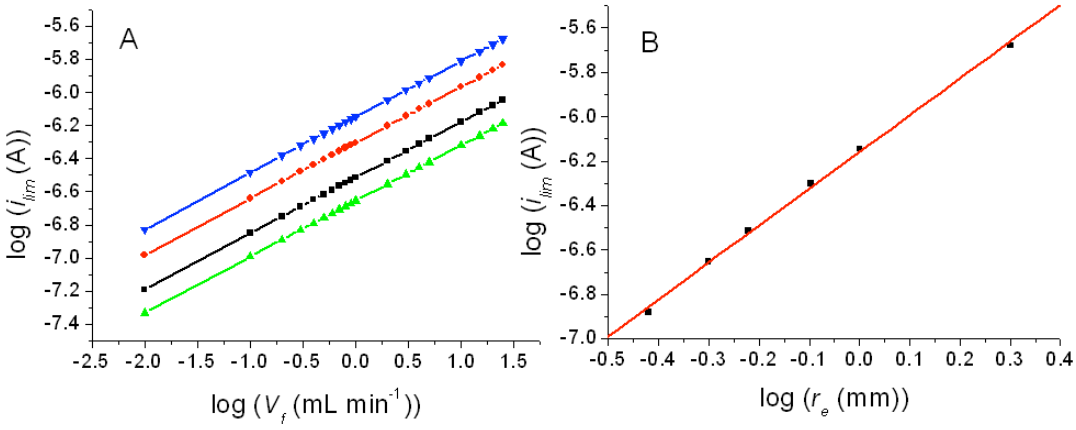

Figure 6.26 (a) Effect of varying the r_e on the i_{lim} response, (b) log r_e - log i_{lim} plot where the gradient is 1.7.

The reported simulations demonstrate that it is essential to know the RFC dimensions in order to accurately predict the limiting current response. The influence of the nozzle radius on the internal hydrodynamics requires each device to be simulated explicitly. By only simulating the convection and diffusion close to the electrode (section 6.3.8) it is possible to analyse the limiting current response for over 20 flow rates in a few hours. As such, the hydrodynamic profile, and electrochemical response within individual RFCs can be readily predicted.

6.4. Experimental

6.4.1. Electrode Fabrication

Gold and VHD SWNT network electrodes were prepared as described in chapter 2. The electrode area was defined using a custom made macro disc mask with alignment marks to aid the assembly of the RFC. Electrode dimensions were

measured using an optical microscope (Olympus BH2). The SCE reference electrode was used with the modified pipette tip described in section 5.3.3, and a Pt wire was utilised as the counter electrode.

6.4.2. RFC assembly

The RFC was produced using the same method described for MSL production, section 2.4, using the unit cell in figure 6.21. As for the channel flow cell four units could be produced in one run (chapter 4). The design could be easily modified to provide a range of nozzle diameters and channel heights. As for the channel flow cell the channel height was determined by white light interferometry (WYKO NT-2000 Surface Profiler, WYKO Systems).

Two methods were used to align the electrode directly underneath the inlet of the wall jet cell. (i) The first method, illustrated in figure 6.27, used on the gold electrode, was performed using a manually controlled vertical stage. Initially, the disc electrode was positioned centrally underneath a custom made alignment tip, attached to the vertical stage (figure 6.27 (b)). The outlet of the RFC was attached by push fitting to the alignment tip and lowered onto the electrode surface (figure 6.27 (c) and (d)). The RFC was temporarily secured to the electrode surface by modelling putty, which allowed the removal of the tip from the RFC. Finally, the RFC was bound to the electrode using thread (figure 6.27 (e)). This method allowed an accuracy of ~100 μm (radial offset) to be achieved reliably.

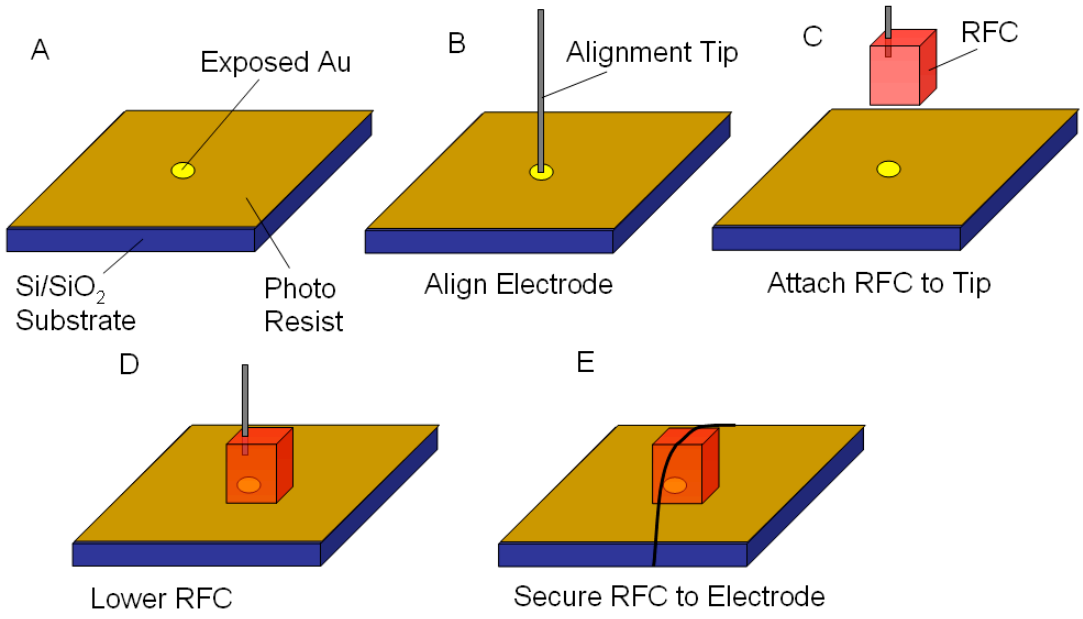

Figure 6.27 Illustration of the RFC and electrode alignment method used for assembling the RFC and Au electrodes. (a) Schematic of the developed Au electrode, (b) alignment of the electrode, (c) mounting the RFC onto the alignment tip over the electrode, (d) the RFC is lowered onto the electrode surface, (e) the RFC is secured to the electrode and the alignment tip is removed. Not to scale.

The second method (used for the SWNT samples) involved alignment of the wall jet cell to alignment features on a photo resist mask (figure 6.28) before being bound to the electrode with thread. To further improve accuracy the overall pattern has identical dimensions to the base of the RFC. The alignment accuracy was comparable to the first method (~100 µm radial offset), but can be achieved in less than half the time. Solution was delivered to the system through piping, (PVC, Vincon Tubing) using a single piston liquid chromatography pump (Gilson 305) fed through a manometric module (Gilson 806) to maintain a constant volume flow rate, minimum $V_f = 0.0025$ mL min^{-1}, maximum $V_f = 25$ ml min^{-1}.

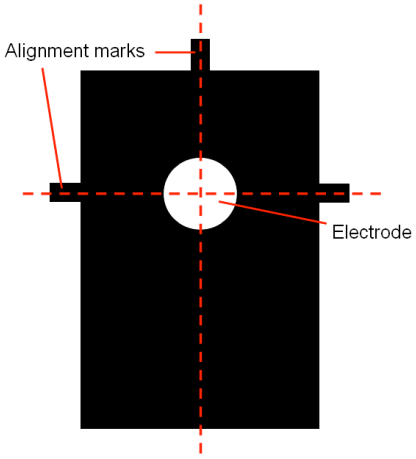

Figure 6.28 Design of the photo resist mask where the actual area was the same as the base of the RFC and the alignment marks fitted features on the RFC. Several masks were made with different electrode radii.

6.5. Results and Discussion

The transport limited current was initially measured using the gold electrode. For these measurements a RFC with r_n = 375 µm and $2h$ = 100 µm (figure 6.10) was used with the gold electrode (r_e = 540 µm). Figure 6.29 (a) shows typical LSVs for the oxidation of 10 µmol dm^{-3} $FcTMA^+$ in 1 mol dm^{-3} KNO_3 at 100 mV s^{-1} at various flow rates. Figure 6.29 (b) shows the comparison of the experimental limiting current response is in reasonable agreement with that predicted by the finite element model. This demonstrates that the device provides well-defined mass transport, as predicted by the finite element model. As reported in chapter 4 the RFC dimensions are not distorted by assembly, this useful feature of MSL removes the need for calibration measurements for each assembly of the RFC. The small variation from the predicted response is attributed to the RFC not being exactly over the centre of the electrode, as the alignment method employed had a maximum error of ~100 µm radial offset.

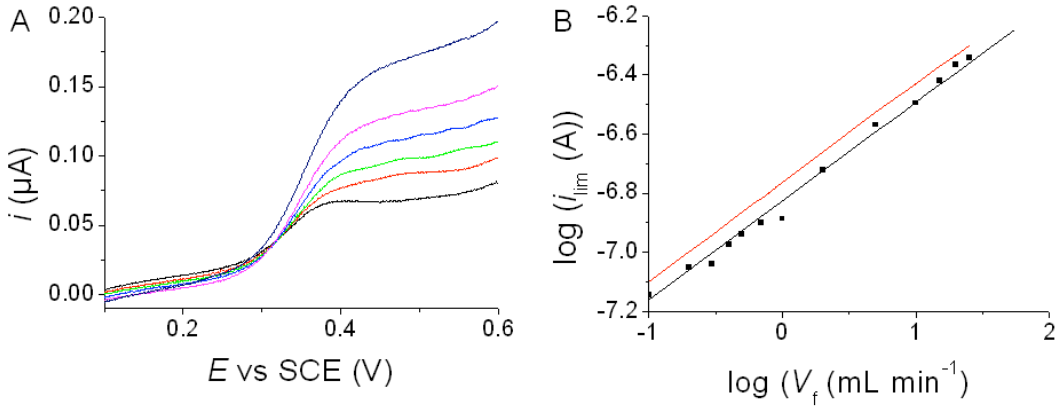

Figure 6.29 (a) Typical LSVs for the oxidation of 10 μM $FcTMA^+$ in 1.0 M KNO_3 at a Au disc electrode (r_e = 0.54 mm r_n = 375 μm and $2h$ = 100 μm) at 100 mV s^{-1} at V_f values of 0.01 (lowest current), 0.05, 0.05, 0.2, 0.4, 1.0 (highest current) ml min^{-1}. (b) Comparison of the experimentally obtained i_{lim} (black data) to the finite element predicted response (solid red line).

To ensure that the wall jet cell could be used in conjunction with SWNT networks it was essential to verify that the SWNT networks were not damaged during the assembly of the RFC or by the impinging flow. An electrode of radius 500 μm was used in conjunction with a wall jet cell with r_n = 375 μm and $2h$ = 100 μm to experimentally verify this.

Figure 6.30 (a) shows typical LSVs for the oxidation of 20 μmol dm^{-3} $FcTMA^+$ in 1 M KNO_3. Particular attention should be drawn to the reduced non-Faradic signal, as observed previously by Bertoncello *et al.*[32] Figure 6.30 (b) shows the comparison of the experimentally observed limiting current to that predicted by the 2D finite element model. The experimental response is slightly lower than predicted; this can be attributed to the nozzle not being directly over the centre of the disc. This is due to the alignment procedure providing an error of up to 100 μm. Figure 6.19 (d) shows that the outer edge of the electrode (radius 500 μm) is located near the two maxima of the fluid velocity. The effect of this error in alignment can be

minimised by using a larger radius electrode so that the electrode circumference lies in an area where the change in fluid speed is small (*e.g.* r_e = 1 mm). It is important to note that the error is small (less than 5%), and is consistent across the entire V_f range.

These data fully support the theoretical model for both the gold and SWNT network disc electrodes, demonstrating that the MSL RFC provides well-defined mass transport to the electrode surface.

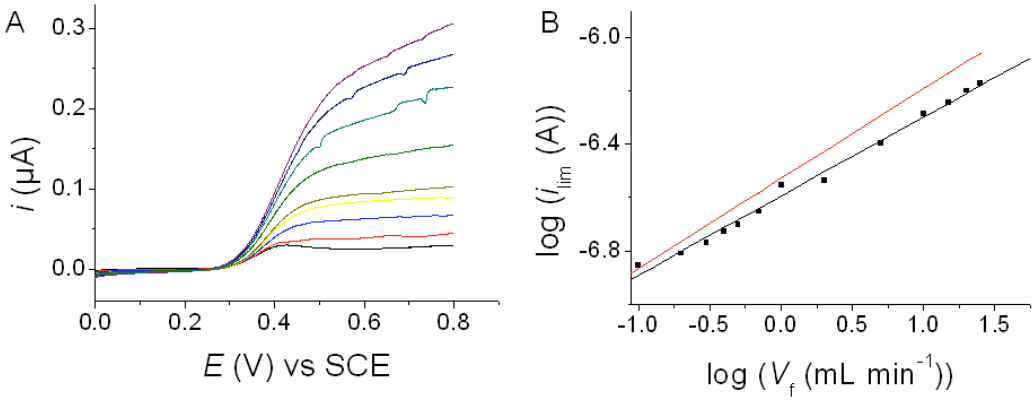

Figure 6.30 (a) Typical LSVs for the oxidation of 20 μM $FcTMA^+$ in 1.0 M KNO_3 at a SWNT disc electrode (r_e = 0.5 mm r_n = 375 μm and $2h$ = 100 μm) at 100 mV s^{-1} at V_f values of 0.01 (lowest current), 0.05 0.1 0.2 0.3 0.4 0.5 0.7 1.0 2.0 5.0 10.0 15.0 (highest current) ml min^{-1}. (b) Comparison of the experimentally obtained i_{lim} (black data) to the finite element predicted response (solid red line).

To demonstrate the use of the RFC and SWNT electrode a concentration gradient for $FcTMA^+$ was performed. The detection of 100 nmol dm^{-3} of $FcTMA^+$ on a disc of radius 1 mm, is shown in figure 6.31 where a RFC of dimensions r_n = 375 μm and $2h$ = 202 μm at a V_f of 15 mL min^{-1} was employed.

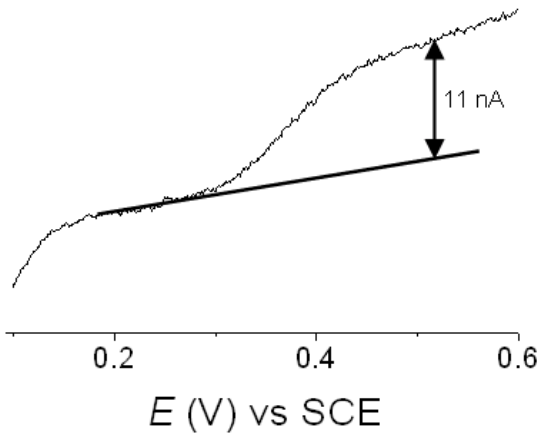

Figure 6.31 (a) LSV of 100 nM $FcTMA^+$ 1 M KNO_3 on a SWNT disc electrode (r_e = 0.99 mm, r_n = 375 μm, h = 202 μm, and V_f = 15 mL min^{-1}

The i_{lim} response follows the same V_f trends as for the previous electrodes (figure 6.32 (a)), and produces a linear i_{lim} - V_f response for the concentration range of 100 nmol dm^{-3} to 1 μmol dm^{-3}. Figure 6.32 (b) shows the. The gradient of the log c_b vs log i_{lim} plot is approximately 1, suggesting that the limiting current response is directly proportional to the concentration, providing confirmation of this new type of flow cell as an analytical device. The linear concentration dependence holds for all tested flow rates (1 mL min^{-1} – 25 mL min^{-1}). The detection limit is estimated to be 10 nmol dm^{-3} for the RFC and SWNT disc electrode dimensions tested.

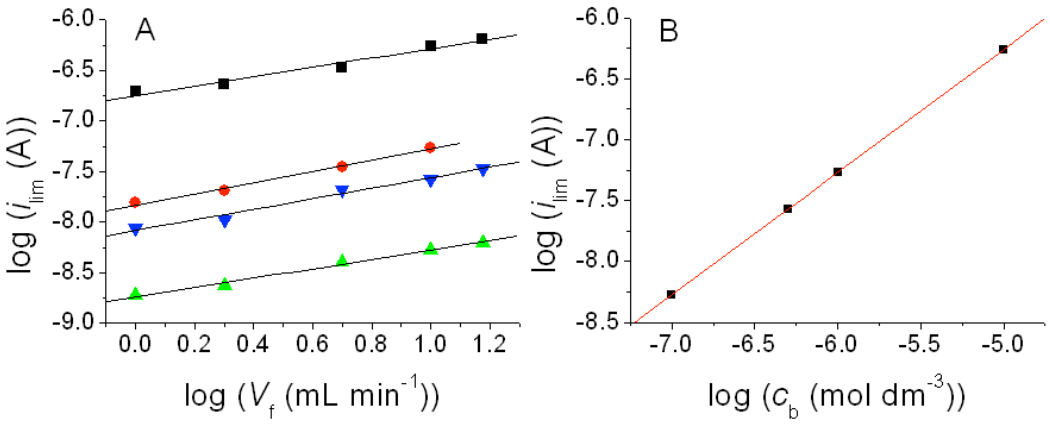

Figure 6.32 (a) i_{lim} response at different concentrations, 10 nmol dm^{-3} (■), 1 µmol dm^{-3} (●), 0.5 µmol dm^{-3} (▼) and 0.1 µmol dm^{-3} (▲). (b) Concentration gradient at V_f = 10 mL min^{-1} using a SWNT disc electrode (r_e = 0.99 mm, r_n = 375 µm, h = 202 µm

6.6. Conclusions

This chapter has reported the successful design and development of a RFC that can be rapidly assembled and provides well-defined mass transport to electrode surfaces. The use of MSL to create the RFCs allows the ready realisation of modifications to the nozzle dimensions and channel height, and facilitates the customisation of the wall jet cell to specific applications. This could include the use of optically transparent materials for the RFC, or electrode, to facilitate the combination of electrochemical and spectroscopic techniques; *e.g.* confocal microscopy and UV- visible spectroscopy.

It has been shown that the limiting current response of the two piece RFC design can be predicted by FEM. The RFC can be assembled onto the electrode quickly, and without the distortion of the channel dimensions, making the device applicable to a wide range of planar electrode materials. This has been demonstrated by the use of gold and SWNT disc electrodes. The SWNT electrode facilitates the low

concentration (100 nmol dm^{-3}) detection of $FcTMA^+$ with a detection limit of 10 nmol dm^{-3}.

6.7. References

(1) Macpherson, J. V.; Marcar, S.; Unwin, P. R. *Anal. Chem.* **1994**, *66*, 2175.
(2) Macpherson, J. V.; Beeston, M. A.; Unwin, P. R. *Journal of the Chemical Society-Faraday Transactions* **1995**, *91*, 899.
(3) Martin, R. D.; Unwin, P. R. *Journal of Electroanalytical Chemistry* **1995**, *397*, 325.
(4) Compton, R. G.; Fisher, A. C.; Tyley, G. P. *Journal of Applied Electrochemistry* **1990**, *20*, 912.
(5) Chin, D. T.; Tsang, C. H. *Journal of the Electrochemical Society* **1978**, *125*, 1461.
(6) Powell, F. E.; Fogg, A. G. *Analyst* **1988**, *113*, 483.
(7) Bitziou, E.; Rudd, N. C.; Edwards, M. A.; Unwin, P. R. *Analytical Chemistry* **2006**, *78*, 1435.
(8) Chin, D. T.; Chandran, R. R. *Journal of the Electrochemical Society* **1981**, *128*, 1904.
(9) Powell, F. E.; Fogg, A. G. *Electroanalysis* **1990**, *2*, 463.
(10) Macpherson, J. V.; Unwin, P. R. *Analytical Chemistry* **1998**, *70*, 2914.
(11) Macpherson, J. V.; Jones, C. E.; Unwin, P. R. *Journal of Physical Chemistry B* **1998**, *102*, 9891.
(12) Albery, W. J.; Brett, C. M. A. *Journal of Electroanalytical Chemistry* **1983**, *148*, 211.
(13) Thiemig, D.; Bund, A.; Talbot, J. B. *Journal of the Electrochemical Society* **2007**, *154*, D510.
(14) Macpherson, J. V.; Unwin, P. R. *Analytical Chemistry* **1997**, *69*, 5045.
(15) Bitziou, E.; Rudd, N. C.; Unwin, P. R. *Journal of Electroanalytical Chemistry* **2007**, *602*, 263.
(16) Macpherson, J. V.; Simjee, N.; Unwin, P. R. *Electrochimica Acta* **2001**, *47*, 29.
(17) Macpherson, J. V.; Unwin, P. R. *Analytical Chemistry* **1999**, *71*, 4642.
(18) Rees, N. V.; Klymenko, O. V.; Coles, B. A.; Compton, R. G. *Journal of Electroanalytical Chemistry* **2003**, *557*, 99.
(19) Aoki, K.; Tokuda, K.; Matsuda, H. *Journal of Electroanalytical Chemistry* **1986**, *206*, 37.
(20) Albery, W. J.; Brett, C. M. A. *Journal of Electroanalytical Chemistry* **1983**, *148*, 201.
(21) Yamada, J.; Matsuda, H. *Journal of Electroanalytical Chemistry* **1973**, *44*, 189.
(22) Compton, R. G.; Fisher, A. C.; Latham, M. H.; Brett, C. M. A.; Brett, A. *Journal of Physical Chemistry* **1992**, *96*, 8363.
(23) Melville, J. L.; Coles, B. A.; Compton, R. G.; Simjee, N.; Macpherson, J. V.; Unwin, P. R. *Journal of Physical Chemistry B* **2003**, *107*, 379.

(24) Melville, J.; Simjee, N.; Unwin, P. R.; Coles, B. A.; Compton, R. G. *Journal of Physical Chemistry B* **2002**, *106*, 2690.
(25) Compton, R. G.; Greaves, C. R.; Waller, A. M. *Journal of Applied Electrochemistry* **1990**, *20*, 575.
(26) Brett, C. M. A.; Brett, A.; Fisher, A. C.; Compton, R. G. *Journal of Electroanalytical Chemistry* **1992**, *334*, 57.
(27) Albery, W. J. *Journal of Electroanalytical Chemistry* **1985**, *191*, 1.
(28) Lide, D. R. *CRC Handbook of Chemistry and Physics*; CRC Press: USA, 2001.
(29) Bertoncello, P.; Ciani, I.; Li, F.; Unwin, P. R. *Langmuir* **2006**, *22*, 10380.
(30) Compton, R. G.; Unwin, P. R. *Journal of Electroanalytical Chemistry* **1986**, *206*, 57.
(31) Compton, R. G.; Unwin, P. R. *Journal of Electroanalytical Chemistry* **1986**, *205*, 1.
(32) Bertoncello, P.; Edgeworth, J. P.; Macpherson, J. V.; Unwin, P. R. *Journal of the American Chemical Society* **2007**, *129*, 10982.

7. Conclusion

The work within this thesis has covered two key topics; the properties and use of SWNT networks as an electrode material and the design and development of hydrodynamic cells fabricated by microstereo lithography.

The investigation into the sites of ET at a SWNT network is of fundamental importance to the use of SWNTs as an electrode material. To make efficient use of electrode treatment steps and to optimise the material it is important to know what gives rise to the electrochemical response. The two proposed theories for ET, sidewall activity and discrete site activity, were investigated by the combination of theoretical and experimental studies. Diffusion to the active sites was successfully decoupled on a typical voltammetric timescale by reducing the rate of diffusion using a drop-cast Nafion^{TM} film. This prevented diffusion layer overlap and allowed the critical comparison of the theoretical and experimental data. Even when using a generous quantity of active sites the discrete active site model significantly underestimated the current response, indicating that the sidewall of the SWNT must contribute to the electrochemical activity of the SWNT network. However, the predicted current response for the SWNT side wall being entirely active overestimated the observed current response, indicating that the SWNTs were not homogenously active.

The design of hydrodynamic devices for application to a variety of planar substrates, whilst removing the need for electrochemical calibration experiments and sealant material is advantageous to numerous electrochemical experiments. The channels were fabricated using MSL, a computer aided layer-by-layer photo-polymerisation. MSL allowed devices with complex internal structures to be constructed with a high level of accuracy. Importantly, the cured polymer used to

construct the channel is not distorted by the operating conditions employed. The work within chapter 4 outlined the design concepts and demonstrated that the electrochemical response within the channel was predictable for band electrodes and for the entire channel floor being active. The device was successfully applied to a range of electrode materials, including metallic electrodes, pBDD and SWNTs (in chapter 5). The channel was ready to use, without the need for calibration after assembly of the cell, allowing application to any planar electrode material. The use of MSL allows the basic channel design to be easily modified to incorporate additional electrodes, *e.g.* ion selective electrodes, and mixing channels for dissolution studies.

The success of the channel flow cell presented in chapter 4 was applied to the impinging jet geometry in chapter 6. The complexities and common variants of the impinging jet set-up were theoretically investigated to determine the final design for the radial flow cell. The layer-by-layer construction method of MSL was utilised to create a true radial flow geometry which would be difficult to produce by conventional manufacturing techniques. The device features a four-fold symmetric outlet system which prevented distortion of the characteristic radial flow of an impinging jet. Importantly the use of MSL allowed a variety of internal dimensions to be varied providing a device that could be customised for the desired solution speed and flow rates. As for the channel flow cell, the RFC could be constructed rapidly and with the use of custom built photo-resist alignment masks the nozzle could be positioned accurately over the centre of the electrode.

This thesis has provided evidence for the sidewall activity of SWNTs, and demonstrated the benefits of the low non-Faradaic noise associated with a two dimensional SWNT network. The networks were readily synthesised using the cCVD techniques outlined within the thesis and were amenable to hydrodynamic

applications. The application of MSL to the production of hydrodynamic devices provides the fundamental framework for future studies using both channel and radial flow. The flow devices can be assembled onto any planar substrate, allowing for dissolution studies and for generation/collection studies. Further developments of MSL could provide access to smaller dimensions, and potentially assembly from polymers with optical windows. This could replace complex channel designs featuring quartz windows for combined spectroscopic studies and will maintain the design freedom provided by the MSL design methodology. The design flexibility inherent in the channel and radial flow cell designs allows for many exciting possibilities which were previous hindered by cell dimensions, or difficult assembly procedures.